NEUTRON SPECTROSCOPY OF ^{7}Li(p,n) WITH A ^{3}He ION CHAMBER

NEUTRON SPECTROSCOPY OF AN ACCELERATOR BASED ^{7}Li(p,n) NEUTRON SOURCE WITH A ^{3}He IONIZATION CHAMBER

By

WITOLD MATYSIAK

A Thesis
Submitted to the School of Graduate Studies
in Partial Fulfillment of the Requirements
for the Degree
Doctor of Philosophy

McMaster University

DOCTOR OF PHILOSOPHY (2010)
(Medical Physics and Applied Radiation Sciences)

McMaster University
Hamilton, ON, Canada

TITLE: Neutron spectroscopy of an accelerator based ^{7}Li(p,n) neutron source with a ^{3}He ionization chamber

AUTHOR: Witold Matysiak, MSc. Eng. (Politechnika Warszawska, Warsaw, Poland)

SUPERVISOR: Dr. Soo-Hyun Byun

NUMBER OF PAGES: xvi, 125

ABSTRACT

Significant discrepancies had been identified by many research groups worldwide between calculated and measured neutron doses from the ^{7}Li(p,n) accelerator based neutron source, and therefore precise characterization of the source was needed. In this work neutron spectra from the ^{7}Li(p,n) source were measured with a ^{3}He ion chamber in the incident proton energy range from 1.95 to 2.3 MeV. The ^{3}He detector is hypersensitive to slow neutrons, so a time-of-flight based slow neutron rejection acquisition system was built and tested. The system is based on an electrostatic proton chopper and an acquisition system working in coincidence mode. The response function of the ^{3}He was extended down to 30 keV neutron energy and the collected neutron spectra were unfolded using two methods: van Cittert iterative algorithm with Jansson constraint, and a regularized constrained inversion. Theoretical neutron spectra emitted by the ^{7}Li(p,n) source were calculated and compared with experimental unfolded spectra, as well as with results of the Monte Carlo simulations of the lithium target assembly and the walls of the experimental area. Using fluence to kerma conversion coefficients, the neutron dose was calculated and compared with results obtained from an independent experiment using the microdosimetric technique with a tissue equivalent proportional counter. Total neutron yield of the ^{7}Li(p,n) reaction was measured using induced activity of ^{7}Be. Results showed a negative energy offset of the incident proton beam between 50 and 58 keV with respect to the generating voltmeter indication of the accelerator terminal. Shapes of the measured neutron spectra showed significant moderation originating from neutron scattering on the lithium target assembly and walls of the experimental area. When accounting for this offset, neutron yields showed an agreement with calculated values within 22 % for 1.95 MeV and within approximately 7 % for higher proton energies.

ACKNOWLEDGEMENTS

I would like to express my gratitude to my supervisor Dr. Soo-Hyun Byun. His wide knowledge of nuclear spectroscopy and enthusiasm in investigating new challenges was instrumental in creation of this thesis.

I am also grateful to my mentor Dr. William V. Prestwich for inspiring discussions at tea time.

This work could not be possible without the selfless guidance of Dr. David R. Chettle, who presented me with a possibility of graduate work at McMaster.

I also received professional help and used the experience of Alice Pidruczny, Scott McMaster, Jason Falladown, and Kenrick Chin, to whom I am very grateful.

I would also like to thank my friends and colleagues who shared the graduate work experience with me. Among them are Lisa Liu, Mariangela Zamburlini, Ali Fatemi-Arkedani, Andrei Hanu, Jovica Atanackovic, Aravinthan Jegatheesan, and Arjit Baghwala.

Finally, I would like to thank my fiancée Grażyna Drzazga for her continuous support.

TABLE OF CONTENTS

LIST OF FIGURES

LIST OF TABLES

1. INTRODUCTION 1

2. MEASUREMENT OF THE THICK TARGET ^{7}Li(p,n) NEUTRON SOURCE SPECTRUM USING A ^{3}He IONIZATION CHAMBER 13

3. RELATIVE ENHANCEMENT OF A ^{3}He ION CHAMBER RESPONSE TO FAST NEUTRONS BY TOF REJECTION OF SLOW NEUTRONS WITH A PULSED NEUTRON SOURCE 28

4. OPTIMIZATION OF THE PROTON CHOPPER FOR ^{7}Li(p,n) NEUTRON SPECTROMETRY USING A ^{3}He IONIZATION CHAMBER 45

5. MEASUREMENTS OF THE NEUTRON SPECTRUM FROM THE ^{7}Li(p,n) ACCELERATOR BASED NEUTRON SOURCE AT VARIOUS PROTON ENERGIES AS WELL AS ANGLES AND DISTANCES FROM THE LITHIUM TARGET 73

6. PRECISE MEASUREMENTS OF THE THICK TARGET NEUTRON YIELDS OF THE ^{7}Li(p,n) REACTION 94

TABLE OF ABBREVIATIONS

ABNS	Accelerator Based Neutron Source
ADC	Analog to Digital Converter
Be	Beryllium
BF_3	Boron Trifluoride
CMS	Center of Mass System
DPP	Digital Pulse Processing
DSP	Digital Signal Processor
Eu	Europium
FWHM	Full Width at Half Maximum
GVM	Generating Voltmeter
He	Helium
HPGe	Hyperpure Germanium
HV	High Voltage
LET	Linear Energy Transfer
Li	Lithium
LLD	Low Level Discriminator
MC	Monte Carlo
MCA	Multichannel Analyzer
MCNP	Monte Carlo N-Particle
MCS	Multichannel Scaler
NaI(Tl)	Sodium Iodide Thallium Activated
PHA	Pulse Height Analyzer
Sm	Samarium
TEPC	Tissue Equivalent Proportional Counter
TOF	Time-Of-Flight
TSCA	Timing Single Channel Analyzer

Chapter 1

INTRODUCTION[♣]

1.1. ^{7}Li(p,n) accelerator based neutron source

The ^{7}Li(p,n) reaction has been employed in medical and radiobiological applications requiring intense neutron sources with low energy accelerators (Byun et al., 2007; Aslam et al., 2008; Blue & Yanch, 2003; Culbertson et al., 2004). The lithium target produces a high neutron yield for a given incident energy of protons and requires relatively low proton energy compared to the other competing proton-induced reaction, ^{9}Be(p,n). The physical instability of the pure lithium metal due to its low melting temperature (180 °C) makes it challenging to use as a target, particularly for high current operations, but this problem can be addressed by extensive cooling of the target assembly (Petrich et al., 2008; Bayanov et al., 2009). Another practical difficulty stems from the chemical instability of lithium. Due to its strong oxidation potential, lithium metal quickly creates an oxidation layer on the surface when exposed to air. Although target preparation and installation is generally carried out under a noble gas environment, there may always be a risk of temporary air exposure. The oxide layer can lead to a decrease in total neutron yield as compared to the yield from a pure metal target. Finally, carbon deposits can accumulate on the surface of the lithium target, which is unavoidable when oil diffusion vacuum pumps are used in

---

[♣] Text of the introduction chapter is closely based on the introduction sections of the four publications constituting this thesis:

Chapter 2 - W. Matysiak, W.V. Prestwich, S.H. Byun, Measurement of the thick target ^{7}Li(p,n) neutron source spectrum using a ^{3}He ionization chamber, Nucl. Instr. Meth. A, 2008; 592: 316-324.

Chapter 3 - W. Matysiak, K. Chin, S. McMaster, W.V. Prestwich, S.H. Byun, Relative Enhancement of a ^{3}He Ion Chamber Response to Fast Neutrons by TOF Rejection of Slow Neutron with a Pulsed Neutron Source, IEEE Trans. on Nucl. Sci., 2009; 56: 266-271.

Chapter 4 - W. Matysiak, D.R. Chettle, W.V. Prestwich, S.H. Byun, Optimization of the proton chopper for ^{7}Li(p,n) neutron spectrometry using a ^{3}He ionization chamber, submitted for publication in Nucl. Instr. Meth. A, March 10, 2010

Chapter 6 - W. Matysiak, W.V. Prestwich, S.H. Byun, Precise measurements of the thick target neutron yields of the ^{7}Li(p,n) reaction, submitted for publication in Nucl. Instr. Meth. A, March 24, 2010 the proton beam line. The carbon deposition lowers the neutron production rate by making the incident proton beam partially lose its energy in the carbon layer prior to reaching the lithium itself.

For a given incident proton energy, the neutron production covers from the incident to the threshold energy as the proton loses its energy within the lithium target. Therefore, both neutron yield and spectrum are sensitive to the incident proton energy. Many studies have been performed to optimize the neutron spectrum for *in vivo* neutron activation analysis (Arnold, McNeill, Prestwich, & Chettle, 2000; Pejović-Milić, Arnold, McNeill, & Chettle, 2000) or boron neutron capture therapy (Allen, Beynon, Green, & James, 1999; Bleuel, Donahue, Ludewigt, & Vujic, 1998; Lee & Zhou, 1999) by combining the neutron producing target with a proper moderator and reflector.

In a typical arrangement, the lithium metal is mounted on a metal backing equipped with water cooling channels, facilitating the heat removal in order to prevent the lithium from melting. However, additional components of the target assembly provide scattering centers for neutrons, thereby disturbing the original neutron energy spectrum and angular emission directions. Also, the experimental area has to be protected with walls, so therefore room-return neutrons may also contribute to the departure of the measured spectra from the theoretically predicted shape. The contribution of these factors can be partially accounted for by carefully modeling the experimental arrangement using Monte Carlo simulation, but experimental verification of the results is always necessary.

1.2. The ^{7}Li(p,n) reaction

The ^{7}Li(p,n) reaction has a threshold of ~ 1.88 MeV, a broad resonance at 2.25 MeV, and up to 2.4 MeV, ^{7}Li(p,n)^{7}Be is the only channel open for neutron emission. Liskien and Paulsen (Liskien & Paulsen, 1975) measured the cross-section of the reaction in the incident proton energy range up to 7 MeV. Figure 1.1 shows the cross-section in the incident proton energy region from threshold to 2.4 MeV measured by three research groups.

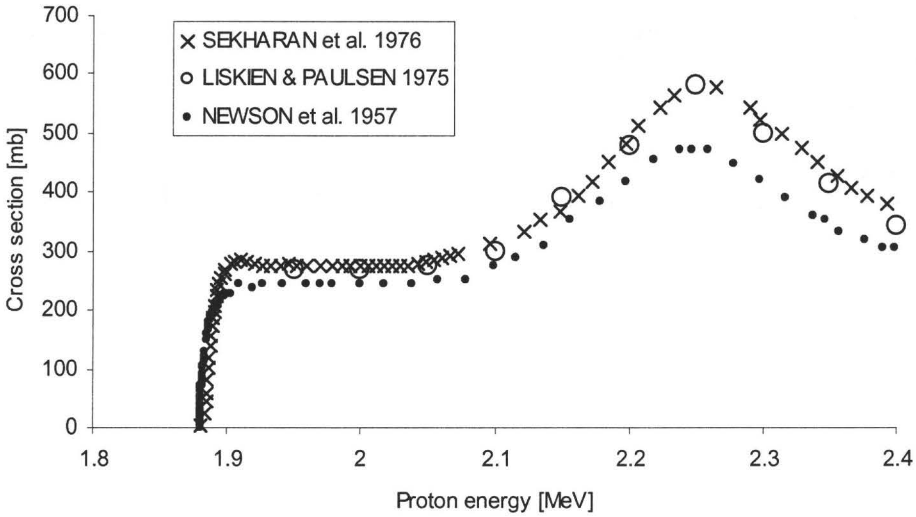

Figure 1.1: The ^{7}Li(p,n) cross-section as a function of the incident proton energy (Liskien & Paulsen, 1975; Newson, Williamson, K. W. Jones, Gibbons, & Marshak, 1957; Sekharan, Laumer, Kern, & Gabbard, 1976).

In this work, the Liskien and Paulsen cross-section data were used. The angular distribution of neutron emission in CMS is given in the same publication (Liskien & Paulsen, 1975) as a set of tabulated coefficients (*A*) of Legendre polynomials (*P*) for the same incident proton energy range (Figure 1.2):

$$\left(\frac{d\sigma}{d\Omega}\right)(\theta) = \left(\frac{d\sigma}{d\Omega}\right)_{CMS}(0^\circ)\sum_{i=0}^{2} A_i P_i(\cos(\theta)).$$

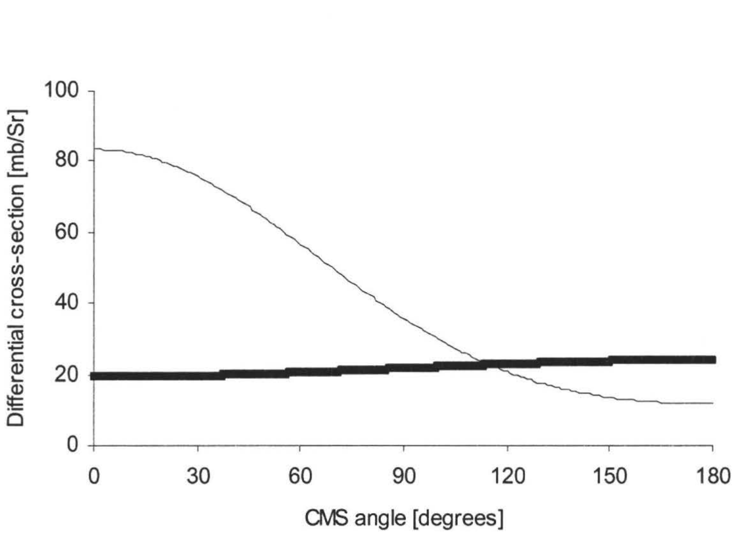

Figure 1.2: Angular distribution of the ^{7}Li(p,n) differential cross-section in CMS for two example proton energies: 1.95 (thick line) and 2.3 MeV (thin line) (Liskien & Paulsen, 1975).

The ^{7}Li(p,n) reaction rate per proton path length dx for a proton current i_p into a $\vec{\Omega}_{CMS}$ direction in the CMS within solid angle $d\Omega_{CMS}$ is expressed as (Arnold et al., 2000) $d\dot{Y} = \frac{i_p}{e} n_{Li} \left(\frac{d\sigma}{d\Omega}\right)_{CMS} d\Omega_{CMS} dx$, where n_{Li} and e denote ^{7}Li number density and the electronic charge, respectively. The differential path length dx can be converted into the differential energy of proton (E_p) using the stopping power $S(E_p)$ of Li for protons: $dx = \frac{dx}{dE_p} dE_p = -\frac{1}{S(E_p)} dE_p$. The stopping power data were obtained from the SRIM data library (Ziegler, 2006). Finally, the transformation of the reaction coordinates from CMS to laboratory system yields: $\frac{d^2\dot{Y}}{dE_n\, d\Omega} = \frac{i_p}{e} n_{Li} \left(\frac{d\sigma}{d\Omega}\right)_{CMS} \frac{d\Omega_{CMS}}{d\Omega} \frac{dE_p}{dE_n} \left(-\frac{1}{S(E_p)}\right)$, where E_n is the neutron energy and Ω is the solid angle in the laboratory system.

Because the reaction is double valued close to the threshold, the $\frac{d\Omega_{CMS}}{d\Omega}$ and $\frac{dE_p}{dE_n}$ elements cannot be evaluated separately in the whole E_n and Ω range, because in a specific region of E_n and Ω values, the product is indeterminate. Instead, the product of the two factors can be evaluated jointly as proposed by Lee and Zhou (Lee & Zhou, 1999). Another practical difficulty in evaluation of the reaction stems from the fact that the differential cross-section was fully evaluated only above 1.95 MeV and the analytical model runs into a singularity when the proton energy approaches the reaction threshold. Instead, an approximation has to be used (Ritchie, 1976).

The information outlined above is sufficient to evaluate the double differential neutron yield formula numerically and the Matlab package (MathWorks Inc, 2008) was employed for the task. Figure 1.3 shows the double differential neutron yield calculated for an example proton energy of 2.3 MeV, and Figure 1.4 shows maximum neutron energy and emission angle contours calculated using the double differential neutron yield.

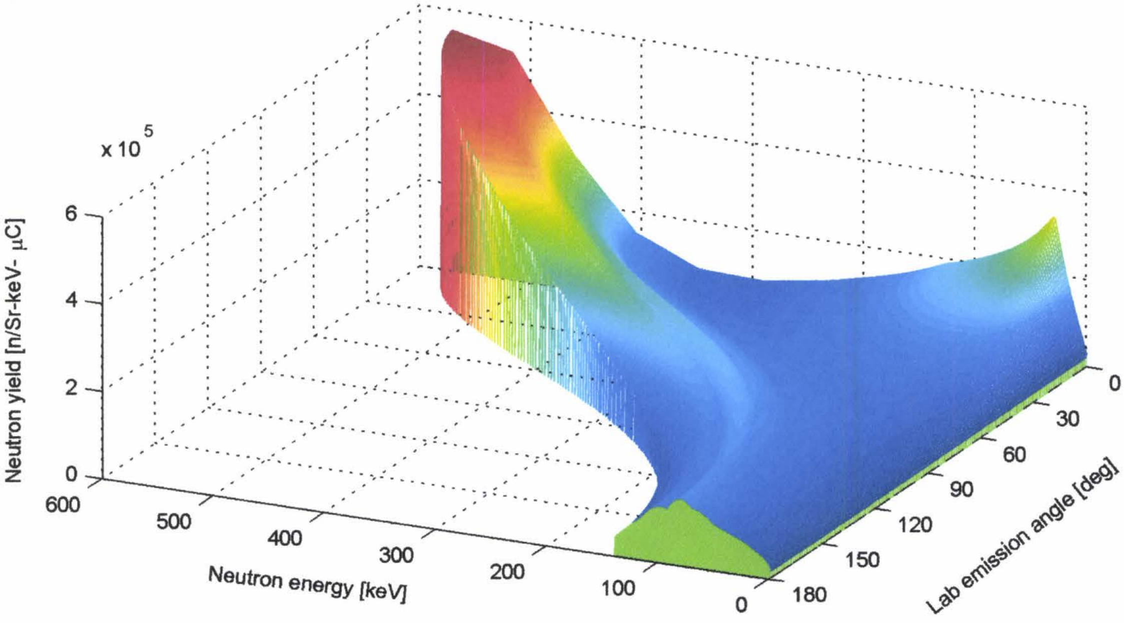

Figure 1.3: Double differential neutron yield of the ^{7}Li(p,n) reaction for an example proton energy of 2.3 MeV.

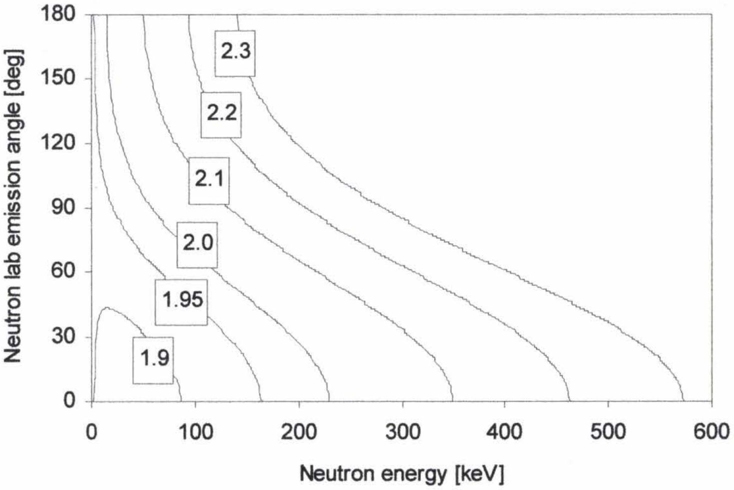

Figure 1.4: Maximum neutron emission angles and energy contours for incident proton energies between 1.9 and 2.3 MeV.

The double differential formula allows for calculation of the neutron spectra in real experimental conditions by integration over areas limited by polar and azimuthal angles: $\frac{dY}{dE_n}(E_n) = \int_0^{\varphi_{\max}} \int_0^{\theta_{\max}} \frac{dY}{dE_n}(E_n)\sin(\theta)d\theta d\varphi$. In this work, this formulation was used to calculate neutron spectra over the ^{3}He detector area (see Figure 1.5).

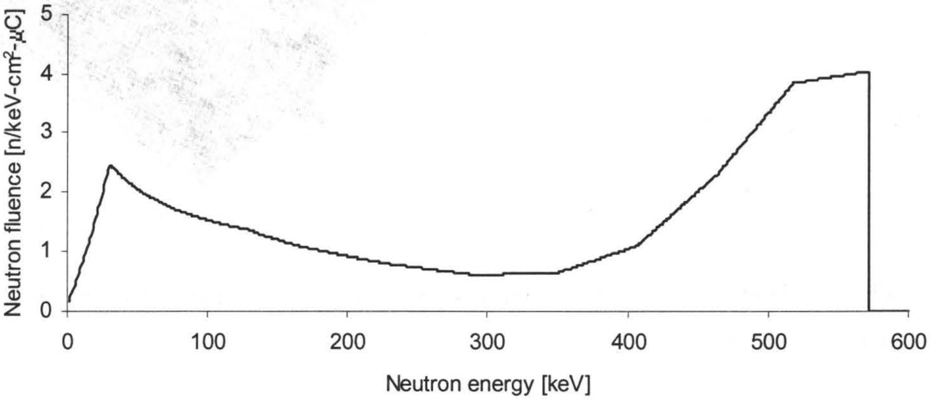

Figure 1.5: Neutron fluence over the ^{3}He detector area calculated for an example incident proton energy of 2.3 MeV. The detector is positioned perpendicularly to the proton beam axis at a distance of 3.7 m in the forward direction.

The Matlab script was also used to output the double differential distribution in the format accepted by MCNP scripting language, which therefore allowed for automated generation of MCNP source cards.

1.3. Motivation for the study

Given that optimizing the neutron irradiation field relies heavily on the raw neutron spectra, accurate characterization of the ^{7}Li(p,n) neutron fluence spectra is of great importance for all ^{7}Li(p,n) neutron beam users, and the raw spectrum from the lithium target is no doubt important information regardless of ultimate applications. Until now, most studies have relied only on theoretical spectra, which were calculated using the ^{7}Li(p,n) cross section and the lithium stopping power for protons (Arnold et al., 2000; Lee & Zhou, 1999). Although some measurements of thermal and epithermal neutron fluence rates were reported for moderated neutron beams (Arnold et al., 2002; Lee et al., 1999), there are few publications reporting the experimental neutron spectra directly from thick target ^{7}Li(p,n) neutron sources. Thus, the primary objective of this study was to measure the thick target ^{7}Li(p,n) neutron spectra for various incident proton energies.

1.4. ^{3}He neutron detector

There are several methods to measure the neutron spectrum (Brooks & Klein, 2002). The neutron detector used in this study is a gridded ^{3}He ionization chamber of the Shalev-Cuttler type (FNS-1, Seforad Applied Radiation Ltd., Israel) with a cylindrical active volume of 5 cm in diameter by 15 cm in length. To achieve a high detection efficiency, the detector was filled with 6 atm ^{3}He. Argon (3 atm) and methane (0.5 atm) were added for proper operation.

The ^{3}He ion chamber offers good energy resolution for neutrons with energies above approximately 30 keV (Beimer, Nyman, & Tengblad, 1986; Iguchi, Nakayamada, Takahashi, & Nakazawa, 1994; Loughlin, Adams, & Sadler, 1990; McFee, 1977). The ^{3}He(n,p)T reaction, which constitutes the main interaction of neutrons with the detector, has a cross-section of less than 1 barn for 100 keV neutrons and 5330 barns for 25 meV neutrons. The Q-value of the reaction shifts the deposited kinetic energy of neutrons in the detector upwards by 764 keV. Due to the extremely large cross-section of the ^{3}He(n,p) reaction at thermal energies, even a weak thermal neutron fluence rate can produce a significant counting rate in the detector, which may lead to a serious pile-up problem. Therefore, the detector chamber is surrounded by a slow neutron shield composed of a 2 mm-thick boron nitride and 0.5 mm-thick cadmium layer. Even with the shield, the epithermal peak is a dominant feature in measured spectra, because epithermal[♣] neutrons above ~ 1.0 eV penetrate the shield and create an intense peak corresponding to the 764 keV Q-value in measured spectra. Although not caused by thermal neutrons, the peak is often termed the "thermal peak", but in order to recognize its origin, in this study it is referred to as the "epithermal peak". Since the energy resolution of the detector at 764 keV is ~ 15 keV in FWHM, even neutrons up to a few kiloelectronvolts can be scored in the epithermal peak. Hence, neutron spectrometry with the ^{3}He ion chamber is limited down to approximately 30 keV. The spectral information for the epithermal region can be measured using other methods, e.g. time-of-flight spectrometry.

The ^{3}He ion chamber has been employed in a variety of applications (Franz et al., 1977; Loughlin et al., 1990; Ohm, Kratz, & S.G. Prussin, 1987), but there are a number of difficulties when working with this detector. The maximum counting rate is limited to approximately 1,000 cps due to slow charge carrier collection, with the majority of all counts scored in the epithermal peak. The peak fraction of the detector response is not 100 %, therefore spectral unfolding is necessary to prevent overestimation of the part of the spectrum below the maximum neutron energy, especially for measurements where high neutron energies are expected. However, the use of the detector response function in the unfolding process is limited only to the part above the epithermal peak. This is due to the fact that when attempting the unfolding process using the full response, the unfolding result is mostly governed by the size of the epithermal peak, which makes the process unstable. An iterative unfolding algorithm compares the measured spectrum with the solution spectrum folded with the response function after each step of iteration. When the complete response function is employed in unfolding, the difference between the measured and modeled spectra is mostly governed by the epithermal peak due to its relative size. If the epithermal peak counting rate is sufficiently reduced so that the difference between the epithermal

---

[♣] For convenience, neutron energies in this study have been sorted as thermal (E_n<0.5 eV), epithermal (0.5 eV<E_n<30 keV), and fast (E_n>30 keV).

peak and the rest of the spectrum is not so significant, the complete detector response can be used in the unfolding process.

1.5. Proton chopper

From the Monte Carlo simulation of the energy dependent efficiency of the ^{3}He ionization chamber (Matysiak, Prestwich, & Byun, 2008), it was identified that the detector efficiency is at a maximum at ~ 10 eV and is relatively high in the whole neutron energy region from 1 eV to 100 eV. The detection events corresponding to the epithermal peak are mainly caused by these incident neutrons, which penetrate the detector neutron shield. Therefore, these neutrons must be rejected in order to solve the interference problem of the epithermal peak. With a continuous neutron beam, the only potential way to separate epithermal neutron events from fast neutron events would be through pulse shape analysis. However, it is not clear how much difference is present between the pulse shapes of epithermal and fast neutron ^{3}He(n,p) events, although ^{3}He recoil events can be efficiently rejected when pulse shape analysis is employed (Evans & Brandenberger, 1979).

With a pulsed neutron beam, rejection is more straightforward. Epithermal neutrons can be rejected based on their flight time, so therefore the size of the epithermal peak is reduced in measured spectra. In this case, the requirement of a short pulse width and a long flight length is not as critical as in conventional time-of-flight spectrometry, since time information is used only for gating the ^{3}He spectrometer instead of for accurate measurement of flight time. The simplest way to create a pulsed neutron beam is to chop the incident proton beam periodically, which leads to repeated production of a neutron bunch. In this study, development of a proton chopper system, the so-called electrostatic chopper (Taccetti et al., 2002; Fifield, Tims, Gladkis, Morton, & Barrows, 2006; Berkovits et al., 2004; Draxler, Gruber, & Bauer, 2003), is reported. Two different chopper high-voltage supplies were developed and their performances evaluated. Test measurements of the ^{3}He ionization chamber with the pulsed neutron beam are also reported.

Following the development of the proton chopper, systematic investigation of the dependence of the chopper performance on its operational parameters was carried out. The diagnostics of the pulsing system aims at ensuring that the neutron spectra acquired with the pulsing system are equivalent in neutron yield and spectral content above the slow neutron rejection threshold with neutron spectra acquired in the continuous current mode. First, it is important to ensure that the coincidence window of the pulse processing system is well aligned with the proton pulse so that fast neutrons produced in the burst can reach the detector and be analyzed by the pulse processing chain within that coincidence window interval. Next, linearity between the proton current incident on the lithium target and the number of detected events has to be verified in order to see if the dead time of the system is significant in the operating range of the proton currents. Finally, the neutron spectra collected in the pulsed mode should be compared with the neutron spectra acquired in the continuous current mode in order to verify that the fast neutron yield is equivalent in the two modes, thus allowing for absolute neutron fluence measurements in the pulsed mode. Under the optimized proton pulsing condition, neutron spectra can be collected and analyzed.

Based on the measured neutron spectra, total neutron kerma can be calculated using fluence-to-kerma coefficients (Chadwick et al., 1999). In order to verify the ^{3}He chamber dose measurements in the absolute sense, the microdosimetric technique with the tissue equivalent proportional counter (TEPC) was applied. Two detectors, ½" and 5" (LET-SW1/2 and LET-SW5, Far West Technology), both simulating a 2 micrometer sphere were employed. Both are equipped with a built-in alpha-emitting source for easy lineal energy calibration.

1.6. Neutron yield of the ^{7}Li(p,n) reaction

Many groups reported experimental thick target ^{7}Li(p,n) neutron yield data and found significant discrepancies between theoretical and experimental yields (Aslam, Prestwich, & McNeill, 2003; Lee et al., 1999; Yu, Yue, Han, Chen, & Tian, 1998). The theoretical neutron yields in all these studies assumed a pure metal lithium target and no attempts were made to correct for the perturbation effects such as target oxidation or carbon deposition. The corrections for these effects are difficult because quantitative information on oxide and carbon layers is hard to estimate. For the neutron yield near threshold, there is another factor to be taken into account. The ^{7}Li(p,n) cross-section in this region changes rapidly therefore, the proton energy stability plays an important role. To account for large discrepancies (30 % to a factor of 2) between theoretical and experimental yields, Aslam (Aslam et al., 2003) attributed them to the oxidation effect, while Lee (Lee et al., 1999) attributed them to the proton energy spread.

In this study, as a simple way of accounting for all these perturbation effects, the effective incident proton energy was determined from the measured maximum neutron energy. The neutron spectrum was acquired using a ^{3}He ion chamber. The measurements were conducted for five different nominal (see Ch. 5) proton energies from 1.95 MeV to 2.3 MeV, so that the effect of finite proton energy spread can be compared for regions where the yield varies rapidly with proton energy versus regions where the yield is relatively slowly varying.

Chapter 2

MEASUREMENT OF THE THICK TARGET ^{7}Li(p,n) NEUTRON SOURCE SPECTRUM USING A ^{3}He IONIZATION CHAMBER

2.1. Summary

In this chapter, the properties of the ^{7}Li(p,n) accelerator based neutron source and the neutron detection system based on the ^{3}He detector are investigated.

First, two types of pulse processing systems were used for neutron spectra acquisition: an analog pulse height analyzer based on CR-(RC)^2 shaping connected to a peak sensing ADC and a digital system with trapezoidal shaping. The performance of the two systems was compared and it was concluded that the digital system gives better energy resolution consistently and that its pile-up rejection system is more effective.

Next, the iterative unfolding algorithm was presented and its performance evaluated using analytically generated functions. The algorithm adequately restored a step function, but it was not capable of unfolding the raw spectrum including the epithermal peak due to its relative size. As a solution, only the part of the spectrum above 794 keV (above 30 keV neutron energy) can be used for unfolding to avoid interference of the epithermal peak.

Finally, efficiency and wall effect in the detector were investigated. The detector efficiency was modeled using the MC method, and a factor-of-two discrepancy was identified between the simulated and experimental results. The wall effect was investigated using an analytical model, and the MC simulated efficiency was corrected to reflect this phenomenon. The effectiveness of slow neutron shielding was also modeled and a conclusion was reached, that the most

significant contribution to the epithermal peak comes from neutrons of energies in the region between approximately 1 and 100 eV.

It was concluded therefore, that if the slow neutron events can be rejected, the height of the epithermal peak may be significantly reduced and the full detector response, i.e. not only the part above 794 keV, can be employed in the spectral unfolding process.

The content of this chapter has been published in Nuclear Instruments and Methods Section A. The manuscript was prepared by me and revised by co-authors. The introduction and conclusion sections of the paper were removed to avoid redundancy with the information contained in the introduction and conclusion chapters of this thesis. Section numbers and the reference system were adjusted to conform to the referencing style used in the thesis. The bibliography is presented at the end of the thesis.

Measurement of the thick target ^{7}Li(p,n) neutron source spectrum using a ^{3}He ionization chamber

W. Matysiak[1], W.V. Prestwich[1] and S.H. Byun[1]

[1]Medical Physics and Applied Radiation Sciences, McMaster University, Hamilton, Ont., Canada L8S 4K1

Received 20 January 2008, in final form 15 March 2008.

Published in *Nuclear Instruments and Methods in Physics Research Section A: Accelerators, Spectrometers, Detectors and Associated Equipment*, 2008; 592: 316-324.

Online at dx.doi.org/10.1016/j.nima.2008.03.110.

2.2. Experiments

2.2.1. The neutron source

[…] A thick lithium target was installed at the McMaster KN accelerator, which mainly serves as either a neutron or a photon source for medical and radiobiological applications. The KN accelerator can deliver protons up to 2.35 MeV with a maximum current of ~ 80 μA. The layout of the target assembly is shown in Figure 2.1.

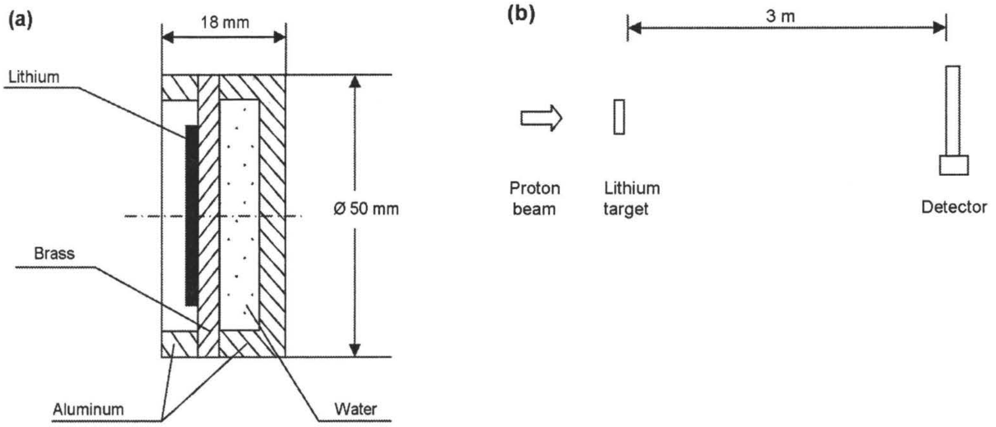

Figure 2.1: (a) Lithium target holder assembly and (b) ^{3}He ionization chamber arrangement.

The assembly is composed of a brass support plate with a few millimeter layer of natural lithium metal mounted on it. The brass plate is cooled with a water cooling system and the cooling capacity is sufficient up to the maximum proton current.

Table 2.1: Proton energies and currents used in the experiment.

Proton energy	Proton current	Count rate	Dead time
[MeV]	[μA]	[cps]	[%]
1.95	3.0	616	<2
2.0	1.0	617	<2
2.1	0.7	640	<2
2.2	0.5	672	<2
2.3	0.4	719	<2

The proton energy was varied from 1.95 to 2.30 MeV as listed in Table 2.1. This energy range covers the near threshold to the peak of the resonance of the ^{7}Li(p,n) reaction. As was observed, the detector can handle counting rates only up to approximately 1,000 cps without significant pulse pile-ups, therefore proton current was maintained between 0.4 and 3.0 μA to prevent the problem. The ^{3}He detector was positioned at three meters from the lithium target along the proton beam axis to keep pulse pile-up as low as possible.

2.2.2. The detector and electronics

[...] The detector was operated with an anode bias at + 3 kV and a grid bias at + 850 V as recommended by the manufacturer. The preamplifier output signal was split and processed by both an analog pulse height analyzer and a digital pulse processing system to compare their performances.

The analog system consisted of a shaping amplifier and a peak-sensing ADC. Due to a notable spread in pulse rise time distribution of the ^{3}He ionization chamber, the choice of the shaping time constant is important to achieve a satisfactory energy resolution. In this study, the optimum shaping time was determined through the observation of the epithermal peak resolution by varying the shaping time of the amplifier. A shaping time of 4 μs gave the best resolution consistently. The peak-sensing ADC used was a successive-approximation type

(ORTEC, TRUMP-PCI) with a conversion time of 8 μs. A conversion gain of 1024 channels was selected.

For digital pulse processing, a commercial digital signal processor (ORTEC, DSPEC PLUS) was used. The preamplifier output signal was directly digitized and the pulse form was shaped with the trapezoidal method. A rise time of 8 μs, which is equivalent to the shaping time of 4 μs in the CR-(RC)^2 analog shaping, showed the best energy resolution. The flattop was set at 2 μs. The pile-up rejection was always activated in the digital system while it could not be implemented in the analog system due to the difference in standardization between the shaping amplifier and the peak-sensing ADC.

Figure 2.2 shows spectra measured with the two pulse processing systems at the incident proton energy of 2 MeV. For convenience, the spectrum of the analog system was shifted vertically. It is apparent that the pile-up rejection of the digital system works properly except for a few events recorded at the sum peak position of the epithermal peak. Moreover, the digital system shows an enhanced epithermal peak resolution due to more complete charge collection used by trapezoidal shaping. Table 2.2 lists epithermal peak resolutions observed at different proton energies. The digital system consistently gave better resolution due to combined effects of the trapezoidal shaping and better pile-up rejection. Therefore, spectra accumulated with the digital system were used in further unfolding process.

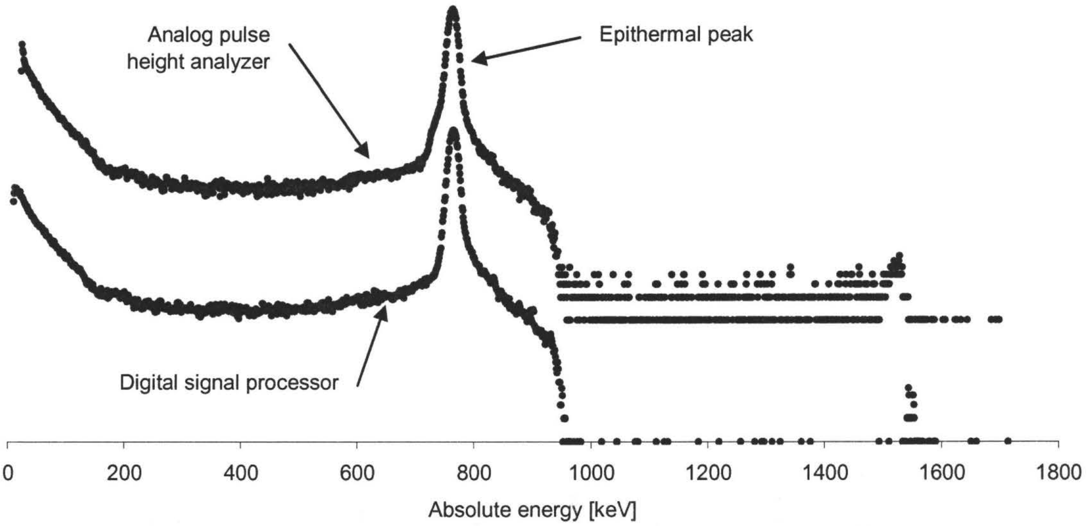

Figure 2.2: Spectra measured with the ^{3}He spectrometer for 2.0 MeV proton energy using digital and analog pulse processing systems.

Table 2.2: Epithermal peak resolutions for analog and digital pulse processing systems.

Proton energy	FWHM	
	Digital system	Analog PHA
[MeV]	[keV]	[keV]
1.95	15.49	16.08
2.0	15.38	16.05
2.1	15.17	15.83
2.2	15.41	16.04
2.3	15.56	16.30

2.3. Spectrum analysis: unfolding

2.3.1. The response function

The experimental response function of the Shalev-Cuttler type ^{3}He ionization chamber was reported by Beimer (Beimer et al., 1986) and Loughlin (Loughlin et al., 1990). Monte Carlo calculations of the response function were reported by others as well (Sailor, Prussin, and Derzon 1988; Iguchi et al. 1994), however, significant adjustments were required to match the calculated to the experimental response functions.

Beimer produced a library of the detector responses in the neutron energy range of 130 ~ 3030 keV. For each mono-energy neutron beam, both epithermal peak and gamma-ray events were subtracted from the measured spectrum in order to include only fast neutron events and subsequently fitted into a function with sixteen parameters. Loughlin reported a similar response function measurement in the neutron energy region of 2.0 to 3.0 MeV. Since Beimer's response function covers most of the spectral range of our interest, it was adopted and used for the unfolding process in this study.

A complete detector response includes features which vary with experimental conditions, i.e. the epithermal peak and the gamma-ray continuum, which must not be included in the model of response function. Beimer suggested subtracting both the gamma-ray continuum and the epithermal peak from experimental spectra: the former by fitting an exponential function and the latter by finding epithermal peak shape from an independent experiment and subtracting it from measured spectrum. This technique, however, is effective only for neutrons in the MeV region. In our spectral region, the neutron spectrum is expected to vary smoothly from thermal energies to approximately a few hundred keV. Subtracting the epithermal peak in these conditions produces unstable results. Moreover, additional factors such as the gamma-ray contamination and the wall effect continuum originating from slow neutron interaction events make the subtraction even more difficult. Therefore, the low energy part of response function below the epithermal peak was not used in unfolding.

2.3.2. Detector efficiency

The phenomena of incomplete charge collection and wall effect make peak efficiency definition problematic for the ^{3}He ionization chamber. In other words, not all full-energy absorption events are scored into the full-energy peak due to wide distribution of the charge collection time or due to secondary charged particles depositing part of their kinetic energy in detector walls.

To validate the experimental efficiency data partly, Monte Carlo calculations were performed with the MCNP5 (Briesmeister, 1997) code using the SHARCNET computing network (http://www.sharcnet.ca), in the neutron energy range of 10 keV ~ 1 MeV. The comparison between the calculated and the published experimental efficiencies was made in terms of the peak efficiency instead of the total efficiency due to the fact that transport of the secondary particles, i.e. recoil proton and triton which contribute to the partial energy deposition events, can not be simulated with the current version of MCNP. The detector geometry was implemented into the input file of the program and the ^{3}He(n,p) reaction rate in the detector active volume was calculated with the *FM*4 tally for mono-energetic neutrons. Angular distribution of the neutron source was assumed to be isotropic and the source-to-detector distance was set at 1 meter for efficiency calculations.

The wall effect caused by the secondary particles was estimated using a simple method. At each point in the detector active volume, proton and triton emission directions were assumed to be opposite in the laboratory system and their energy losses in the active volume were analytically calculated using the range and the stopping power data (Ziegler, 2006). An example of the wall effect for 100 keV neutrons is shown in Figure 2.3. If the total energy deposition was higher than 90 % of the incident neutron energy, that event was scored as a full energy deposition and included in the full-energy peak.

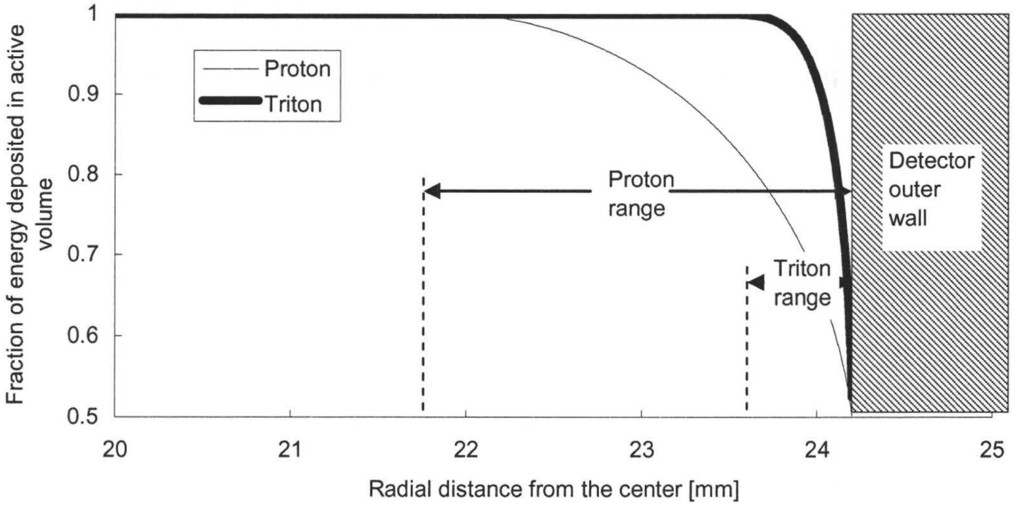

Figure 2.3: Wall effect in ^{3}He detector caused by reaction products following 100 keV neutron capture.

It turned out that the Monte Carlo efficiency overestimates Beimer's experimental results (Beimer et al., 1986) by a factor of two. As it has already been mentioned, the incomplete charge collection in the chamber most likely caused this discrepancy. Figure 2.4 shows the experimental (Beimer et al., 1986) and the calculated peak efficiencies. The calculated efficiency was scaled down so that it matches the experimental data at 200 keV. It is obvious that the energy dependencies of both efficiencies are quite similar.

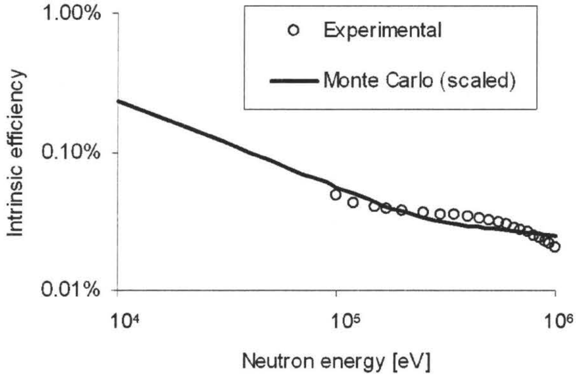

Figure 2.4: Monte Carlo simulation of the detector efficiency corrected for wall effect (solid line) and experimental data (Beimer et al., 1986) (open circles).

[...] The slow neutron shield of the detector becomes less effective with increasing neutron energies. In order to investigate the performance of the thermal shielding, the MCNP simulation was extended to the very low energy region. Figure 2.5 shows the calculated efficiency in low energy region. Due to the fact that the cadmium and boron neutron capture cross-sections at lower energies are very high, the probability of a neutron penetrating the shield and interacting in the active volume is extremely low.

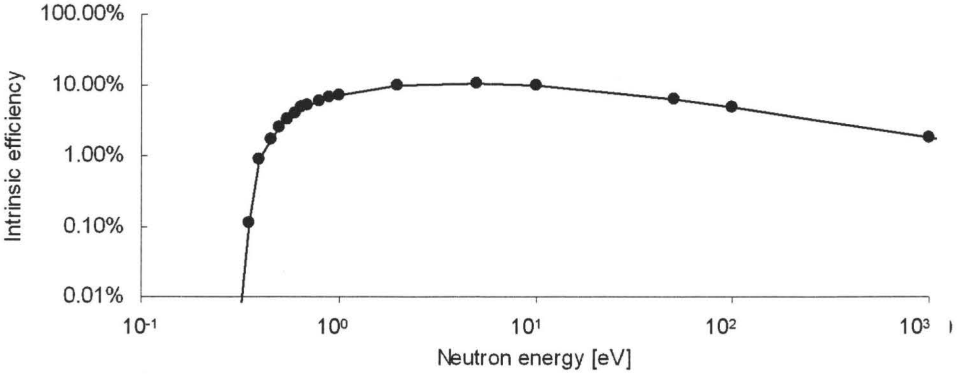

Figure 2.5: Calculated intrinsic peak efficiency in the low energy region.

From the figure, it is straightforward that the main contribution to the epithermal peak comes from neutron energies of approximately 10 eV. Above this region, the neutron shield is not effective and does not significantly distort the incident spectrum. However, the relatively wide (approximately 15 keV FWHM) and intense epithermal peak makes it impossible to resolve neutrons with energies up to several keV.

2.3.3. Unfolding algorithm

Given that $R(E,E_n)$ is the detector response function at an incident neutron energy E_n, the measured spectrum $M(E)$ can be expressed as

$$M(E) = N(E) + \int R(E,E_n)\Phi(E_n)dE_n \tag{2.1}$$

where $N(E)$ denotes random noise and $\Phi(E_n)$ the incident neutron fluence spectrum. Since the measured spectrum and the response function are available in discrete bins, the above formula is usually converted into a matrix equation

$$\mathbf{M} = \mathbf{N} + \mathbf{R\Phi} \tag{2.2}$$

This equation is ill-conditioned therefore solving it produces unstable results when direct inversion is attempted due to the nature of the response matrix. For that reason, a group of iterative methods has been used in practice. Historically, the first such method was proposed by van Cittert (van Cittert, 1931). Jansson (Jansson, 1995) as well as others proposed modified versions.

Van Cittert's algorithm reads

$$\Phi_i^{k+1} = \Phi_i^k + b(M_i - \sum_j R_{ij}\Phi_j^k) \tag{2.3}$$

where superscript k denotes k^{th} iteration step and a constant b is adjusted to meet convergence criteria (Xu, Aissaoui, & Jacquey, 1994). Van Cittert's algorithm does not prevent a solution spectrum from having negative elements, therefore it has not been employed in situations like this study, where a non-negative solution must be guaranteed.

Janssons's algorithm introduces a relaxation function μ as

$$\Phi_i^{k+1} = \Phi_i^k + \mu_i^k(M_i - \sum_j R_{ij}\Phi_j^k) \tag{2.4}$$

where μ is defined as $\mu_i^k = b\left(1 - 2/c\left|\Phi_i^k - c/2\right|\right)$, with constants b and c depending on physical bounds of the collected dataset. The relaxation function gradually applies corrections so that all elements of vector Φ^{k+1} are expected to occur between a minimum and maximum value imposed by the function. In this study, Jansson's algorithm was chosen for the unfolding analysis.

After each iteration a root mean square error function was calculated as

$$RMSE = \sqrt{\sum_i \left(M_i - \sum_j R_{ij} \Phi_j^k \right)^2} \tag{2.5}$$

Iterations were interrupted when the change in RMSE in subsequent iteration steps was less than 1%, which was found to be a balance between a large number of iterations producing spurious peaks in solution spectrum, and a smaller number showing inadequate restoration of the spectrum.

Before analyzing measured spectra, the unfolding algorithm was tested with an ideal continuous spectrum to evaluate its reliability. A step function representing a neutron fluence spectrum was generated as shown in Figure 2.6 (a). The fluence spectrum was then folded with the response function. The result is shown in Figure 2.6 (b). To make the folded result more realistic, varying amounts of Gaussian noise were added in Figure 2.6 (c). Close comparison of this figure with Figure 2.7 reveals that the amount of random noise added is of similar order as the statistical fluctuations present in measured spectra.

As pointed out by Crilly (Crilly, 1990), a cross-correlation filtering used prior to unfolding with the Jansson method improves the signal to noise ratio of the unfolded spectrum and therefore, the observed spectrum was filtered using a single pass of cross-correlation filter with the Gaussian kernel using a standard deviation of 30 keV and length of 9 keV (1 keV per bin). Shorter filter window lengths do not effectively remove oscillations and longer windows contribute to smearing of the fast varying spectral features that is, the former act as a high pass filter, while the latter act as a low pass filter.

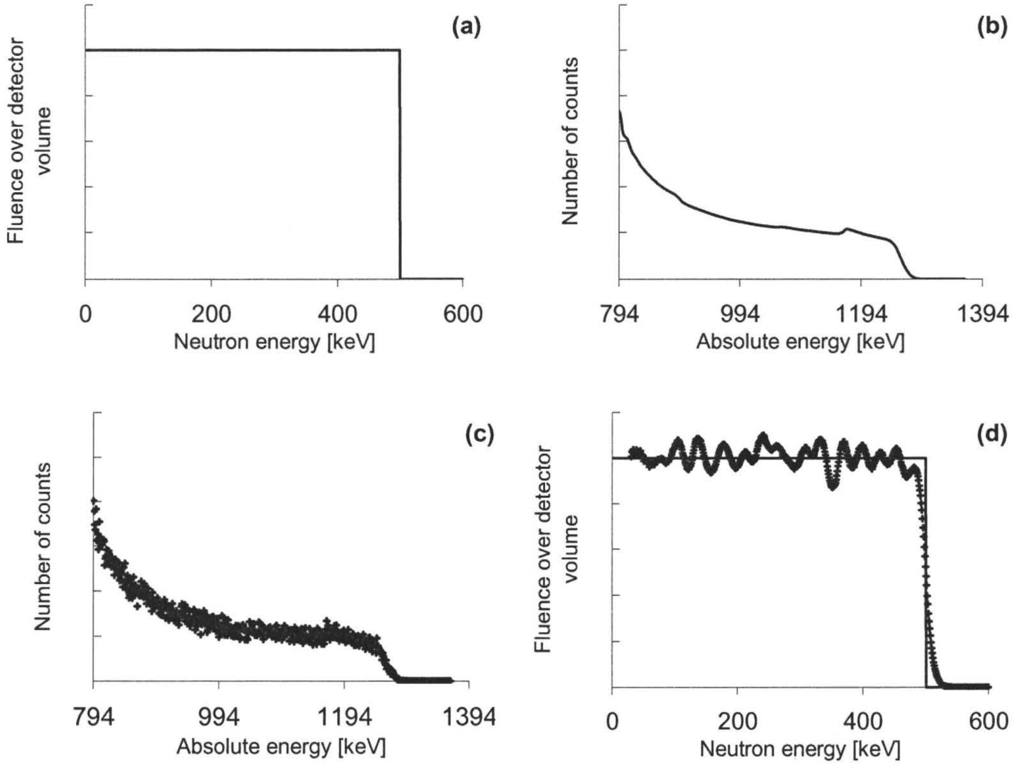

Figure 2.6: (a) Step function representing neutron fluence spectrum, (b) neutron spectrum folded with the detector response function, (c) Gaussian noise added, (d) unfolded (crosses) and source (solid line) spectra.

The unfolding algorithm does not impose any requirements on the first estimate of the unfolded spectrum, so the initial guess Φ^0 was estimated as

$$\Phi_j^0 = \frac{M_j}{\varepsilon(E_n)_j}$$ *

which is generally accepted in iteration processes. After 60 iteration steps the RMSE was no longer decreasing. The iteration was interrupted and the solution spectrum was filtered using the same kernel. The unfolded spectrum, Figure 2.6 (d), shows good agreement with the test-source spectrum of Figure 2.6 (a). Cross-correlation filtering with a relatively long window, smoothed fast oscillations in the result spectrum while leaving the low frequency portion.

---

[*] $\varepsilon(E_n)$ denotes energy dependent peak efficiency of the detector

2.4. Results

It is important to determine the minimum neutron energy limit below which, the incident neutron energy cannot be recovered. In the case of a ^{3}He detector this limit is set by the width of the epithermal peak, which is determined mainly by statistical fluctuations and the preamplifier noise. The epithermal peak can be approximated by a Gaussian. Therefore an arbitrary value of ± 2 FWHM gives five orders of magnitude reduction in number of counts. In measured spectra FWHM have values of approx. 15 keV, therefore a lower limit of 30 keV was adopted.

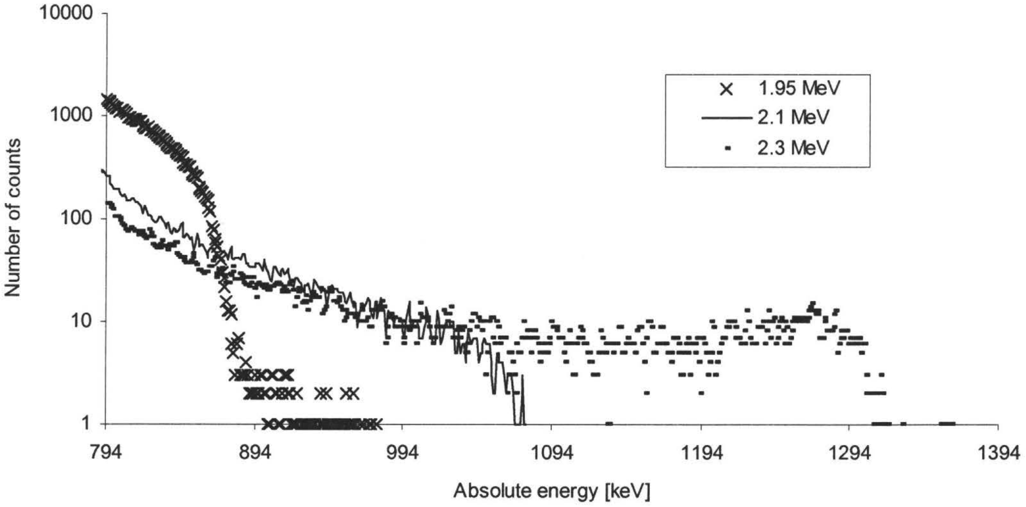

Figure 2.7: Neutron spectra measured with the ^{3}He ionization chamber for three selected proton energies.

Figure 2.7 shows the measured raw spectra above 794 keV for three selected incident proton energies. As the incident energy increases, the neutron energy is extended to the high energy side. The maximum neutron energy measured shows a systematic deviation from the theoretical calculation, which is discussed in detail later in this work. [...]

Chapter 3

RELATIVE ENHANCEMENT OF A ^{3}He ION CHAMBER RESPONSE TO FAST NEUTRONS BY TOF REJECTION OF SLOW NEUTRONS WITH A PULSED NEUTRON SOURCE

3.1. Summary

As presented in the previous chapter, the presence of the epithermal peak in neutron spectra measured with the ^{3}He ionization chamber makes it difficult to use the complete response function in an unfolding process. In order to reduce the epithermal peak counting rate significantly, an active method of rejecting low energy neutrons (< 180 eV) based on their time-of-flight is presented in this chapter. The method required a modification of the proton accelerator beam line in order to produce short pulses of protons.

Design considerations for two types of the proton chopper high voltage switches are presented: a prototype based on polarity reversal and a final design using fast switching. The performance of the two switches was evaluated by running the accelerator at 1.8 MeV (below the neutron production threshold) and observing prompt gamma-rays from the ^{7}Li(p,p'γ) reaction with a gamma-ray detector. The final design was chosen for further work because it showed a more rectangular pulse profile.

Initial measurements with the ^{3}He detector were taken and the ratio of the number of detection events above the epithermal peak to the number of events scored in the epithermal peak has been improved by a factor of 5.

The content of this chapter has been published in IEEE Transactions on Nuclear Science. The manuscript was prepared by me and revised by co-authors. The introduction and conclusion sections of the paper were removed to avoid redundancy with the information contained in the introduction and conclusion chapters of this thesis. Section numbers and the reference system were adjusted to conform to the referencing style used in the thesis. The bibliography is presented at the end of the thesis.

Relative Enhancement of a ^{3}He Ion Chamber Response to Fast Neutrons by TOF Rejection of Slow Neutrons with a Pulsed Neutron Source

W. Matysiak[1], K. Chin[1], S. McMaster[1], W.V. Prestwich[1], S.H. Byun[1]

[1]Medical Physics and Applied Radiation Sciences, McMaster University, Hamilton, Ont., Canada L8S 4K1

Received 29 May 2008, in final form 28 October 2008.

Published in *IEEE Transactions on Nuclear Science*, 2009; 56: 266-271.

Online at dx.doi.org/10.1109/TNS.2008.2008805.

3.2. Materials and methods

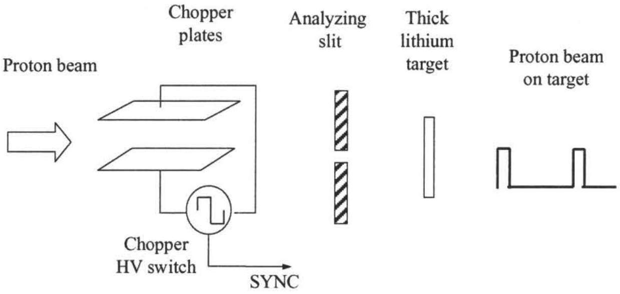

Figure 3.1: Schematic view of the proton chopper system. The incident proton beam passes chopper plates and is subsequently analyzed by the slit before hitting the lithium target. The chopper HV switching circuit produces a short SYNC pulse, which is used further to shape the coincidence window signal.

[…] Figure 3.1 shows a schematic diagram of the proton chopper system. The proton beam passes chopper plates and hits the analyzing slit. The chopper plates are 120 cm long aluminum plates located between the analyzing magnet of the KN accelerator and the lithium target. Fast square-shaped high voltage (HV) pulses are applied to the chopper plates from the switching circuit of the chopper HV supply. A SYNC logic pulse synchronized to the HV pulse is also generated so that it can be used to trigger a multichannel scaler (MCS) or a timing module.

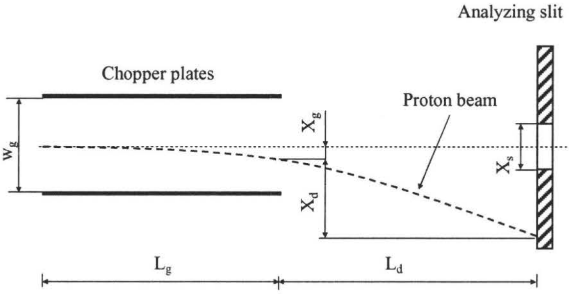

Figure 3.2 Dimensions of the proton pulsing system.

When the proton beam passes the chopper plates, the E-field acts upon the proton beam and deflects it in the vertical direction. The transverse position of the beam at the slit depends on the E-field strength and other parameters (Figure 3.2).

By periodically applying high voltage pulses, the proton beam hits the lithium target only for a short time per each period and neutron bunches are produced repeatedly. The repetition rate is set by the control panel of the HV switching circuit and is widely selectable from 0.02 Hz to 10 kHz.

In this study, two types of the HV switching circuit were built and evaluated. The prototype was based on the transient change in the E-field following DC polarity reversal induced by the driving circuit. Following prototype tests, a modified type was designed using a faster HV switching to position the beam so that it is either blocked by the analyzing slit or passes through it.

3.2.1. Prototype pulsing circuit based on polarity reversal

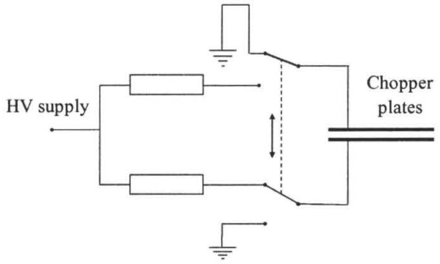

Figure 3.3: Schematic diagram of the prototype HV switching circuit.

In the prototype design, the HV switching circuit periodically reverses polarity of the plates as shown in Figure 3.3. During a transient period, electric potentials at both plates change simultaneously in the opposite way and the corresponding differential potential makes the proton beam scan from one end position to the other end position. The SYNC pulse is generated at the beginning of each polarity reversal phase. The E-field between the plates behaves according to the transient step response of the RC circuit as shown in Figure 3.4.

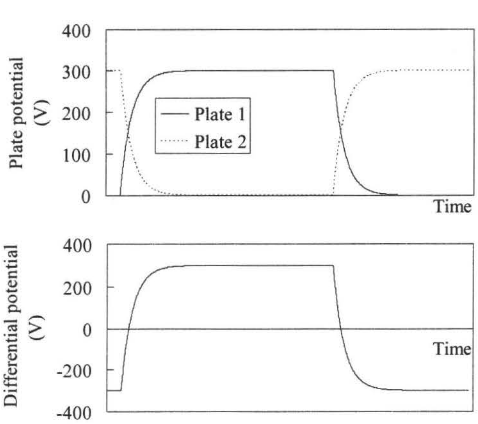

Figure 3.4: Potential change on deflector plates with respect to the common ground (top) and the differential potential between plates (bottom).

Transverse velocity of the proton beam at the exit of the plates is given by

$$v_x(t) = \frac{e}{w_g m_p} \int_t^{t+T_g} U(t')dt' \tag{4.1}$$

where e, m_p, and w_g are the elementary charge, proton mass, and plates separation (Figure 3.2) respectively. U is the potential difference between plates and varies as

$$U(t') = U_{\max}\left(1 - 2e^{-t'/\tau}\right) \tag{4.2}$$

at the rising phase. The time constant τ in (4.2) is determined by the load resistance of the HV supply (37 kΩ) and the summed capacitance of the chopper plates and the cable. A typical value of τ is

$$\tau = RC = 37\ k\Omega \cdot 1.3\ nF \approx 48\ \mu s\ . \tag{4.3}$$

T_g is the proton transit time in the chopper electric field and is given by

$$T_g = L_g \sqrt{\frac{m_p}{2E_p}}\ . \tag{4.4}$$

For the proton energy of E_p = 2 MeV and deflection plates of 1.2 m in length, it is 61 ns. Since this is a few orders of magnitude smaller than the rate of *U(t')* change, it can be assumed that the E-field is constant during passage of the proton beam and (4.1) is simplified to

$$v_x(t) = \frac{eT_g}{w_g m_p} U(t). \tag{4.5}$$

The total vertical deflection of the proton beam at the analyzing slit is a sum of its deflection within the plates and the constant velocity deflection during its flight between the chopper and the slit, and is given by

$$X(t) = X_g(t) + X_d(t) = \frac{eU(t)}{2E_p} \frac{L_g}{w_g} \left(\frac{L_g}{2} + L_d \right). \tag{4.6}$$

When designing the chopper system, the following constraints on its geometrical parameters have to be considered:

- high voltage switching circuits require specialized components, therefore keeping the DC voltage below approx. 350 V makes the design less complicated.
- the total length of the accelerator beam line which is available for modifications (L_g+L_d in Figure 3.2) is 4 m.
- maximum deflection of the proton beam on the slit plane must not exceed approximately 2 cm, otherwise the beam impinges on other elements of the beam line (such as the Faraday cup).
- the separation between the chopper plates must be small so that a strong electric field is produced for a given bias potential, but wide enough so that it does not unnecessarily complicate focusing of the proton beam. Knowing that the beam spot has a typical FWHM of approx 0.5 cm, a 2 cm minimum gap was found to give enough margin for undisturbed operations.
- the length of the plates must be such that the beam at its maximum deflection does not hit the surface of the plates. A chopper bias of 300 V applied to plates of 1.2 m in length separated by 2 cm deflects a 2 MeV proton by approximately X_g = 2.7 mm (Figure 3.2) from its axis, and then the deflection becomes 15 mm on the slit plane.

- since the FWHM of the beam is typically 0.5 cm, a slit size of less than 0.5 cm will not reduce the time width of the neutron pulse, but will only reduce the total current incident on the target which is undesirable, therefore a slit size of 0.7 cm was adopted.

By substituting the above parameters into (4.6) it was found that maximum deflection of the beam on the slit plane is 1.4 cm.

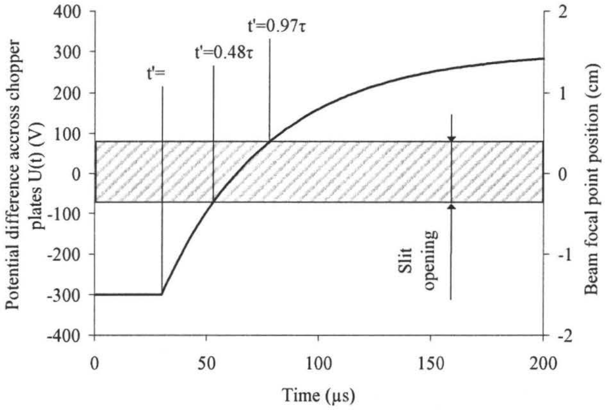

Figure 3.5: Proton opening at the analyzing slit.

Figure 3.5 shows the beam position on the slit plane as a function of time. At the time t'=0, the HV switch initiates polarity change and the electric field starts reversing. At $t'\approx0.48\tau$, the beam focal point meets the bottom edge of the slit and protons start hitting the lithium target. At $t'\approx0.97\tau$, the beam moves away from the slit opening and the whole proton current is again blocked by the slit. The time constant τ can be conveniently adjusted with the load resistor of the switching circuit. For values given in (4.3), protons are incident on the target for approximately 23 μs.

When positioning the ^{3}He ion chamber with respect to the source, following factors were taken into account:

- maximum proton current available and neutron yield
- minimum acceptable detector counting rate to acquire a spectrum of good statistical quality
- expected effective neutron low energy time-of-flight cut-off

The proton pulse repetition period (duty cycle) had to be adjusted so that low energy neutrons arriving at the detector from the previous neutron bunch do not interfere with fast neutrons of the next bunch. This time was determined by observing neutron events in the detector after the SYNC signal using the MCS. It was found that approx 1.7 ms after the signal the neutron intensity was not decreasing significantly, which agrees with the theoretical flight times for low energy neutrons. Therefore the proton duty cycle was chosen as 2 ms.

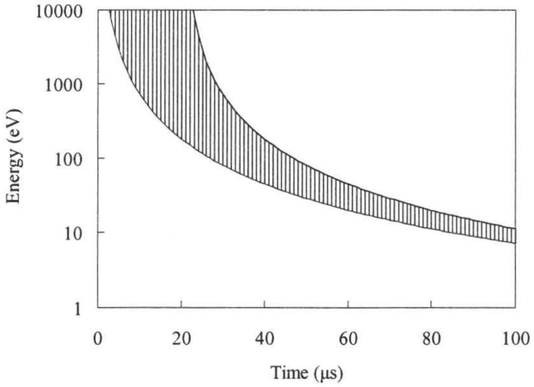

Figure 3.6: Minimum and maximum neutron energies observed by the detector following a 20 μs bunch of neutrons from the target at 3.7 m.

For the available target room flight length of 3.7 m, neutron energies E_n seen by the detector at time t following the neutron burst are given by

$$\frac{m_n L_f^{\ 2}}{2t^2} < E_n < \frac{m_n L_f^{\ 2}}{2(t-t_p)^2} \tag{4.7}$$

where m_n, L_f, and t_p are neutron mass, flight length, and proton pulse width respectively. For $t_p = 20$ μs, neutrons with energy lower than approx. 180 eV can be effectively discriminated against (see Figure 3.6).

The event rate detected by the ^{3}He ion chamber with the above settings and 60 μA continuous proton current, varied from approx. 20 cps for 1.95 MeV proton energy, to approx. 200 cps for 2.3 MeV, keeping pile-up at a sufficiently low level in the ion chamber.

3.2.2. Instrumentation and tests

The chopper power supply was placed close to the plates in order to keep the capacitance of connecting cables as low as possible. Since the signal rise time of the ^{3}He ion chamber is in the order of a few microseconds, the ion chamber is not adequate for the performance evaluation of the chopper system. Instead, a NaI(Tl) detector was employed. The accelerator was operated at 1.8 MeV, below the threshold of the ^{7}Li(p,n) reaction, so that only gamma-rays were produced by the ^{7}Li(p,p'γ) reaction. A block diagram of the time spectroscopy system is shown in Figure 3.7. The NaI(Tl) signal is shaped, discriminated and then fed to the MCS. As a start trigger signal of the MCS, the SYNC logic pulse from the chopper power supply is employed as stated. The SYNC pulse is generated earlier than the proton beam opening at the analyzing slit and therefore, there is a positive zero offset in the MCS. The dwell time of the MCS was set at 1 μs.

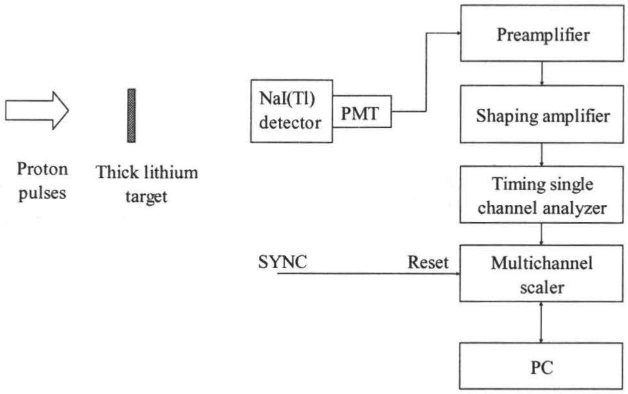

Figure 3.7: Block diagram of the proton pulsing test system. Proton pulses induce 478 keV gamma-rays, which are detected by the NaI(Tl) detector. The multichannel scaler measures the arrival time distribution with respect to the SYNC pulse.

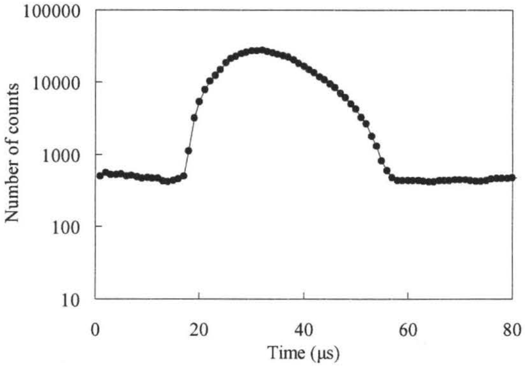

Figure 3.8: The proton pulse characteristics for the prototype switching circuit measured using proton induced gamma-rays. The pulse has a width of 20 μs and a positive skew. Time t_0=0 corresponds to the rising edge of the SYNC pulse.

The measured time spectrum is shown in Figure 3.8. From the figure, the proton pulse width is approximately 20 μs FWHM. Positive skew of the pulse shape may be attributed to a longer beam tail when sweeping the beam across the analyzing slit or changing transient chopper voltage (see Figure 3.5).

3.2.3. Modified pulsing circuit based on fast switching

Following prototype tests, a modified type of switching circuit was designed. The objective of the modification was to improve the pattern of the HV pulse shape and to reduce the proton pulse width further. To achieve this goal, the driving current of the HV power supply must be much higher than the current of the prototype to ensure faster build-up of the E-field between the plates. The current is limited by the power rating of the load resistor and switching transistors.

In this type, only one chopper plate is biased whereas the other plate is fixed at the ground potential all the time. A simplified circuit diagram is shown in Figure 3.9.

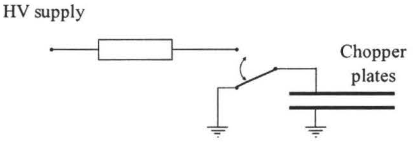

Figure 3.9: Modified HV switching circuit.

Figure 3.10 shows a measured time variation of the chopper plate potential. First, the HV switch generates the positive SYNC signal. After a few microseconds the HV decreases to 0 V, stays for a predefined time (pulse width) and then recovers to the full potential level. In contrast to the prototype, the SYNC pulse in this type is generated only at the falling edge of the HV bias. The rise and fall times of the driving potential are approx. 2 µs. For normal operations, a 300 V potential is used, which is sufficient to deflect the beam off the analyzing slit.

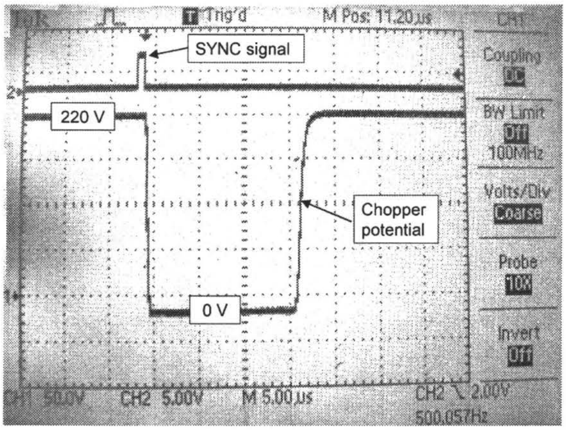

Figure 3.10: Time variation of the plate 1 potential (Ch1) and the SYNC signal (Ch2).

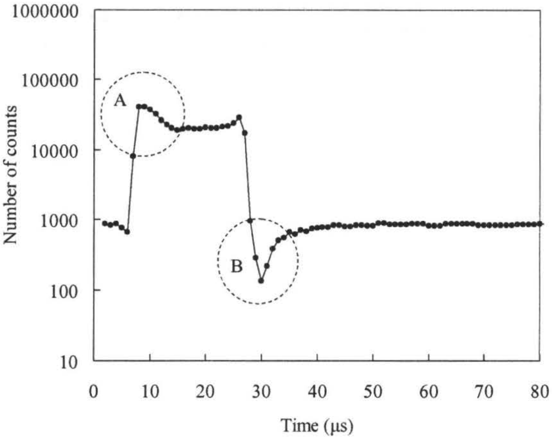

Figure 3.11: The proton pulse characteristics for the fast switching circuit. The pulse has a width of 19.5 μs. Time t_0=0 corresponds to the rising edge of the SYNC pulse.

The switching circuit was tested in the same way as the prototype. As shown in Figure 3.11, this type of switching gives a more rectangular pulse profile. However, the areas marked with circles in Figure 3.11 show significant deviation from the expected profile. Rather than the beam intensity change, these irregularities may be related to the pulse processing and collection statistics. In the area A, the increase in number of counts may be explained by the fact that the pulse processing system is less likely to show dead time in the very beginning of the high event rate pulse, therefore initial pulses are more likely to be processed. Similarly, in the area marked as B, the pulse processing system extends the dead time which makes background events following the high intensity pulse be less likely to be processed.

3.2.4. Experimental setup for measurements with the ^{3}He chamber

Figure 3.12 shows a block diagram for neutron field measurements. The ^{3}He ion chamber output signal was split and connected to the MCS as well as a commercial digital signal processing (DSP) unit (ORTEC DSPEC Plus). Detailed information on operating parameters is available in the previous chapter. The DSP unit can be operated in coincidence or anticoincidence mode.

A branch of the SYNC pulse is connected to a gate and delay (not shown in Figure 3.12), which generates the coincidence gate signal. The time t_g, during which the coincidence gate remains open determines the neutron energy discrimination level. As shown in Figure 3.8 and Figure 3.11, there is a time gap (t_d) between the SYNC pulse and gamma-ray events occurring in the NaI detector. This is related to the time required for protons to travel from their resting position to the analyzing slit as well as a finite time required for the HV switch transistors to change their logic states. In order to compensate for this time, the coincidence signal was delayed by 17 μs for the prototype of the HV switch. A similar delay was given to the modified HV switch.

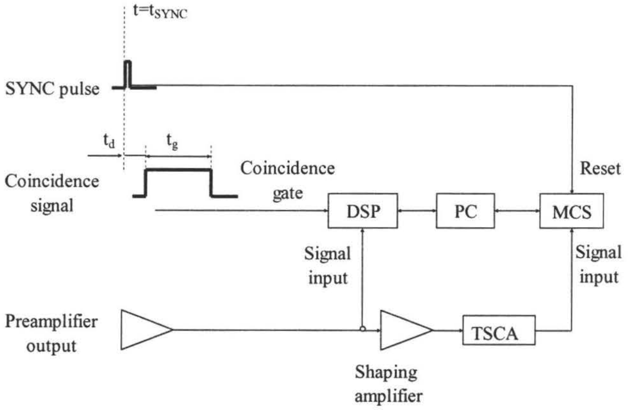

Figure 3.12: Diagram of the pulse processing system. The SYNC signal resets internal clock of the MCS system. The coincidence signal width determines minimum neutron energy acquired by the DSP in coincidence mode.

3.3. Results

3.3.1. Neutron energy spectra in coincidence and anticoincidence modes

In order to evaluate performance of the electrostatic chopper system, three measurements were taken at the 2.2 MeV proton energy with different DSP coincidence gate settings. The proton pulse width was set at 20 μs. First (Figure 3.13 (a)), the DSP was set into the coincidence mode, with the window width of 20 μs. Figure 3.13 (b) shows the spectrum taken with a much longer, 160 μs coincidence window. As expected, the 20 μs coincidence gating gives more effective slow neutron rejection than 160 μs gating. The ratio of the counts above epithermal peak (> 794 keV) to the epithermal peak counts (764 ± 30 keV) is 0.2 and 0.04, respectively. Next, the DSP was set into the anticoincidence mode by keeping the coincidence width unchanged and the corresponding spectrum in Figure 3.13 (c) shows almost pure slow neutron response of the detector. For comparison, a typical 2.2 MeV spectrum acquired with continuous proton mode is shown in Figure 3.13 (d).

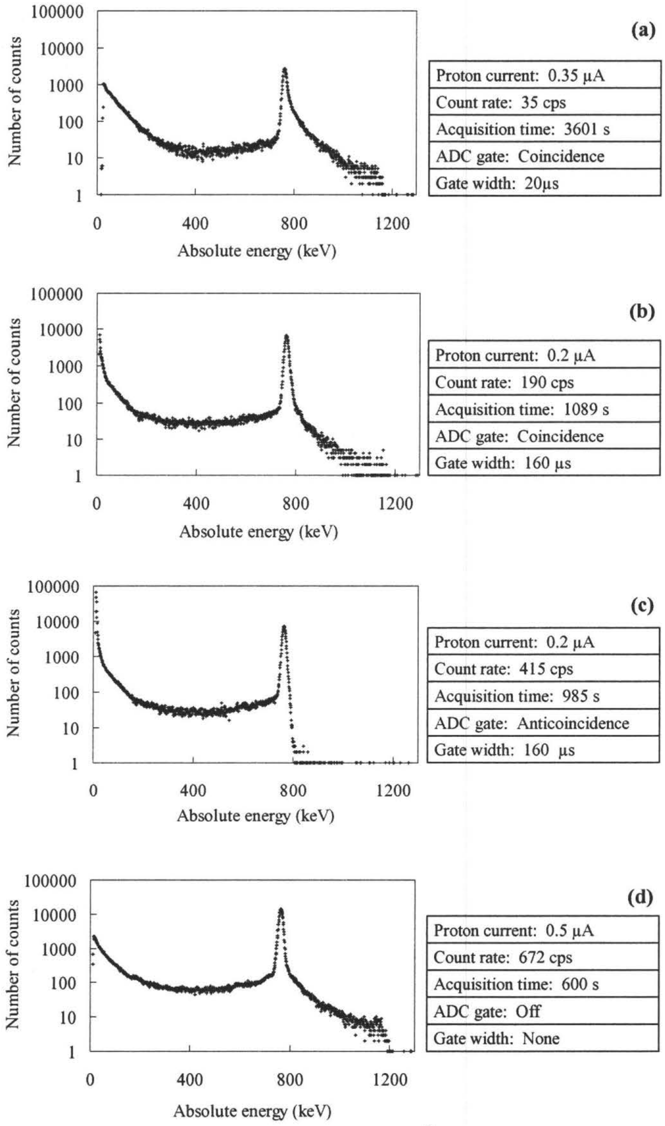

(a)
Proton current: 0.35 μA
Count rate: 35 cps
Acquisition time: 3601 s
ADC gate: Coincidence
Gate width: 20μs

(b)
Proton current: 0.2 μA
Count rate: 190 cps
Acquisition time: 1089 s
ADC gate: Coincidence
Gate width: 160 μs

(c)
Proton current: 0.2 μA
Count rate: 415 cps
Acquisition time: 985 s
ADC gate: Anticoincidence
Gate width: 160 μs

(d)
Proton current: 0.5 μA
Count rate: 672 cps
Acquisition time: 600 s
ADC gate: Off
Gate width: None

Figure 3.13: Neutron spectra measured by the ^{3}He spectrometer for incident proton energy 2.2 MeV, (a) Coincidence mode with a short gate width (b) Coincidence mode with longer gate width (c) Anticoincidence mode (d) Reference spectrum acquired with continuous proton beam.

3.3.2. Neutron time spectrum

The MCS spectrum in Figure 3.14 shows a time distribution of neutron detection events with respect to the SYNC signal. In order to count only neutron events, the LLD of the TSCA was set right below the epithermal peak pulse height. The dwell time of the MCS was set at 10 μs.

From the figure, the peak intensity at ~0.1 ms after the SYNC pulse corresponds to the neutron energy of approx. 10 eV. As presented in the previous chapter, neutrons of energies in this range are the main source of the epithermal peak.

Since 160 μs and 20 μs coincidence windows were used to collect data with the DSP, the MCS spectrum was used for estimating the fraction of all counts processed. From the figure, for the 160 μs coincidence window width, 78 % of all detected events are processed. The estimated fraction of processed events for the 20 μs coincidence window is in the order of a few percent. By reducing the coincidence window from 160 to 20 μs, the epithermal peak should be reduced by a factor of ~ 20, which is quite different from the epithermal peak reduction identified in Figure 3.13. Misalignment of the proton pulse with the coincidence window may be partly responsible for the difference. Further investigations will be carried out to address this problem.

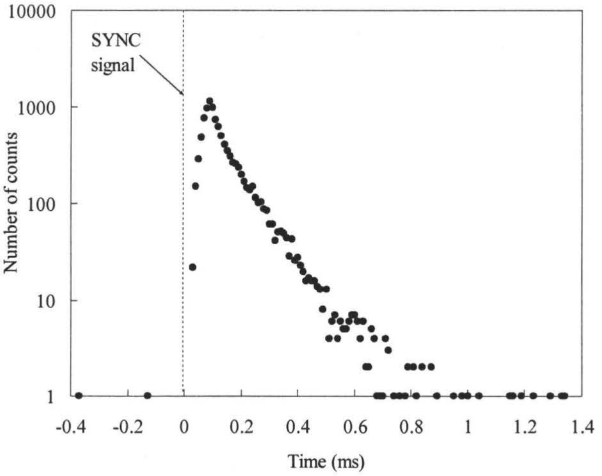

Figure 3.14: Time spectrum of the ^{3}He ion chamber.

Chapter 4

OPTIMIZATION OF THE PROTON CHOPPER FOR ^{7}Li(p,n) NEUTRON SPECTROMETRY USING A ^{3}He IONIZATION CHAMBER

4.1. Summary

Following the design and first tests of the proton chopper system, thick target ^{7}Li(p,n) neutron spectra measurements with the ^{3}He ion chamber in the proton energy region between 1.9 and 2.3 MeV using the McMaster pulsed accelerator neutron source are presented in this chapter. The pulsed neutron beam was produced by the electrostatic proton chopper described in chapter 3 to reject the slow neutron detection events, which seriously limit the fast neutron counting rate of the ^{3}He ion chamber. The chopper system was fully characterized using a NaI(Tl) detector in a wide range of proton pulse widths. To collect both arrival time and energy information of NaI(Tl) detection events, a time-energy analyzer was built using a time scaler and a successive approximation peak sensing ADC. The measured time distributions of the 478 keV gamma-ray peak from the 7Li(p,p'γ) reaction showed a reasonable agreement with the chopper controller settings. To optimize the proton chopper operation for the ^{3}He ion chamber, neutron spectra were collected in coincidence with the proton pulse for various proton pulse widths. At each proton energy, optimum chopper operation was determined by taking into account the two competing requirements: high fast-to-slow neutron ratio and realistic fast neutron counting rate. The proton pulse and coincidence window widths used were between 20 μs for 1.95 MeV and 5 μs for 2.3 MeV, which corresponded to calculated time-of-flight rejection thresholds of 180 eV and 2.8 keV respectively. The raw data collected at optimum conditions were analyzed using three different spectral unfolding methods: a simple division by detection efficiency, an iterative algorithm, and a regularized constrained

inversion method. The three methods gave consistent neutron fluence spectra within 20% above 30 keV. Thanks to the enhanced fast-to-slow neutron ratio of the pulsed beam, the full detector response function could be employed in unfolding, which led to an extension of the dynamic energy range as well as a better stability of the unfolding process in the low energy region.[*]

The content of this chapter has been submitted for publication in Nuclear Instruments and Methods Section A. The manuscript was prepared by me and revised by co-authors. The introduction and conclusion sections of the paper were removed to avoid redundancy with the information contained in the introduction and conclusion chapters of this thesis. The reference system was adjusted to conform to the referencing style used in the thesis. The bibliography is presented at the end of the thesis.

---

[*] Based on the abstract from: Optimization of the proton chopper for ^{7}Li(p,n) neutron spectrometry using a ^{3}He ionization chamber, submitted for publication in Nucl. Instr. Meth. A, March 10, 2010.

Optimization of the proton chopper for ^{7}Li(p,n) neutron spectrometry using a ^{3}He ionization chamber

W. Matysiak[1], D.R. Chettle[1], W.V. Prestwich[1], S.H. Byun[1]

[1]Medical Physics and Applied Radiation Sciences, McMaster University,
Hamilton, ON, Canada, L8S 4K1

Submitted for publication in *Nuclear Instruments and Methods in Physics Research Section A: Accelerators, Spectrometers, Detectors and Associated Equipment*, 10 March 2010.

4.2. The proton chopper

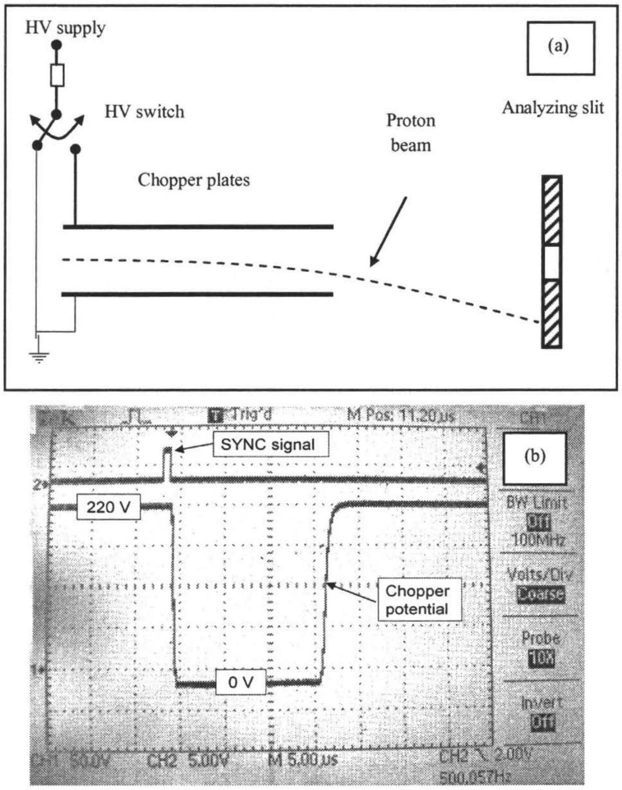

Figure 4.1: (a) Diagram of the electrostatic chopper system and (b) experimentally measured output potential of the top chopper plate.

[…] The design of the proton chopper has been described in detail in the previous chapter. As shown in Figure 4.1, the chopper relies on electrostatic deflection of the proton beam. Two aluminum plates (a) were inserted in the last section of the proton beam line. The bottom plate is permanently grounded and the top plate is connected to a high voltage switch, which periodically drives the plate potential from zero to 300 V. The maximum voltage is sufficient to create the E-field needed to deflect the proton beam from the opening of the analyzing slit. At the beginning of each duty cycle, the HV switch generates the logic SYNC signal (b), which is subsequently used to trigger the peak-sensing ADC coincidence window and the multichannel time scaler.

4.3. Tests and results

4.3.1. Diagnostics of the proton chopper

For timing investigations of the pulsing system, the accelerator was operated at 1.8 MeV, which is below the neutron production threshold. The time distribution of the 478 keV gamma-rays from the ^{7}Li(p,p'γ) reaction was measured to diagnose the proton pulsing system. A NaI(Tl) detector coupled to a photomultiplier tube was used as a gamma-ray detector because scintillation pulses produced by the detector are fast and need only a short shaping time, therefore introducing little time delay between an actual detection event and its counting by the pulse processing chain. To collect both energy and time information simultaneously, a 2-D time-energy analyzing system was built. The NaI detector output signal was shaped by a shaping amplifier with 0.25 μs shaping time and connected to the 2-D system as shown in Figure 4.2.

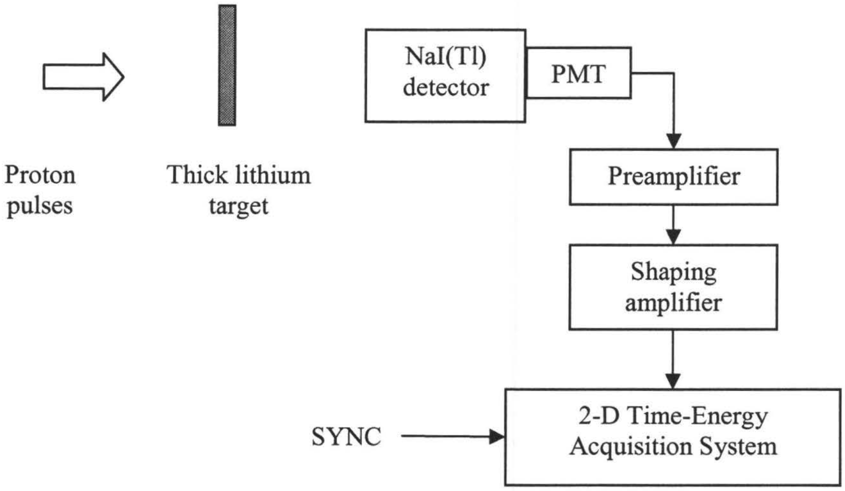

Figure 4.2: Block diagram of the proton pulsing test system. The 478 keV gamma-rays from the ^{7}Li(p,p'γ) reaction were detected by the NaI(Tl) detector. The 2-D time-energy acquisition system analyzes the pulse height and its arrival time with respect to the SYNC signal.

Figure 4.3 shows the detailed block diagram of the 2-D system. The input of the 2-D system accepts a shaped linear signal. The peak-sensing ADC (model

8715, Canberra) carries out the pulse height analysis and indicates the end of conversion time by the DATA READY logic signal. Since the ADC is a successive approximation type and the conversion time is constant, the DATA READY signal can be used as a simple way of picking up the detected pulse arrival time. The time scaler is triggered by the SYNC signal sent by the proton chopper and records the pulse arrival time. The dwell time of the time scaler was set at 1 μs, which is a sufficient time resolution for proton chopper evaluation. Both pulse height and arrival time values are read directly by a digital signal processing (DSP) unit (model DSP56F807PY80, Freescale Semiconductor) and recorded in its 64 kB memory which is allocated to form a matrix of 64 columns by 1024 rows to store pulse arrival time and amplitude, respectively. This matrix can be requested anytime during the acquisition or after the acquisition is completed and transferred via USB connection to the PC.

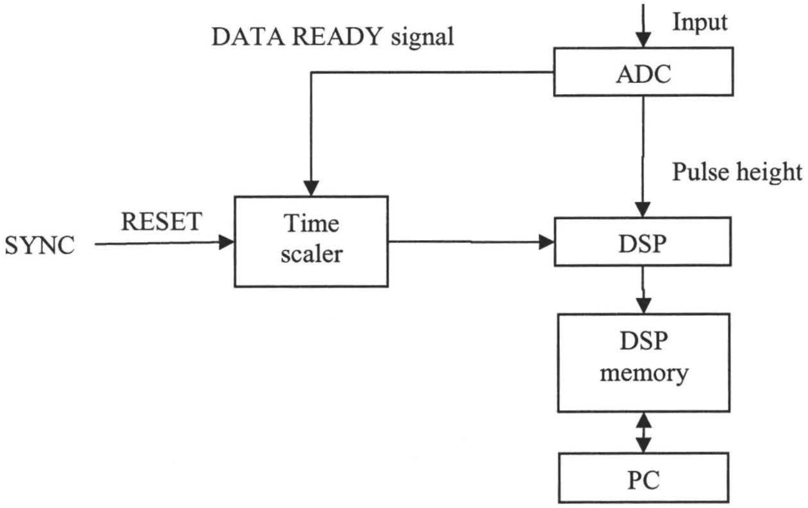

Figure 4.3: 2-D time-energy acquisition system.

Since the 2-D system picks up the leading edge time of the ADC DATA READY signal rather than a constant fraction time of the preamp rising edge, the recorded time is delayed by both the shaping amp and the ADC. In particular, the peaking time of the shaping amp is subject to the shaping time constant, so that the amount of time delay changes when the shaping time setting is altered. This delay effect is demonstrated in Figure 4.4 for a CR-(RC)^2 shaper, the peaking of which is given by twice the shaping time. As shown in the figure, a longer shaping time leads to a longer delay time. Given that the two delay effects by the shaping amp and the ADC can be calibrated, the effects do not induce any significant problems.

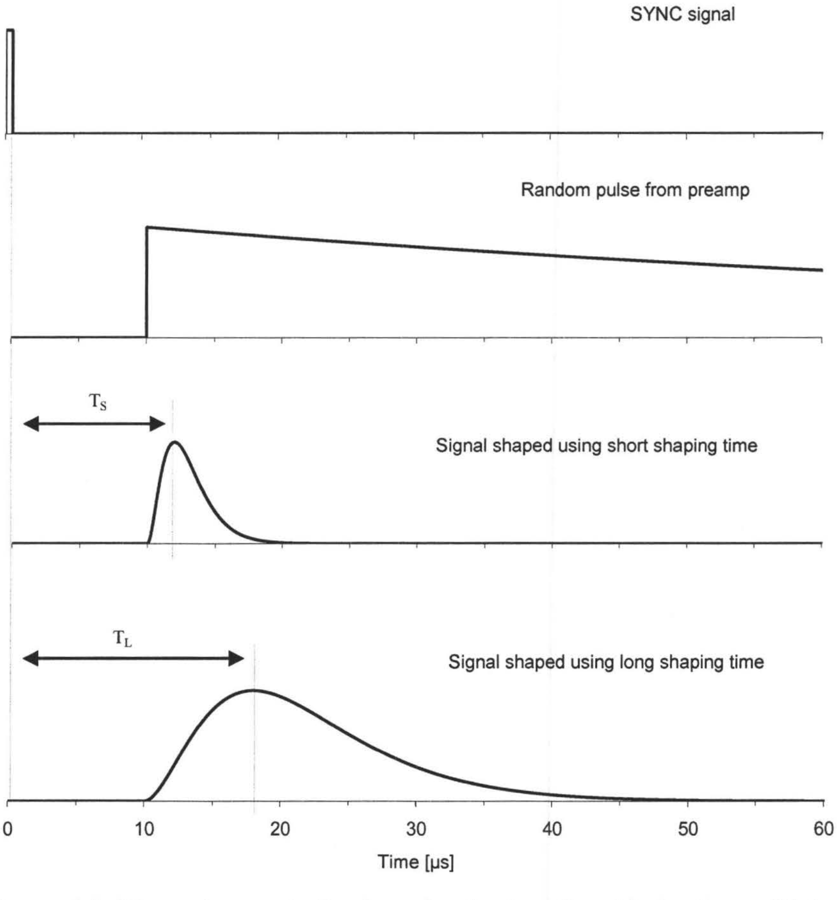

Figure 4.4: The assignment of a shaped pulse to a time bin by the multichannel time scaler depends on the shaping time. The time interval T_S (pulse shaped using a short shaping time) is shorter than T_L (pulse shaped using a long shaping time).

To evaluate the performance of the chopper, the chopper system should be characterized comprehensively. The proton chopper allows for setting the proton pulse width in 1 microsecond intervals. A series of measurements was conducted by varying the proton pulse width from 1 to 40 microseconds. The instantaneous proton current incident on the lithium target was kept between 4 and 6 microamperes, which led to approximately 0.1 counts per 1 microsecond time channel per duty cycle. The time spectra presented in Figure 4.5 were obtained by integration of the 2-D spectrum along the energy axis around the 478 keV peak. The vertical axis shows the gross integrated number of counts of the 478 keV peak region in 1 μs intervals (dwell time of the 2-D system) and the horizontal axis indicates time after the SYNC signal. The results show the setting of the proton chopper and the experimentally measured FWHM of each gamma-ray burst. It is apparent, that the proton chopper setting is consistently lower than the experimentally found FWHM of the gamma-ray burst.

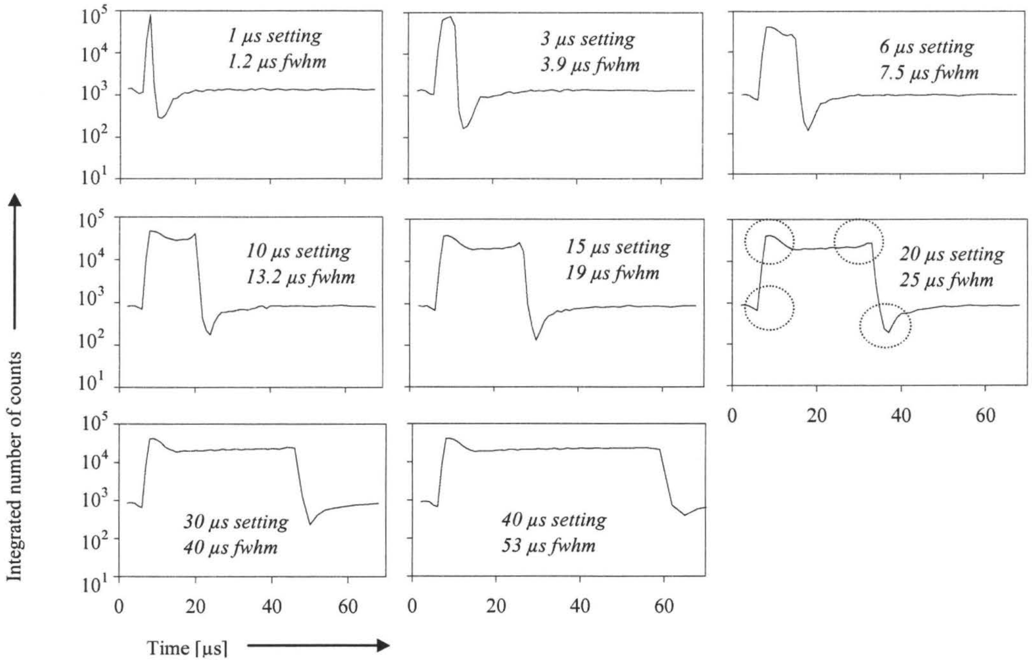

Figure 4.5: Multichannel time spectra of the proton pulse for proton pulse width settings from 1 to 40 microseconds. Time T=0 corresponds to the leading edge of the SYNC pulse. The vertical axis represents integrated number of counts around the 478 keV peak and the horizontal axis the time after the SYNC signal.

All spectra in Figure 4.5 show a background continuum of the 478 keV gamma-rays which do not originate from the ^{7}Li(p,p'γ) reaction but from the decay of ^{7}Be present in the target (See section 6.1.2).

It is also visible that all spectra exhibit characteristic "dips" and "horns" (areas marked with circles in Figure 4.5). At the leading edge of the proton pulse, a decrease in the number of recorded pulses even below the background level of ^{7}Be decay gamma-rays is visible in the time region immediately before the proton beam hits the target. This is followed by an increased number of recorded events immediately after the proton beam starts striking the target. On the other hand, a reversed pattern can be observed at the falling edge of the proton pulse: an increase in the number of counts before the end of the pulse and a decrease below the normal background level after the beam is deflected from the target.

The decrease in number of counts below the background level indicates a trend occurring in the detector-pulse processing chain rather than a physical phenomenon. In order to explain this, the experiment was repeated with the NaI detector located further away from the target to investigate if the count rate is responsible for these artifacts.

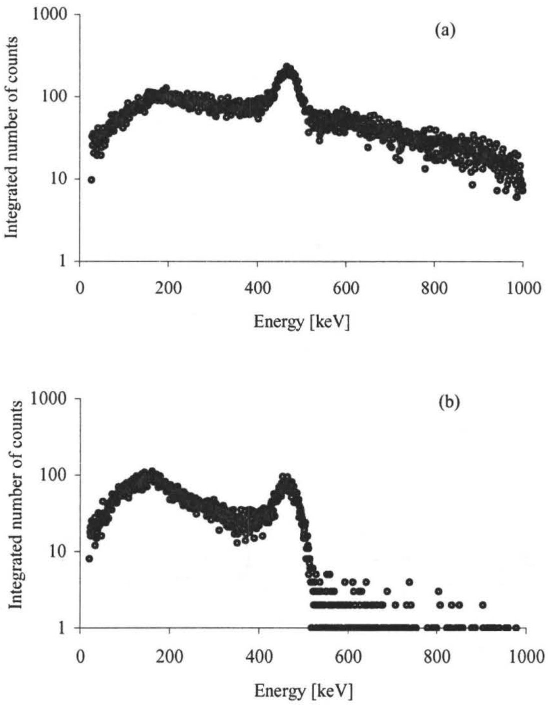

Figure 4.6: Pulse height spectrum of events occurring between 9th and 10th microsecond after the SYNC signal for the proton pulse width setting of 20 μs. The detector located at (a) 37 cm and (b) 1.2 m from the lithium target.

Figure 4.6 shows pulse height spectra for a single time channel of the 2-D acquisition system taken at two distances between the detector and the lithium target. Figure 4.6 (a) shows significant amount of coincidence summing events as opposed to Figure 4.6 (b), where there are very few events above the full energy peak. What follows is, that in the first case some pulses were not scored around the 478 keV peak but their amplitudes piled-up with other events and the summed amplitudes were assigned to other regions of the spectrum. This observation can help explain the aforementioned spurious "dips" and "horns" in the spectrum. Namely, the "dips" originate from the fact that the background pulses immediately before the high count rate region are likely to pile up with events in that high count rate region, therefore are more likely to miss the full energy peak. Similarly, but in reversed order: the background events following the high count rate region can incidentally ride on the tail of pulses from the high counting rate region making them more susceptible for random summing than the later background events. The "horns" on the other hand, are the regions of the high counting rate whose origin can be explained in the following manner: pulses on the extreme ends of the high counting rate region are less likely to pile up than the pulses in the middle of that region.

4.3.2. ^{3}He ion chamber timing behavior

Following the proton pulsing system tests using the NaI(Tl) detector, the next experiment was conducted with the ^{3}He ion chamber. Figure 4.7 shows the block diagram of the ^{3}He ion chamber pulse processing. To compare the timing performances between ^{3}He ion chamber and NaI(Tl), the proton energy was set at 1.8 MeV and both detectors were sequentially exposed to the ^{7}Li(p,p'γ) gamma-rays and their data were collected using the 2-D system. The shaping time of the system remained at 0.25 microseconds for both detectors. In addition, a digital pulse processing chain was added to the ^{3}He preamplifier output signal in order to compare timing behaviors between the analog and the digital systems. The complete block diagram of the pulse processing system is shown in Figure 4.7. Using a Gate & Delay triggered by the SYNC pulse, the digital pulse processing (DPP) unit (model DSPec, ORTEC) was operated in coincidence mode. The coincidence gate window was set at 2 μs and the delay was varied in 2 μs steps from 10 to 50 μs. Then in principle, the collected data are equivalent to a multichannel time spectrum with a dwell time of 2 μs. The 0 to 100 % rise time (i.e. peaking time) and the flattop of the DPP were set at 0.8 μs and 0.4 μs, respectively, which are close to the analog CR-(RC)^2 shaping with a 0.25 μs shaping time.

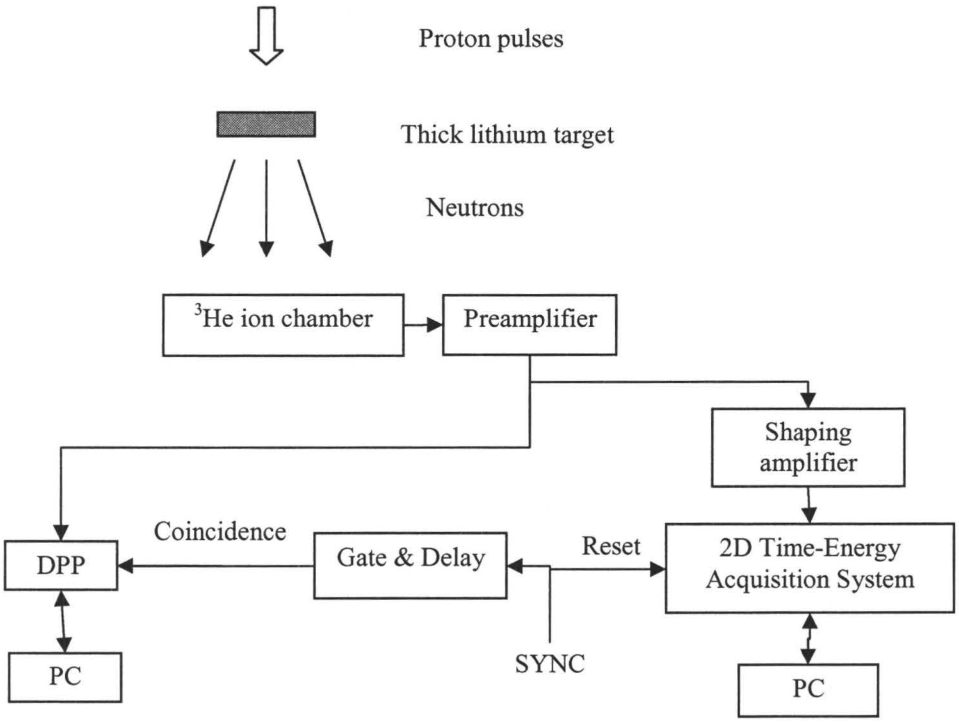

Figure 4.7: Diagram of the ^{3}He ion chamber pulse processing system. The SYNC signal is generated by the proton chopper at the beginning of each proton pulse. The Gate and Delay produces the coincidence window for the DPP.

Figure 4.8 shows multichannel gamma-ray time spectra collected by (a) NaI detector and (b) ^{3}He ion chamber, respectively. Comparison between (a) and (b) reveals that the timing difference for the 0.25 μs shaping time is very small but observable. Also in Figure 4.8 (b), the differences in timing between the digital system and the analog system can be noted. The 50 % fraction of the maximum counting rate is located at 7 μs after the SYNC pulse for all three conditions. The FWHM measured with the NaI detector is 26 μs, the ^{3}He detector with the DPP shows 20 μs and the analog system indicates 23 μs. The differences between the DPP and the analog system working with the ^{3}He detector (Figure 4.8 (b)) determine the extent to which the two spectra can be compared in latter measurements.

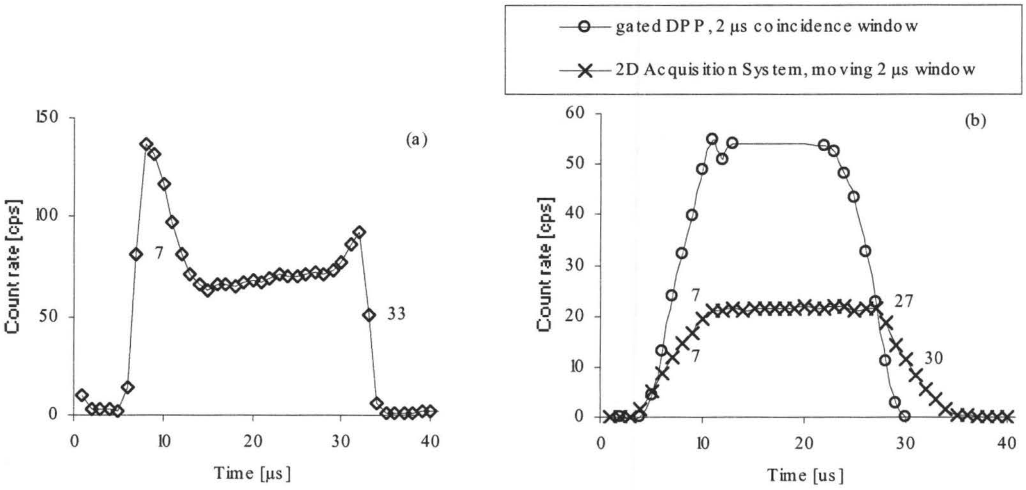

Figure 4.8: Multichannel gamma-ray time spectra of the pulsing system with short shaping time (0.25 µs) taken with (a) NaI detector and (b) ^{3}He ion chamber – analog 2-D acquisition system (open circles) and a series of DPP measurements in coincidence mode (crosses). Time T=0 indicates the leading edge of the SYNC pulse.

Ultimately, the ^{3}He ion chamber needs a longer shaping time for better energy resolution (Matysiak et al., 2008) in neutron measurements. Therefore in the next experiment, a similar experiment was performed with the DPP set at 8 µs rise time and 2 µs flattop, which are the optimized digital pulse shaping parameters for neutron spectroscopy. The proton energy was left at 1.8 MeV without change. The equivalent shaping time in the analog system was set at 4 µs. Figure 4.9 shows the comparison of timing behavior of the two processing chains with these shaping parameters.

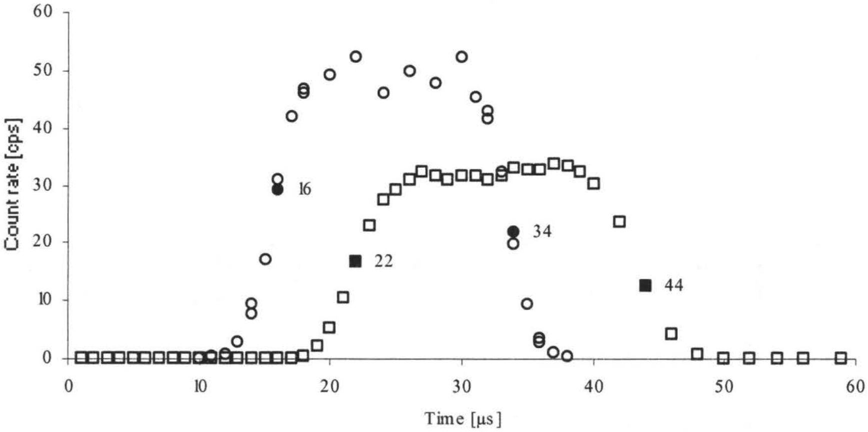

Figure 4.9: Multichannel gamma-ray time spectra of the ^{3}He ion chamber taken with the analog 2-D acquisition system at 4 µs shaping time (squares) and a series of DPP at 8 µs rise time in coincidence mode (circles).

As presented in Figure 4.9, the FWHM widths are 18 µs and 22 µs for the digital and analog systems, respectively. There is also a 6 µs time offset between the two pulses. The offset may be a result of different time pickup methods used by the two systems. The difference in observed count rates is due to different LLD settings for both systems.

^{3}He ion chamber interactions with gamma-rays produce pulses of relatively low amplitudes. However, the pulses created by neutron interactions have at least approximately three times higher amplitudes. It is important therefore to ascertain, that the time pickup for a detected pulse does not depend on its amplitude. Indeed, an experiment performed with a precision pulser connected to the test input of the ^{3}He detector preamplifier showed, that for neither the analog nor the digital systems, the position of the time channel of the pulse varies with amplitude. Knowing this fact, the timing behavior of the pulsing system with the signal processing chain will not change for neutron interaction events. Starting position and width of the proton pulse analyzed from the digital system data were recorded and used in the subsequent neutron fluence spectra measurements for generating the coincidence gate signal.

4.3.3. ^{3}He neutron spectra for pulsed and continuous proton currents

In the neutron TOF measurements the energy of neutrons arriving at the detector is directly coupled to the time after the neutron pulse. This observation is important for the ^{3}He ion chamber due to the fact that the intrinsic efficiency of the detector for eV neutrons becomes high (Figure 2.5). It is expected therefore, that the instantaneous counting rate of the system increases with time after the proton pulse. If the instantaneous current is high and the proton pulse and the coincidence window are sufficiently wide, the detector can exhibit significant dead time during the proton pulse.

In this experiment, the linearity of the variation of the total number of counts in the detector with the proton current at fixed proton pulse and coincidence window widths was investigated. Considering the duty cycle efficiency (2 ms repetition interval and 20 μs proton pulse width), the effective current of 0.6 μA (Figure 4.10) corresponds to the instantaneous current of 60 μA, and is the maximum available current with the McMaster KN accelerator. Also, 2.3 MeV is the highest proton energy investigated in this study. The two combined factors (maximum proton energy and current) determine the highest neutron production rate achievable with the KN accelerator.

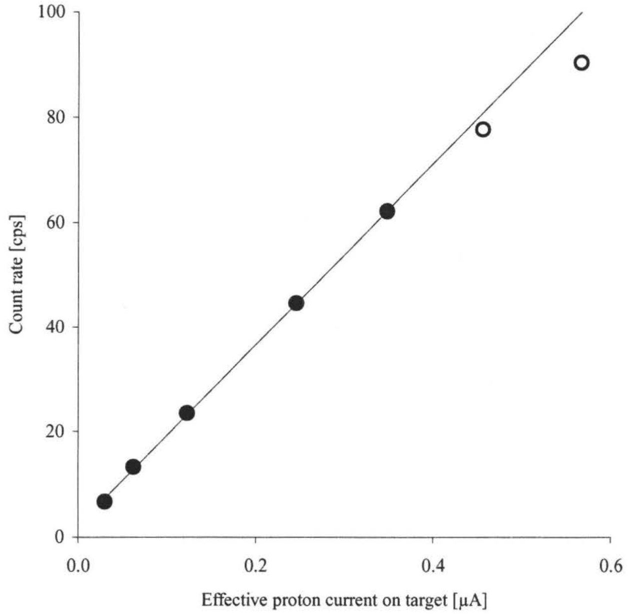

Figure 4.10: Count rate of ^{3}He neutron events (above 300 keV deposited energy) vs. effective proton current for fixed proton pulse and coincidence window widths at incident proton energy of 2.3 MeV.

Figure 4.10 shows the counting rate of the ^{3}He neutron events above a deposited energy of 300 keV, which is the upper value of gamma-ray response of the detector, chosen with a sufficient margin to ensure only neutron events are counted. The figure shows that over the operating range up to approximately 0.4 µA and for 20 µs proton pulse width setting and 20 µs coincidence window width, the count rate increases linearly with the effective current. Above 0.4 µA the observed count rate starts deviating from linearity, and at the maximum current value of 0.6 µA, the observed count rate is 10 % lower than the linear trend.

To ensure that spectra collected in the pulsed mode are equivalent to spectra collected in continuous mode, not only in the relative scale but also in absolute neutron yield, two spectra in the pulsed and the continuous modes were collected sequentially, normalized to the total proton charge, and compared. Figure 4.11 shows the two spectra collected at 2.1 MeV. The instantaneous proton current of the pulsed mode was set at 60 µA, which leads to an effective current of

0.6 μA. The continuous mode data were collected at ~ 0.6 μA and then finely normalized using the total proton charge. As shown in the figure, the patterns of the two spectra in the fast neutron region are consistent. To attempt a quantitative comparison between the two modes, the fast neutron counts above the deposited energy of 794 keV (i.e. 30 keV neutron energy) were integrated for each spectrum. The number of fast neutron counts for the continuous current mode (18.1 counts/μC) was slightly higher than the number of fast counts for the pulsed mode (15.0 counts/μC). This discrepancy can be explained by the fact that for the 20 μs proton pulse width and coincidence window settings, the wider true proton pulse width of 25 μs (see Figure 4.5) leads to a 20% loss in the fast neutron counting rate. As expected, the epithermal neutron peak and the recoil continuum are much higher for the continuous mode spectrum. Also, in the pulsed beam spectrum, the gamma-ray response of the detector can be clearly seen to extend up to approximately 300 keV. In the case of continuous current spectrum, this part is visible only up to approximately 200 keV with the remainder buried under the continuum.

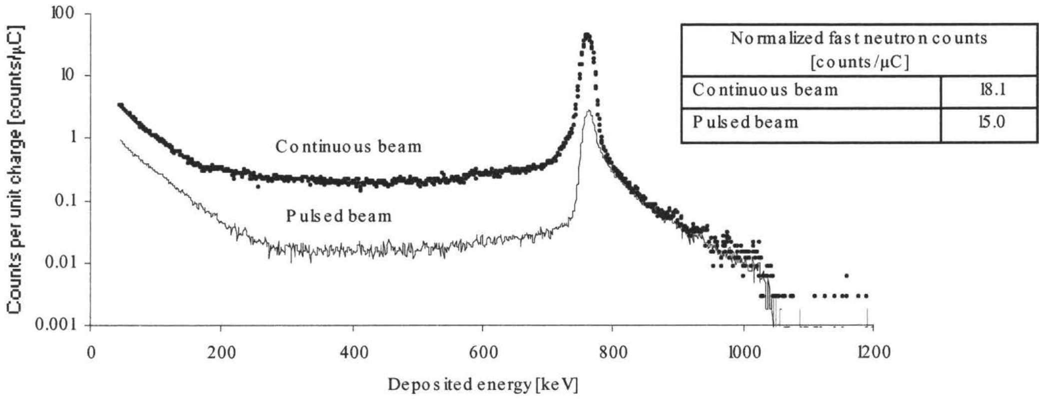

Figure 4.11: Raw neutron spectra normalized to proton charge collected at 2.1 MeV proton energy. Pulsed beam acquisition parameters: 60 μA instantaneous current incident on the analyzing slit, 2 ms duty cycle, 20 μs proton pulse width setting, and 20 μs coincidence window width. Continuous current acquisition: 0.58 μA proton current. The fast neutron counts refer to the integrated number of events above the deposited energy of 794 keV (i.e. 30 keV neutron energy) per proton charge.

4.3.4. Optimization of the proton pulse width for fast neutron spectra collection

Since the ultimate goal of the spectrum collection in the pulsed mode is the rejection of slow neutrons, it is critical to optimize the proton chopper operation. The rejection threshold of 180 eV determined in the previous chapter was governed mostly by the proton pulse width and the corresponding coincidence window width. However, reducing the width of both proton pulse and coincidence window leads to proportional reduction in fast neutron counting rates. Since the neutron yield changes by a factor of 10 in the proton energy range investigated in this study (between 1.95 MeV and 2.3 MeV), the optimal condition of the proton chopper operation may significantly vary depending on the proton energy. Figure 4.12 shows comparison of ^{3}He neutron spectra taken at 2.3 MeV with different proton pulse and coincidence window widths at the maximum available instantaneous proton current (60 μA). From the figure, it is clear that the total count rate increases with increasing proton pulse and coincidence window widths. However, the fraction of events scored in the epithermal peak region (764 ± 30 keV) also increases (Table 4.1) which may also be visible when comparing epithermal peak shapes for the three conditions. As the proton pulse gets shorter, the epithermal peak becomes less pronounced.

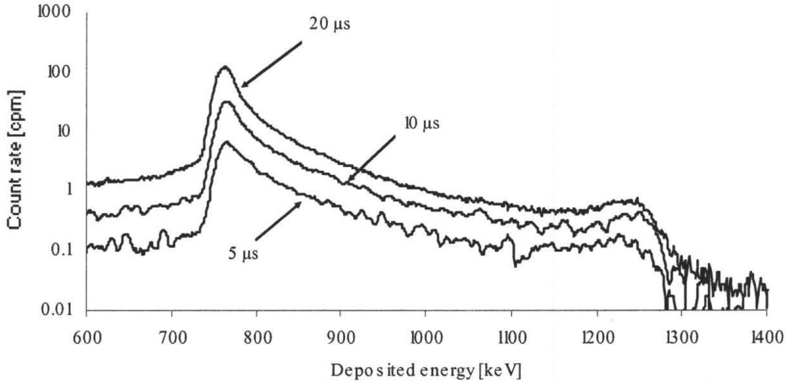

Figure 4.12: Raw neutron spectra taken at 2.3 MeV and maximum instantaneous proton current (60 μA) by varying proton pulse and coincidence window width: 5, 10, and 20 μs.

Table 4.1: Acquisition parameters for 5, 10, and 20 μs nominal proton pulse and coincidence window widths at 2.3 MeV and maximum available proton current incident on the proton chopper analyzing slit (60 μA).

Proton pulse width setting and coincidence window width	5 μs	10 μs	20 μs
Fast neutron (>794 keV) count rate	3.2 cps	9.3 cps	20.2 cps
Ratio of events scored around the epithermal peak (764 ±30 keV) to fast events (>794 keV)	1.1	1.7	2.8
Estimated slow neutron TOF rejection threshold	2.8 keV	714 eV	180 eV

Selection of optimal acquisition parameters at various proton energies was based on the balance between the fast neutron counting rate and slow neutron rejection threshold as well as to avoid lengthy collection times. As the neutron yield significantly depends on the proton energy, optimal acquisition parameters were established individually for each proton energy. For 2.3 MeV the selected proton pulse width and coincidence width were set at 5 μs whereas 10 μs was used for both 2.1 and 1.95 MeV.

It is important to note, that at such low counting rates, any contribution of other neutron producing reactions from the proton beam striking accelerator beam line components (and therefore perturbing the measured spectra) must be established. If this perturbation is high, it will be a limiting factor for shortening the proton pulse and coincidence window widths. Identified reactions which may contribute to neutron yield (F. C. Young, 1996) are ^{65}Cu(p,n) and ^{12}C(d,n). The former reaction is due to the proton beam hitting the analyzing slit made of brass and the latter is due to natural abundance of deuterium in the beam and carbon deposits on the analyzing magnet and the upstream components due to the oil diffusion vacuum pump.

In order to determine the total contribution of the perturbing reactions quantitatively, the proton beam was parked at its resting position striking the slit material only by applying a constant potential difference of 300 V between the deflection plates. This way, the lithium target was not contributing to neutron production and only the perturbing reactions were investigated. Table 4.2 shows fast neutron count rates observed in the ^{3}He spectrometer at the maximum proton current. The counting rates from the perturbing reactions are quite small in the continuous proton mode, and have to be further multiplied by the duty cycle efficiency (1 per cent or less) in order to compare them with the fast neutron counting rate from the ^{7}Li(p,n) reaction. Consequently, it was concluded, that the contaminating neutron producing reactions do not distort the collected data.

Table 4.2: Fast neutron counting rates measured in the continuous mode from the perturbing neutron productions on various elements of the accelerator beam line.

Proton energy	2.2 MeV	2.3 MeV
Fast neutron (>794 keV) count rate	11 counts/600 s	8 counts/600 s

Figure 4.13 shows raw neutron spectra taken with the ^{3}He spectrometer in the pulsed mode for three proton energies: 1.95, 2.1, and 2.3 MeV. Theoretical analysis of the ^{7}Li(p,n) reaction shows that for 2.3 MeV proton energy, the maximum neutron energy extends above 500 keV. This phenomenon is visible as the hydrogen recoil continuum between approximately 300 and 500 keV energy deposited in the detector. The above three spectra also show that the gamma-ray response becomes insignificant above approximately 300 keV. Since the gamma-ray response of the detector varies with experimental conditions, it has not been included in the response function, therefore only the part of the spectrum above 300 keV was used in the spectral unfolding process.

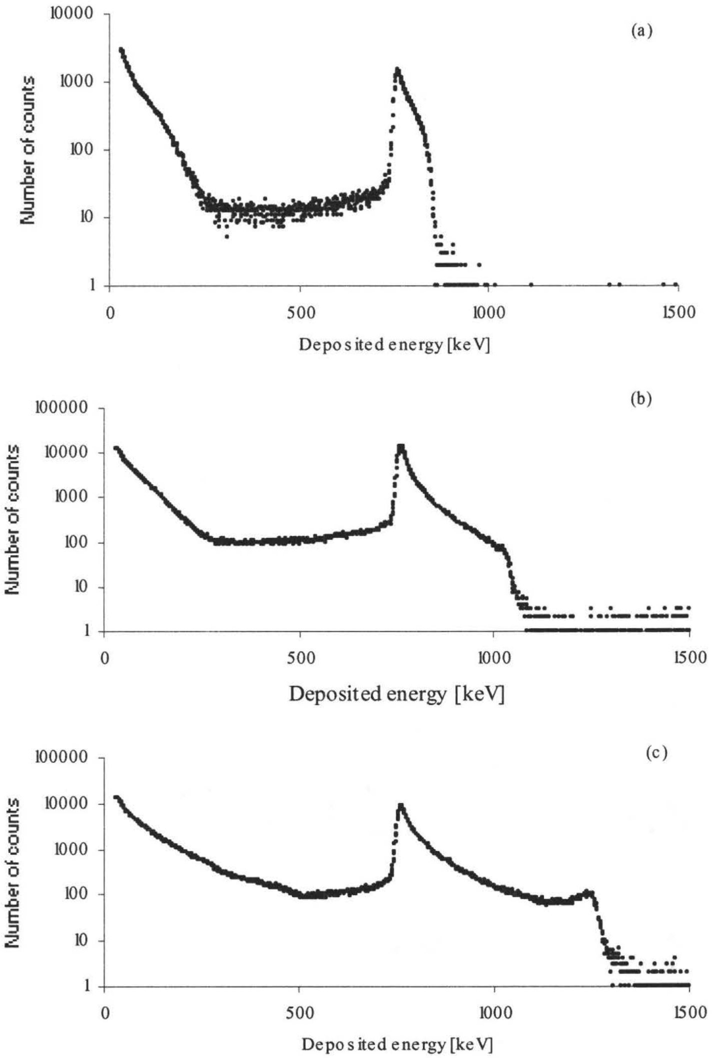

Figure 4.13: Raw neutron spectra collected in the pulsed mode for three proton energies (a) 1.95 MeV, (b) 2.1 MeV, (c) 2.3 MeV.

4.3.5. Neutron spectra acquisition and unfolding

The response function matrix used in the unfolding process was based on the experimental data published by Beimer et al. (Beimer et al., 1986). Since their data cover the neutron energy region from 130 to 3024 keV, it was necessary to extend it to epithermal energies. First, the response of the detector to the epithermal neutrons was experimentally acquired. This was done by making use of the proton pulsing system and running the acquisition system in the anticoincidence mode. Next, the fitting parameter set provided by Beimer was used to fit the experimentally acquired response of the detector to epithermal neutrons, and the parameter values were linearly interpolated between 0 and 130 keV. Since the tabulated fitting parameters describing the full energy peak width have significant uncertainties (10 % or more) and do not show any consistent trend with neutron energy, it was concluded that both incomplete charge collection and electronic noise dominate the experimentally established peak width, therefore linear interpolation of the peak parameters was justified.

Finally, the peak efficiency of the detector was also extended to the epithermal energy using the 1/v dependence of the ^{3}He(n,p) cross-section and the response function was normalized to the peak efficiency. Chapter 2 presents the Monte Carlo (MC) approach to validate the peak efficiency of the detector taking into account the wall effect. The results show that the MC simulated efficiency overestimates the experimental values by approximately a factor of two. Since the reported experimental detector efficiency function shows different values depending on the shaping parameter of the pulse processing (Beimer et al., 1986), it was concluded that this discrepancy was due to the incomplete charge collection process.

There is no simple method to verify the response function experimentally in the region where it was interpolated (0 to 130 keV), however without doing so it is not possible to take advantage of using the full response in the unfolding process and the spectral information contained in the region up to approximately 900 keV deposited energy (~130 keV above the epithermal peak) would be lost. Monte Carlo validation of the response function for this detector has been tried by others (Sailor et al., 1988; Iguchi et al., 1994) but significant departures from experimental functions were reported.

In order to unravel neutron spectra obtained with the ^{3}He ion chamber, two types of unfolding algorithms were tried as well as a third simplest method consisting of dividing the measured spectrum by the energy dependent peak efficiency of the detector (called 'simple division by efficiency' later in the text).

The first unfolding method was based on the Van Cittert iterative algorithm with Jansson constraint (Matysiak et al., 2008; van Cittert, 1931; Jansson, 1995), which was originally employed in our previous work. This method could only be applied to the spectral region above 794 keV deposited energy (above 30 keV neutron energy) due to the fact, that the number of counts in the remainder of the epithermal peak was still approximately two orders of magnitude more than in the fast neutron (above 30 keV neutron energy) part of the spectrum. With such a dominant feature present in the spectrum, the absolute value of the corrections made by the algorithm in each iteration step was governed by the corrections needed to be applied to the high intensity region only (below 30 keV neutron energy). As the initial guess of the first estimate of the spectrum in the iterative algorithm, the simple division by efficiency was used.

The second unfolding method was based on the constrained regularized inversion implemented in the Contin code (Provencher, 1982). This method allows for successful unfolding of the measured spectra using the response function above 300 keV (above the gamma-ray response of the detector), therefore taking into account the part of the recoil continuum below the epithermal peak.

The third method used was the simple division by the energy dependent peak efficiency of the detector. This technique does not take into account the recoil and wall effect continua, therefore it was expected that the lower neutron energy part of the unfolded spectrum would be overestimated. In the performance comparison between the Van Cittert and the constrained inversion methods, the simple division by efficiency was used as a reference, so that the difference between the simple method and the two above could be used as an indicator of the amount of the corrections made by the two unfolding algorithms due to the wall effect and recoil continua.

Figure 4.14 presents the unfolding results obtained with the three methods described above applied to neutron spectra taken for three incident proton energies: 1.95, 2.1, and 2.3 MeV.

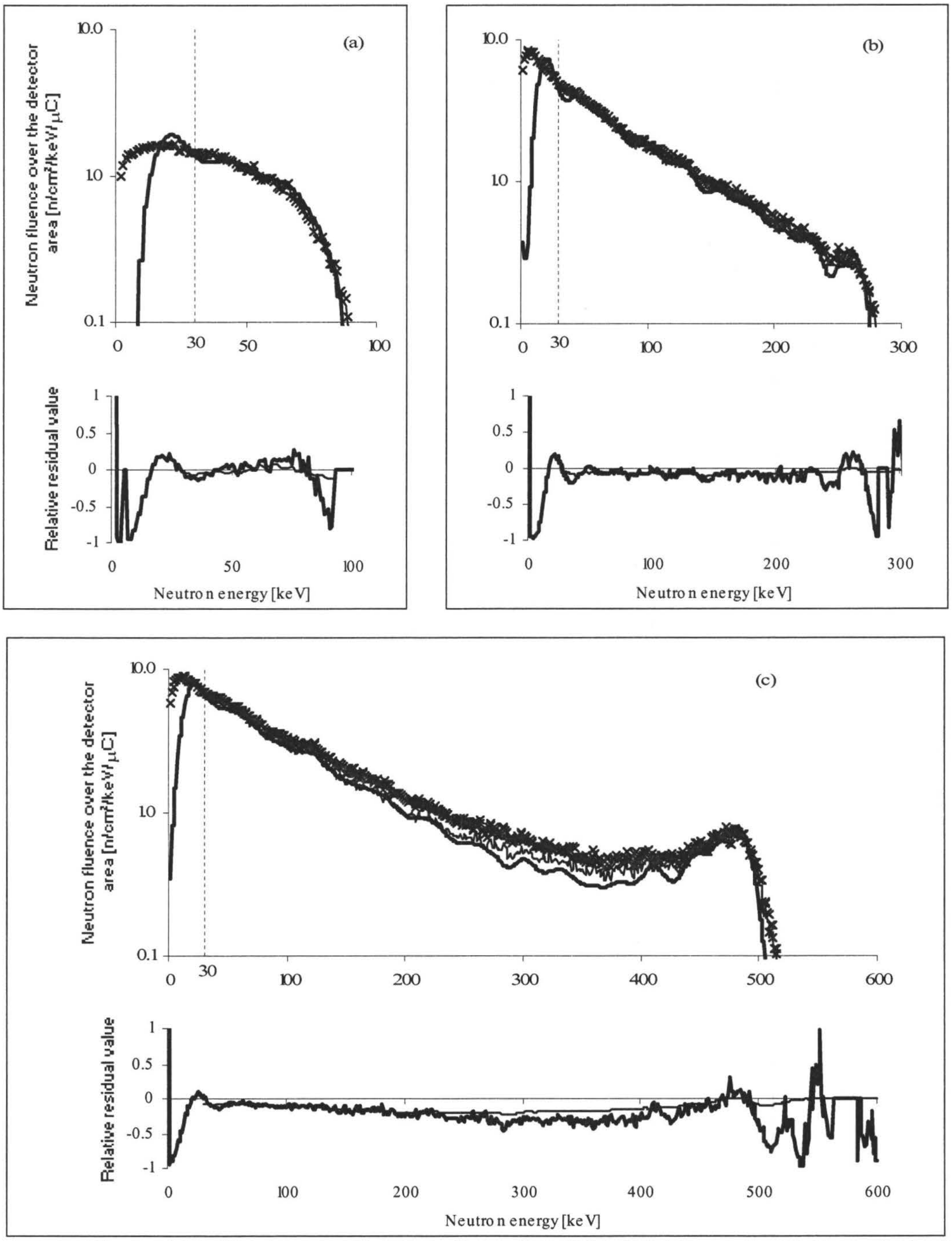

Figure 4.14: Neutron spectra (top figures) unfolded using constrained regularized inversion (solid thick line), Van Cittert iterative algorithm with Jansson constraint (solid thin line), and obtained by dividing by peak efficiency (crosses) for three incident proton energies: (a) 1.95 MeV, (b) 2.1 MeV, and (c) 2.3 MeV. Below each figure are shown corresponding residual values (see discussion in the text).

The top graphs in Figure 4.14 shows the unfolded neutron spectra with the three methods and the bottom graphs shows relative residual values with respect to the simple division by efficiency method.

Figure 4.14 (a) shows neutron fluence spectra obtained at the proton energy of 1.95 MeV. All three unfolding methods give similar results in the higher energy portion of the spectrum down to approximately 50 keV. Below that value, the constrained inversion method shows spurious oscillations. In the region between approximately 0 and 20 keV the spectrum obtained using the simple division by efficiency shows neutron fluence higher than the result obtained with the constrained inversion, however, the constrained inversion is more reliable in this region because it uses also the information contained below the epithermal peak to unravel the value of neutron fluence in this region (i.e. the second half of the epithermal peak below 764 keV as well as the wall effect and recoil continua). It is important to mention here, that the energy resolution of the ^{3}He ion chamber in this region is approximately 15 keV therefore measurements of the spectrum in this energy range should be treated with this accuracy. The corresponding graph showing residuals indicates that for most of the spectral range above approximately 50 keV, the values of residuals are small therefore if the spectrum has good statistical quality, unfolding is not necessary and simple division by efficiency suffices for estimation of the neutron fluence. This behavior was expected because the peak fraction of the detector response above the epithermal peak for neutrons up to approximately 300 keV is high. This can be seen in Figure 4.14 (b), where the neutron spectra are not considerably different regardless of the unfolding method used. Relative residual values show that the simple division by efficiency method overestimates the neutron fluence by approximately 10%. Similarly, significant differences in results can be noted in the lower neutron energy part of the spectrum between 0 and 30 keV.

In Figure 4.14 (c), the results of the three unfolding methods differ appreciably. Both unfolding algorithms apply significant corrections to the middle portion of the spectrum making the ^{7}Li(p,n) resonance peak around 500 keV more pronounced. The correction made to the lower part of the spectrum is higher in case of the constrained inversion algorithm than in the case of the iterative algorithm. Here, the application of the unfolding algorithm prevents overestimation of the neutron fluence spectrum by simply dividing the above epithermal neutron part of measured spectrum by energy dependent efficiency.

Chapter 5

MEASUREMENTS OF THE NEUTRON SPECTRUM FROM THE ^{7}Li(p,n) ACCELERATOR BASED NEUTRON SOURCE AT VARIOUS PROTON ENERGIES AS WELL AS ANGLES AND DISTANCES FROM THE LITHIUM TARGET

5.1. Summary

In this chapter, neutron spectra from the ^{7}Li(p,n) source in continuous proton current mode collected with the ^{3}He ion chamber are presented.

First, neutron spectra were acquired for the laboratory emission angles between 0 and 90 degrees with respect to the incident proton beam axis, at a fixed proton energy of 2.35 MeV, and with the detector positioned at a distance of 3 m from the lithium target. Relative shapes of the collected spectra were qualitatively compared with analytically calculated neutron fluence spectra based on the ^{7}Li(p,n) reaction cross-section and kinematics. The comparison showed that the calculated maximum neutron energies for neutron emission angles higher than approximately 30 degrees were consistently lower than the measured values. It was concluded that the presence of the high energy neutrons at higher angles results from neutron scattering on the target assembly components and the walls of the experimental area.

Next, results of the neutron spectra measurement at the proton energy of 2.3 MeV and distances between 0.64 and 3.7 m in a forward direction are shown. Similarly, analytical neutron fluence spectra were calculated for the corresponding detector positions. The analysis revealed that the analytical kerma overestimates the experimental by a factor of two, even when accounting for the negative proton energy offset. The main reason for this discrepancy stems from the fact that the experimental spectra show a systematic shift of neutron spectrum toward lower

energies due to moderation. The ^{3}He kerma measurements were supported by TEPC dosimetry, and the agreement between the two methods was within approximately 20 % for lower proton energies, but increased to ~50 % for higher proton energies.

Finally, neutron spectra measured at proton energies between 1.95 and 2.3 MeV at a fixed distance of 3.7 m in a forward direction are presented. In the same manner, the analytical spectra were calculated for the corresponding proton energies and additionally, a Monte Carlo model consisting of the target assembly and the walls of the experimental area was built to account for neutron scattering. The agreement between the experimental values and both the analytical and MC results was within ~ 30 %.

In the last section of this chapter sources of experimental error are discussed. As the major contributors, the efficiency function of the ^{3}He detector, precision of the proton energy offset estimation, and scattering conditions in the experimental area are identified. The consistency between results given by the two models of the TEPC detectors is also discussed.

5.2. Instruments and methods

A series of measurements with the ^{3}He spectrometer was taken at accelerator currents low enough to prevent excessive random summing, which was done by keeping the total counting rate of the detector from exceeding 1,000 cps.

First, angular distribution of the neutron emission from the target was measured to qualitatively determine if the maximum neutron energy at each emission angle follows calculated values based on cross-section and kinematics of the ^{7}Li(p,n) reaction (Matysiak et al., 2008; Lee & Zhou, 1999; Liskien & Paulsen, 1975). The level of agreement between the calculated and experimental values can help estimate the significance of the scattering fluence in the experimental area.

In order to investigate this scattering component further, measurements with the ^{3}He spectrometer at varying distances from the target in the forward direction were taken and the raw spectra were unfolded using the iterative Van Cittert algorithm with Jansson constraint (Matysiak et al., 2008; van Cittert, 1931; Jansson, 1995). The experimental neutron fluence spectra were compared with those obtained from analytical treatment of the ^{7}Li(p,n) reaction. Unfolding the raw ^{3}He neutron spectra was based only on the above 794 keV part of the detector response function (above 30 keV neutron energy) in order to avoid the interference of the epithermal peak. As shown in the previous chapter, with proton energies up to approximately 2.1 MeV, the results of unfolding using the full response function of the ^{3}He detector, and only the part above 30 keV, are very close. At the proton energy of 2.3 MeV, the difference in integrated neutron fluence above 30 keV between the spectra obtained using the full detector response and only the part above 30 keV is 2 %, which results in a total difference in kerma of less than 5 %. The use of the complete response function was possible in that study only because the size of the epithermal peak was reduced by an active rejection of slow neutrons (Matysiak, Chin, McMaster, Prestwich, & Byun, 2009). In the case where slow neutrons were not rejected, unfolding using the full response of the detector was not possible. However, the active rejection of slow neutrons requires operating the accelerator in the proton chopper mode, which reduces the effective proton current by a factor of at least 100 (duty cycle efficiency). Even though the accelerator was operated at the maximum instantaneous proton current (approx. 60 μA), the effective current on the target was less than 0.6 μA. This resulted in very low counting rates in the detector at proton energies close to the reaction threshold. We concluded therefore, that the 5 % overestimation of the neutron fluence by using the only above 794 keV part of the response function is acceptable and decided to use continuous current acquisitions for these investigations. The part of the neutron spectrum between 0 and 30 keV could not be reliably unfolded even using the full response of the detector; therefore, no additional sacrifices were made by applying only the part of the response above 794 keV in the unfolding process. Finally, in order to obtain total neutron kerma, the unfolded neutron fluence spectra were multiplied by fluence to kerma conversion coefficients (Chadwick et al., 1999).

In our previous work with the ^{3}He detector (Matysiak et al., 2008), we noted that there is a discrepancy between the Monte Carlo modeled intrinsic efficiency and experimentally reported values (Beimer et al., 1986), so therefore it is important to verify the neutron dose found by using the ^{3}He detector with an independent measurement. The microdosimetric technique with tissue equivalent proportional counter was chosen, because the TEPC detector can be easily calibrated with the internal α radiation source, as well as due to the fact that the neutron dose can be separated from the gamma-ray dose.

In the last experiment, ^{3}He neutron spectra were collected for five nominal incident proton energies, from 1.95 to 2.3 MeV, at a fixed distance from the lithium target in a forward direction. The collected spectra were unfolded using the iterative method and compared with analytically calculated neutron fluence spectra. As mentioned before, the neutron source spectrum is modified by scattering on the elements of the target assembly and walls of the experimental area; therefore, an attempt was made to account for these objects by creating a Monte Carlo model of the target assembly and walls of the experimental area. As the Monte Carlo method engine, the MCNP5 code (Briesmeister, 1997) was employed.

5.3. Results

5.3.1. Neutron spectrum measurements with the ^{3}He ion chamber

Throughout the experiment, the ^{3}He detector used a digital pulse processing unit (model DSPec, ORTEC) with shaping parameters for the incoming pulses set at 8 μs rise time and 2 μs flat top. 1024 pulse height channels were found to be sufficient for the energy resolution of the acquired spectra. For each acquisition, the total proton charge delivered to the target was monitored by the target current integrator, and the total neutron yield stability was monitored by collecting the total number of counts for the same period with a long counter. Figure 5.1 shows the schematic diagram of the acquisition system.

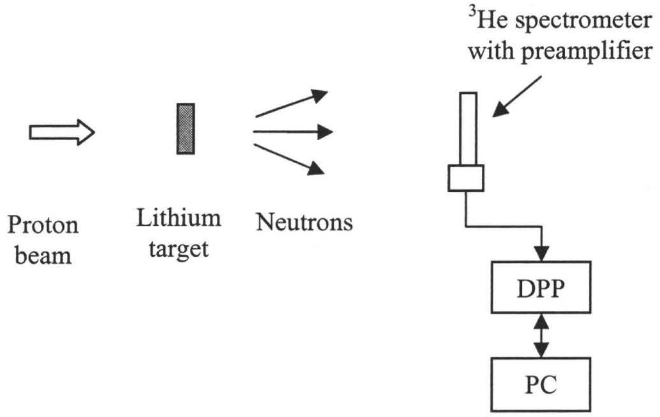

Figure 5.1: Schematic diagram of the acquisition system used for neutron spectroscopy with the ^{3}He ionization chamber.

5.3.2. Angular distribution of neutron emission from the target

In order to verify angular neutron emission distribution from the lithium target, a series of measurements was conducted with the ^{3}He detector at different angles with respect to the incident proton beam axis. For better positioning accuracy the main axis of the detector was aligned with neutron emission direction (Figure 5.2). The 2.35 MeV nominal proton energy was selected for this experiment because analytically calculated angular neutron yield distribution for this energy is strongly forward directed, with the maximum neutron energy correlated with the emission angle (the larger the angle, the smaller maximum neutron energy), so therefore departures from the analytically calculated maximum neutron energies could be straightforward to identify.

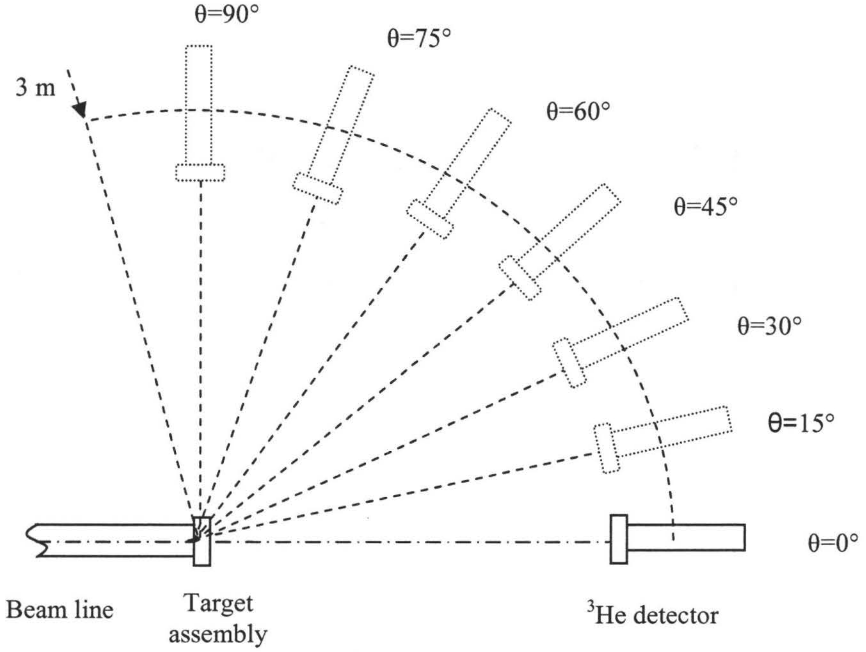

Figure 5.2: Experimental arrangement for the angular neutron emission distribution measurement.

First, the dependence of the detector orientation with respect to the neutron propagation direction was investigated. Two measurements, one with the detector parallel to the neutron propagation direction, and the other with the detector positioned perpendicularly, were taken.

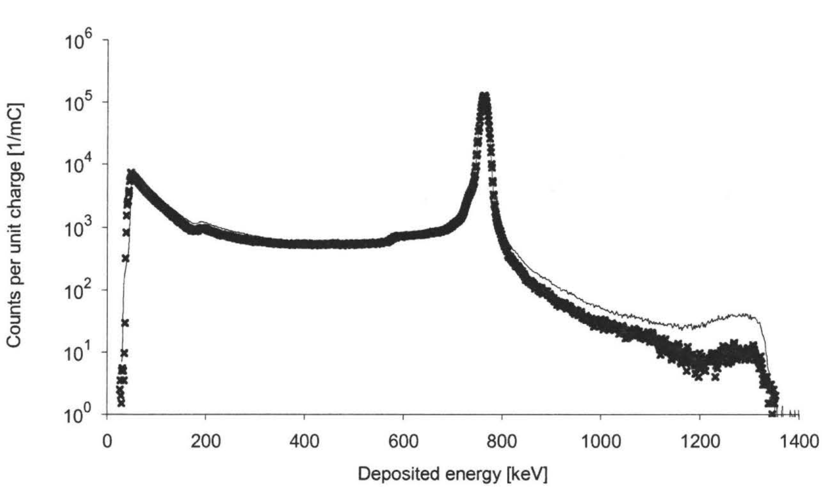

Figure 5.3: Comparison of ^{3}He normalized raw neutron spectra in forward direction at 2.35 MeV with the detector positioned parallel (crosses) and perpendicular (solid line) to neutron propagation direction.

As shown in Figure 5.3, the difference between the two spectra is notable, especially in the high neutron energy region. The epithermal peak size and recoil continua are very close, which was expected because the slow neutrons do not originate from the primary fluence (almost no low energy neutrons are produced from the ^{7}Li(p,n) reaction) but result from moderation, and therefore are independent of the detector orientation. Even though the high neutron energy parts of the two spectra show a difference in intensity, the maximum neutron energies measured with the two detector arrangements are consistent.

As described in the previous chapter, there is a negative energy offset between the proton energy indicated by a generating voltmeter (GVM) of the accelerator terminal and the effective proton energy found from the raw ^{3}He neutron spectra based on maximum neutron energy. In order to measure maximum neutron energy values from raw spectra consistently, we adopted a simple graphical method: with the spectrum printed with a logarithmic ordinate, a straight line is fitted to the falling slope of the high energy edge. The point at which the spectrum diverges from the straight line is considered the maximum deposited energy (Figure 5.4). This method was described in detail in another study presented in the next chapter, and can be used to determine maximum neutron energy in the spectrum with approximately 10 keV accuracy.

Using this method, the maximum neutron energy in the forward direction was found from the raw ^{3}He spectrum.

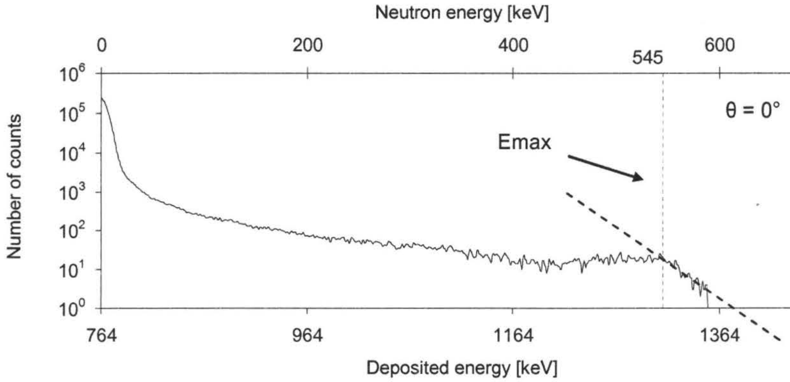

Figure 5.4: Raw neutron spectrum in forward direction for nominal proton energy of 2.35 MeV. Maximum neutron energy found using the graphical method (dashed lines) is 545 keV.

As shown in Figure 5.4, the value of maximum neutron energy in forward direction was found to be 545 keV, which corresponds to the effective incident proton energy of 2.275 MeV. Using this proton energy, neutron fluence spectra were calculated for five emission angles between 15 and 90 degrees and folded with the ^{3}He detector response.

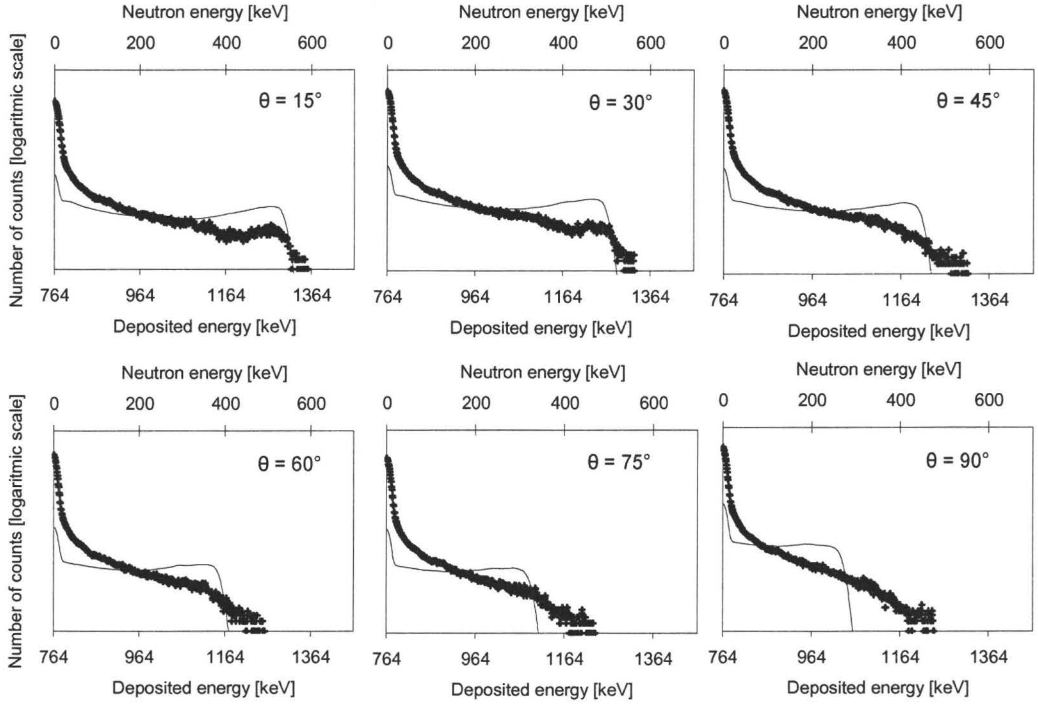

Figure 5.5: Raw neutron spectra for emission angles between 15 and 90 degrees (crosses). The ^{3}He detector was positioned 3 m from the target, with the main detector axis parallel to the neutron propagation direction. For comparison, analytically calculated raw ^{3}He spectra are also shown (solid line). Analytical spectra were multiplied by an arbitrary number so that the shapes of both spectra could be shown on the same graph.

Figure 5.5 shows the raw measured spectra as well as the analytically calculated raw ^{3}He spectra for six angles between 15 and 90 degrees. It is clear, that the analytical spectra do not correspond well with the measured ones, especially for larger angles. The measured spectra do not show significant variation with the angle, and their maximum neutron energies vary between ~ 500 and 600 keV, whereas the calculated values change significantly from 545 keV (0 degrees) to 265 keV (90 degrees).

5.3.3. Neutron spectra and doses in zero degree direction at various distances from the target.

In this experiment, neutron spectra and doses from the ^{7}Li target were measured with the ^{3}He and TEPC detectors. First, raw ^{3}He neutron spectra were collected at the nominal energy of 2.3 MeV at five distances from the lithium target in a forward direction. The 2.3 MeV energy was chosen because it gives relatively high fast neutron count rate compared with lower proton energies. The distances chosen for the measurement were between 0.64 m and 3.7 m. The minimum distance of 0.64 m was arbitrarily chosen because significant relative positioning and solid angle estimation errors increase with decreasing distance. The maximum distance of 3.7 m was limited by the dimensions of the experimental area.

The experimentally acquired spectra were unfolded using the van Cittert iterative algorithm with Jansson constraint using the response function reported by Beimer (Beimer et al., 1986). The response was extended to 30 keV neutron energy as described in the previous chapter.

In the same manner as in the previous section, the proton energy offset was identified using the graphical method. For the nominal energy of 2.3 MeV, a negative offset of 57 keV was identified, so therefore 2.243 MeV effective proton energy was adopted and analytical fluence spectra for this energy were calculated at five distances from the target, between 0.64 and 3.7 m. Figure 5.6 shows comparison of the experimental and analytical results.

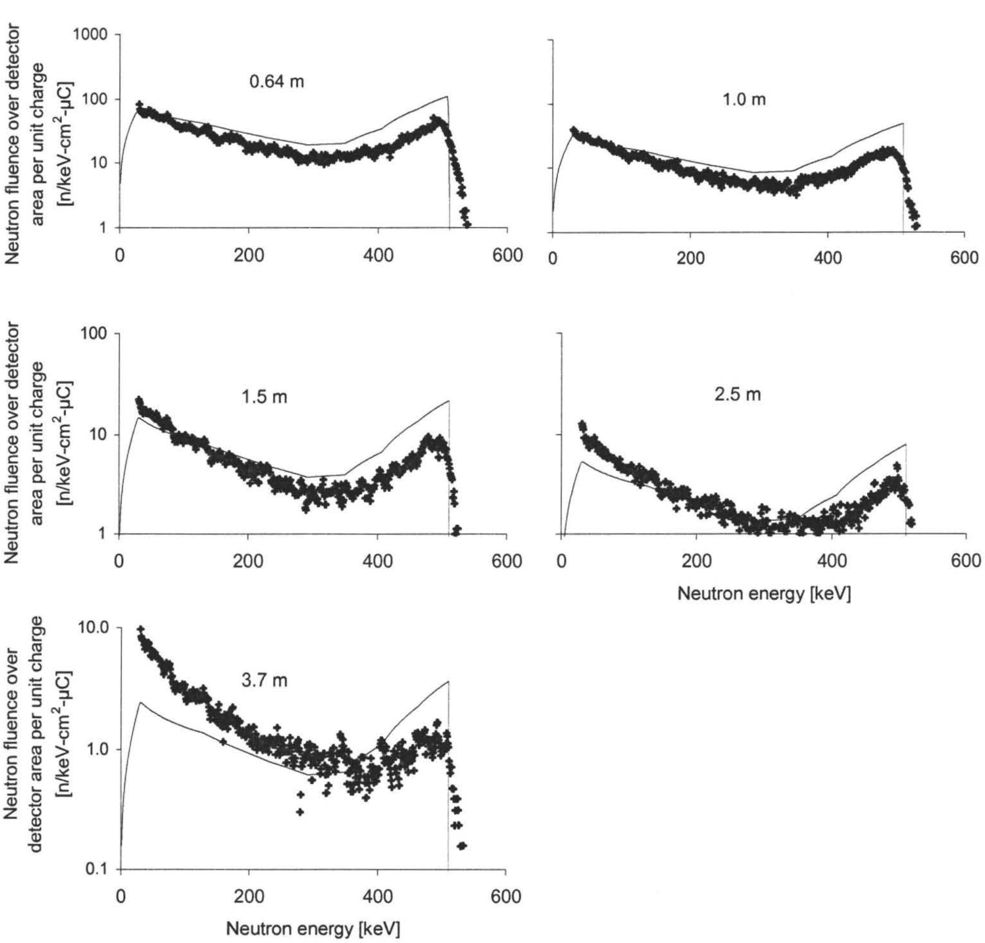

Figure 5.6: Unfolded ^{3}He measured neutron spectra at nominal proton energy of 2.3 MeV (crosses) and corresponding analytical neutron spectra at effective proton energy of 2.243 MeV (solid line) for various distances from the target in forward direction.

At all distances, the high neutron energy component of the analytical spectra is always higher than in the measured spectra. Also, the lower energy component of the measured spectra increases with the distance from the source. Using fluence to kerma conversion coefficients, the total neutron dose was calculated from the unfolded neutron spectra. Figure 5.7 shows a summary of measured versus calculated neutron kerma for all investigated distances.

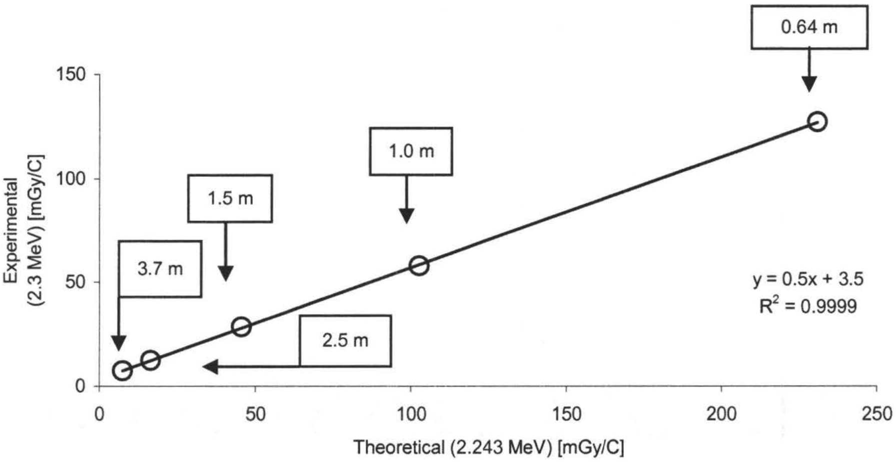

Figure 5.7: ^{3}He detector experimentally measured vs. analytically calculated neutron kerma at zero degrees for various distances from the target.

A linear fit to the experimental data points shows very good linearity between experimental and analytical kerma with a proportionality coefficient of 0.5.

To verify the ^{3}He detector kerma measurements in an absolute sense, microdosimetric measurements with two TEPC detectors (½" and 5") were also taken at the same distances as the ^{3}He detector measurements. The ½" detector efficiency was not sufficient to accumulate good quality spectrum at higher distances, so 2.5 and 3.7 m measurements are not presented here.

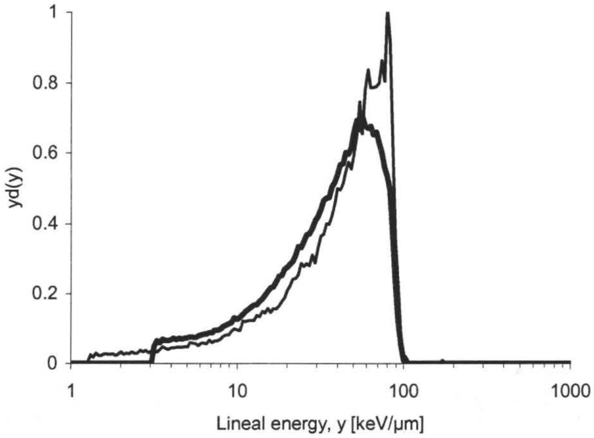

Figure 5.8. Microdosimetric spectra collected with the ½" TEPC (thin line, 3600 s acquisition time) and 5" TEPC (thick line, 900 s acquisition time) at 1 m from the target in forward direction at 2 μA current and 2.3 MeV nominal proton energy.

Figure 5.8 shows example microdosimetric spectra taken with the two TEPC detectors at a distance of 1 m. The 5" detector has better intrinsic efficiency and covers greater solid angle, therefore the acquired spectrum has better statistical quality when compared with the ½" detector, where statistical fluctuations are significant even though the collection time for the small detector was four times longer than for the big detector. The proton recoil edge for the small detector is steeper than for the big detector, and the lower energy part indicates a systematic shift between the two spectra. The shift may be explained by the fact, that the ½" detector lineal energy calibration may not be reliable. A gravitational shutter used in the detector may not have opened to point at the diameter of the detector active volume, but instead pointed at a shorter cord length. Calibration of the 5" TEPC is based on a magnetic shutter and is more reliable. The gamma-ray dose component for the two spectra is not significant, so no effort was made to subtract it from the total dose.

Table 5.1 presents a summary of the ^{3}He and TEPC dose measurements at 2.3 MeV at various distances from the target.

Table 5.1: Comparison of ^{3}He ion chamber and TEPC neutron dose measurements at zero degrees for various distances from the target at 2.3 MeV nominal proton energy (2.243 MeV effective energy).

Distance from the target [m]	0.64	1.0	1.5	2.5	3.7
Analytically calculated kerma above 30 keV for 2.243 MeV [mGy/C]	230.9	102.6	45.6	16.4	7.5
^{3}He neutron kerma above 30 keV [mGy/C]	127.5	57.8	28.5	12.4	7.4
½" TEPC dose [mGy/C]	119	47	23	-	-
5" TEPC dose [mGy/C]	104	43	19	7.2	3.8

All three detectors show doses consistent within approximately 20 % for smaller distances but the discrepancy between results obtained with the ^{3}He and TEPC detectors increases with the distance and reaches ~ 50% at 3.7 m. Also, an approximately factor-of-two difference is present between the TEPC measured and the theoretical doses. Both TEPC measurements show lower values than those measured with the ^{3}He detector, which may be attributed to the efficiency of the ^{3}He detector, which has not been experimentally verified in the neutron energy region below ~ 130 keV. The overall discrepancy between the measured and calculated values may be explained with the help of neutron spectra, which indicate a significant amount of scattering occurring in the experimental room. The factor of two difference at smaller distances reduces to a good agreement at 3.7 m, which may be explained by the fact, that according to Figure 5.7, at this distance, half of the kerma originates from secondary fluence.

5.3.4. Neutron spectra acquired for proton energies between 1.95 and 2.3 MeV

In this experiment, neutron spectra were collected with the ^{3}He ion chamber in the proton energy region between 1.95 and 2.3 MeV. The acquired spectra were unfolded using the iterative algorithm and compared with analytically calculated neutron fluence spectra.

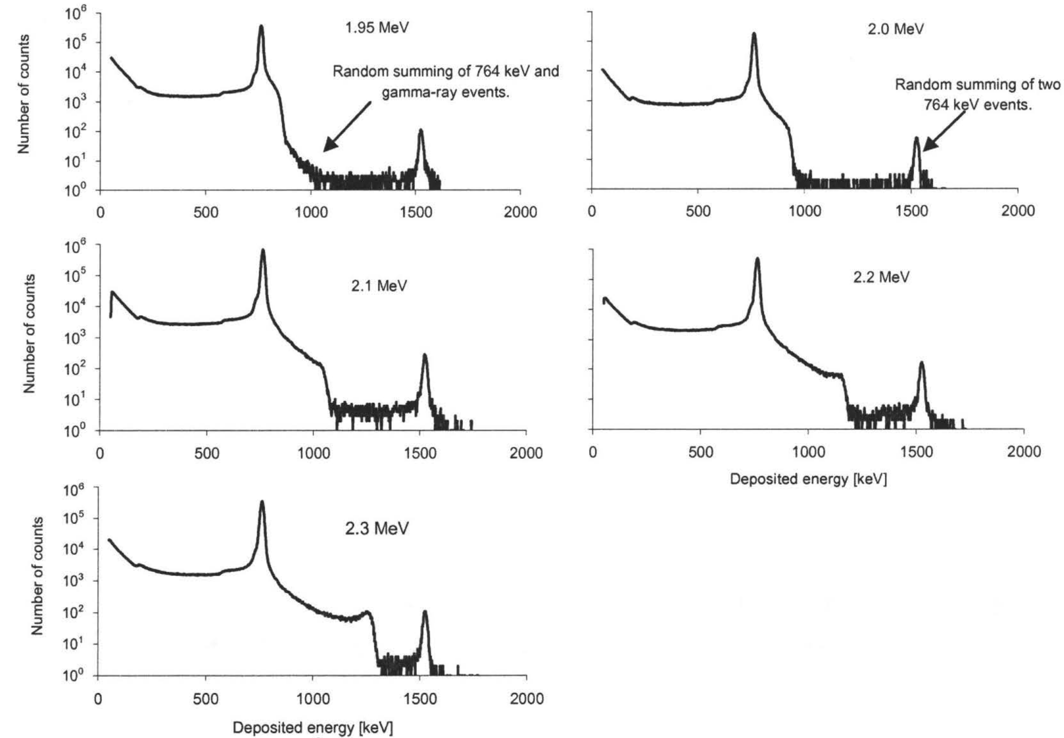

Figure 5.9: Raw ^{3}He neutron spectra in forward direction acquired at nominal proton energies between 1.95 and 2.3 MeV. The detector was positioned perpendicularly to the proton beam axis at a distance of 3.7 m from the target in forward direction.

The proton current in all acquisitions was selected such that the total counting rate in the detector did not exceed 1000 cps. Even though the count rate was low, the double epithermal peak at 1528 keV originating from the random summing of two 764 keV epithermal peak events is present in all collected spectra (Figure 5.9). Some random summing events are also present in the region between the double epithermal peak and the high neutron energy edge, especially for the 1.95 MeV proton energy spectrum (Figure 5.9 top left graph), where the events from the gamma-ray response of the detector undergo summation with the events scored in the epithermal peak. This structure is visible as a triangular shape extending above the fast neutron response, but the number of these events is small.

In the same manner as in the previous section, the effective proton energies for each spectrum shown in Figure 5.9 were determined using the graphical method. In Table 5.2, values of the proton offset are summarized.

Table 5.2: Nominal and effective proton energies for neutron spectra measured with the ^{3}He ion chamber for nominal proton energies from 1.95 to 2.3 MeV.

Nominal proton energy [MeV]	1.95	2.0	2.1	2.2	2.3
Effective proton energy [MeV]	1.900	1.948	2.042	2.145	2.243
Proton energy offset [keV]	-50	-52	-58	-55	-57

Using the effective proton energy values, analytical neutron energy spectra based on the reaction kinematics were calculated. Also, in order to account for scattering, the Monte Carlo method was used to simulate the target assembly and the experimental room walls.

The experimental fluence spectra were unfolded using the iterative algorithm. Figure 5.10 shows comparison of the experimental unfolded neutron spectra with the Monte Carlo simulation and the analytical spectra.

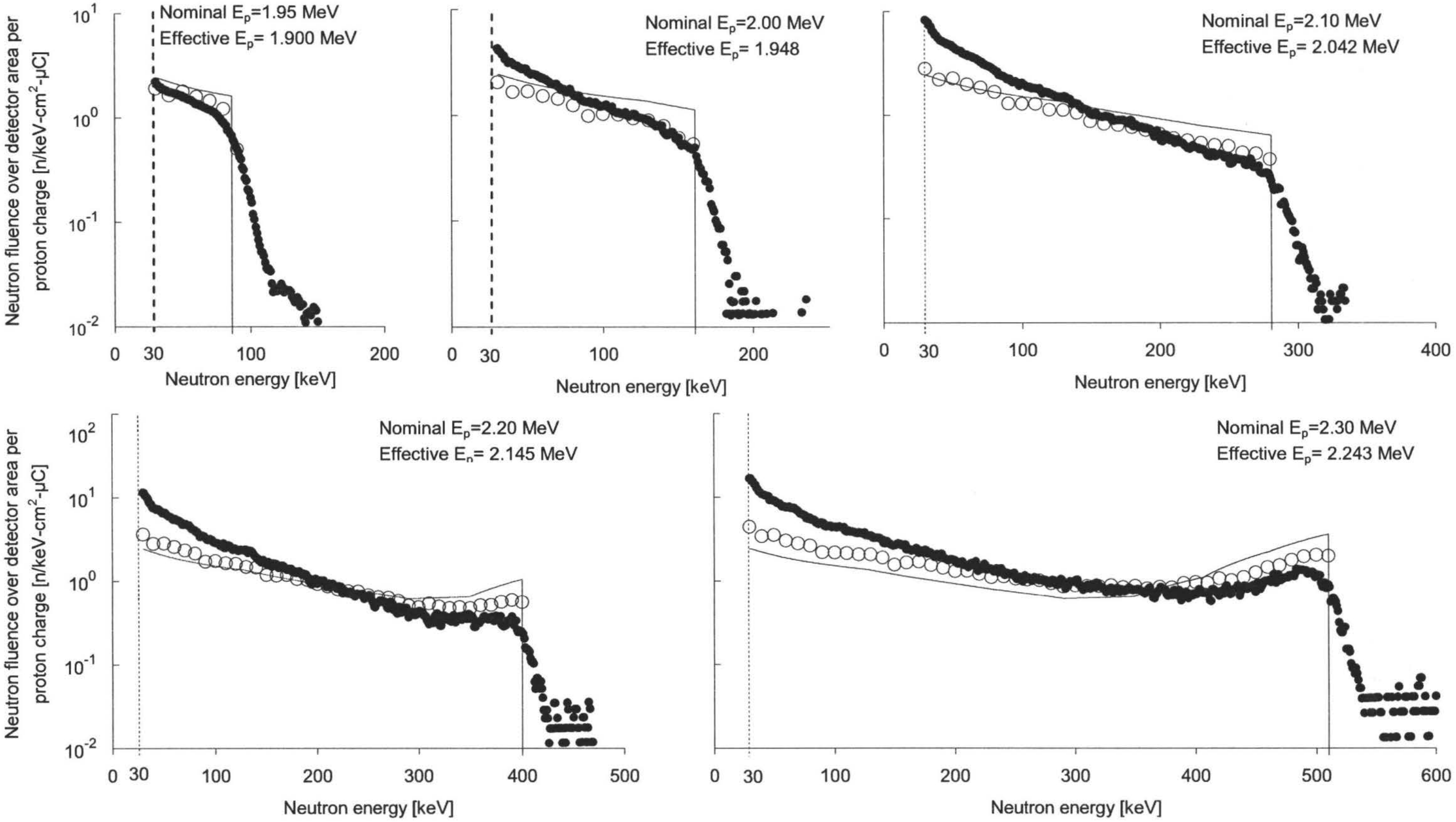

Figure 5.10: Comparison of experimental neutron fluence spectra (dots), obtained with Monte Carlo simulations (open circles), and calculated analytically (solid thin line).

From the comparison of measured and calculated spectra, it is apparent that the measured spectra show consistently lower values of higher energy neutron fluence, and at the same time, their lower energy component is higher than theoretically predicted. This neutron energy shift toward lower energies is caused by neutron scattering. The results of the MC simulations which attempt to account for scattering agree better with the experiment for lower proton energies, but for higher proton energies show values closer to the analytical results. Table 5.3 quantitatively presents neutron kerma based on calculations and measurements.

Table 5.3: Comparison of experimental, Monte Carlo, and analytically calculated neutron kerma over the detector area above 30 keV for proton energies between 1.95 and 2.3 MeV.

Nominal proton energy [MeV]		1.95	2.0	2.1	2.2	2.3
Effective proton energy [MeV]		1.900	1.948	2.042	2.145	2.243
Experimental neutron kerma above 30 keV [mGy/C]		0.37	1.1	2.6	4.4	9.1
Monte Carlo kerma for effective proton energy [mGy/C]	above 30 keV	0.38	0.84	1.9	3.4	7.5
	below 30 keV	0.10	0.14	0.21	0.28	0.36
Analytical kerma for effective proton energy [mGy/C]	above 30 keV	0.47	1.2	2.3	3.5	7.4
	below 30 keV	0.07	0.07	0.07	0.07	0.07

For low proton energies the experimental kerma values were below those calculated analytically, but with increasing proton energy the experimental kerma became higher than the analytical, so that at 2.3 MeV the difference between the two results reached ~ 20 %. Kerma values based on MC simulations show results close to experimental at 1.95 MeV, but for higher energies the MC results underestimate the experimental values by ~ 30 %. The part of total kerma below 30 keV which could not be measured with the ^{3}He detector was estimated with the

MC method. At the nominal proton energy of 1.95 MeV, this portion of kerma constitutes approximately one-fifth of total kerma, but for the maximum proton energy (2.3 MeV), reduces to less than 5 %.

5.3.5. Estimation of the experimental error in neutron dose measurements

All experimental spectra used for dose calculations were acquired with sufficient statistical quality. However, results of the measurements show uncertainties higher than those calculated based only on the statistical analysis of the data, which indicates that the systematic errors are more significant.

In neutron spectrum measurements with the ^{3}He ion chamber, detection efficiency and the shape of the response function used in unfolding contribute to the systematic error. Experimentally, the efficiency was verified only in the neutron energy range from 130 to 3000 keV (Beimer et al., 1986), but for this study the efficiency and response function were extrapolated from 130 to 30 keV without experimental verification. This also means that the portion of total kerma below 30 keV could not be measured with this detector, which contributes to systematic underestimation of the dose between 20 % (at 1.95 MeV) to approximately 5 % at 2.3 MeV (see Table 5.3).

The ^{3}He detector efficiency for perpendicular and parallel arrangements vary, therefore in the neutron field where the scattering component is present, the neutron fluence cannot be measured precisely.

Additionally, accuracy of the graphical method of estimating the maximum neutron energy from raw ^{3}He spectra is approximately 10 keV. Assessment of accuracy of this method is shown in the next chapter of this thesis.

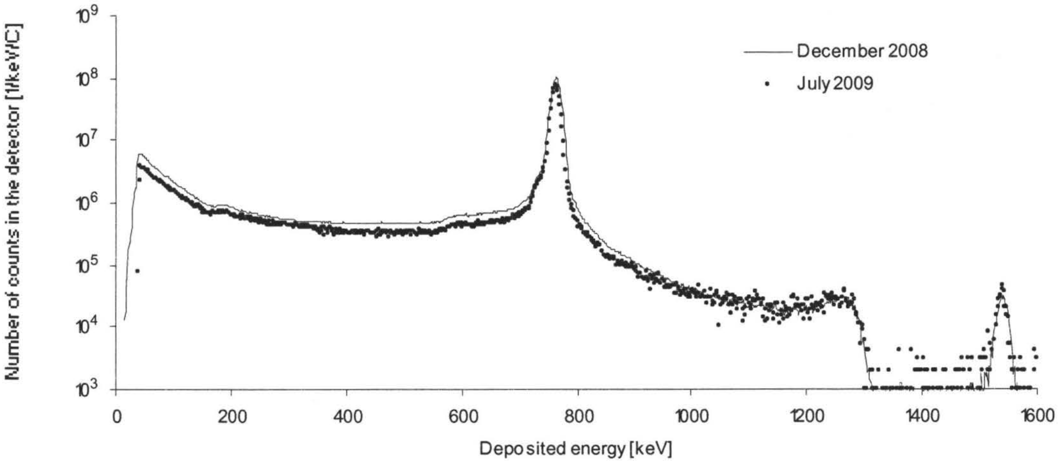

Figure 5.11: Comparison of two raw neutron spectra normalized to proton charge acquired during different experiments: presented in section 5.3.3 (Dec. 2008, solid line) and in section 5.3.4 (July 2009, dots). In both acquisitions the ^{3}He detector was positioned at 3.7 m from the target and the nominal proton energy was 2.3 MeV.

Another contributing factor in the precision of the measurements are scattering conditions in the experimental area. Figure 5.11 compares two raw spectra collected with the ^{3}He spectrometer at identical conditions normalized to proton charge but taken seven months apart. The fast neutron part of both spectra above approximately 1 MeV deposited energy is consistent in both measurements, which indicates that the target condition was stable. However, the lower fast neutron energy part, epithermal peak, and recoil continuum of the December measurement is higher, which suggests that scattering conditions in the experimental area were different in these two experiments.

Table 5.4: Summary of two independent ^{3}He neutron spectra measurements at 2.3 MeV and 3.7 m from the target.

	December 2008	July 2009
Proton current [μA]	0.3	0.5
Acquisition time [min]	180	15
Neutron kerma above 30 keV [mGy/C]	9.1	7.4

As a result, neutron kerma for the December measurement is 23 % higher than for the July measurement (Table 5.4).

In microdosimetric measurements with the ½" TEPC detector, the lineal energy calibration mechanism using the gravitational shutter is not reliable. If not completely closed during measurements, events from the alpha radiation calibration source contribute to detection events, and conversely, if the shutter is not completely open during lineal energy calibration, the position of the calibration peak shifts. As a result, the doses measured with the two TEPCs show approximately 15 % difference.

Chapter 6

PRECISE MEASUREMENTS OF THE THICK TARGET NEUTRON YIELDS OF THE ^{7}Li(p,n) REACTION

In this chapter, results of the thick target neutron yields from the ^{7}Li(p,n)^{7}Be reaction are presented. The measurement was done in the proton energy range from 1.95 to 2.3 MeV by determining induced activity of the ^{7}Be. An HPGe detector was used to detect the 478 keV gamma-rays emitted through ^{7}Be decay. In order to minimize possible fast neutron damage to the HPGe crystal during irradiations, the detector was positioned behind the lithium target with its axis at approximately 135° with respect to the proton beam axis, since the angular distribution of the ^{7}Li(p,n) neutron emission is strongly forward directed. The absolute efficiency of the HPGe detector was calibrated using two mixed multigamma Eu sources. A series of irradiations with nominal proton energies of 1.95, 2.0, 2.1, 2.2, and 2.3 MeV were carried out. In an independent experiment, raw neutron spectra were collected by a ^{3}He ion chamber for the same series of proton energies. From the raw neutron spectra, it was noted that the effective proton energies were lower than the nominal by 50 to 58 keV. After corrections for the proton energy offsets were applied, the measured neutron yields matched the theoretical yields within 20 %. Long term stability of neutron yield was tested at two nominal proton energies, 2.1 and 1.95 MeV, over an experimental period of one year. The results show that the yield at 2.1 MeV was stable within approximately ±15 % and remained consistent even when the lithium target was replaced, whereas at 1.95 MeV, the maximum fluctuations reached a factor of 10.[*]

---

[*] Based on the abstract from: Precise measurements of the thick target neutron yields of the ^{7}Li(p,n) reaction, submitted for publication in Nucl. Instr. Meth. A, March 24, 2010

The content of this chapter has been submitted for publication in Nuclear Instruments and Methods Section A. The manuscript was prepared by me and revised by co-authors. The introduction and conclusion sections of the paper were removed to avoid redundancy with the information contained in the introduction and conclusion chapters of this thesis. Section numbers and the reference system were adjusted to conform to the referencing style used in the thesis. The bibliography is presented at the end of the thesis.

Precise measurements of the thick target neutron yields of the ^{7}Li(p,n) reaction

W. Matysiak[1], W.V. Prestwich[1], S.H. Byun[1]

[1]Department of Medical Physics and Applied Radiation Sciences, McMaster University,
Hamilton, ON, Canada, L8S 4K1

Submitted for publication in *Nuclear Instruments and Methods in Physics Research Section A: Accelerators, Spectrometers, Detectors and Associated Equipment*, 24 March 2010

6.1. Instruments and methods

6.1.1. Accelerator and associated equipment

[…] The accelerator based neutron source used in this study consists of the 3.0 MV Van de Graaf accelerator (model KN3000, HVEC, USA), the analyzing magnet bending the proton beam by 50°, and the lithium target assembly, as shown in Figure 6.1. Total proton charge delivered to the target is measured by the current integrator connected to the target assembly.

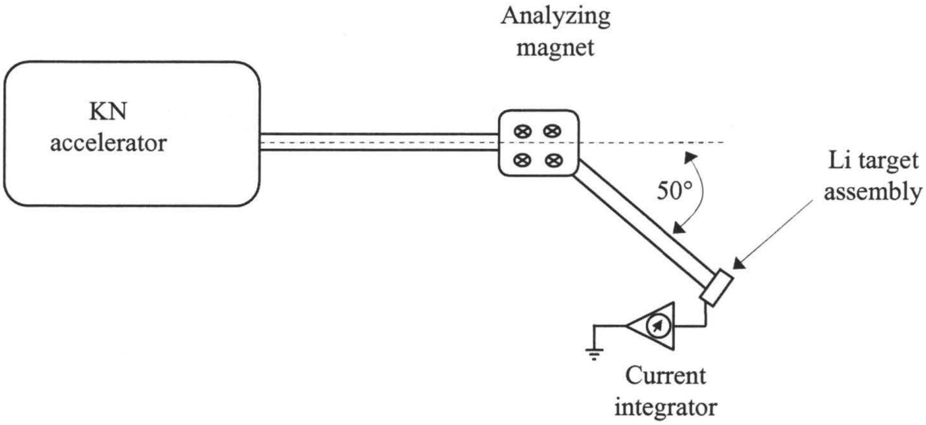

Figure 6.1: Diagram of the accelerator based neutron source used in this study.

6.1.2. Absolute neutron yield measurement using the ^{7}Li(p,n) reaction

In this study, the absolute neutron yield was determined by measuring the activity of ^{7}Be, which is the product of the ^{7}Li(p,n) reaction. ^{7}Be has a 53 day half-life and decays to ^{7}Li through electron capture. The first excited state of ^{7}Li has a branching ratio of 10.5 % and always emits a single 478 keV gamma-ray per transition, so the emission probability is 10.5 % per ^{7}Be decay. In order to relate the induced activity of the ^{7}Be to the total proton charge delivered to the target, the 478 keV gamma line counting rate before and after each proton irradiation was measured. Since decay corrections are negligible, production yield of the ^{7}Be

(Y_{Be}) per proton charge (q) delivered to the lithium target is given as $Y_{Be} = \frac{\Delta N_{Be}}{q}$, where ΔN_{Be} is the number of ^{7}Be atoms produced. In terms of measurable net increase in counting rate of the 478 keV gamma line ($\Delta\dot{C}$), ΔN_{Be} is given as $\Delta N_{Be} = \frac{\Delta\dot{C}}{p\varepsilon\lambda}$, where p, ε, and λ denote emission probability of the 478 keV gamma-ray, absolute peak efficiency of the HPGe detector, and the ^{7}Be decay constant, respectively.

The gamma-ray spectrum was collected with an N-type HPGe detector (relative efficiency 35 %, model GMX-35195, ORTEC) with a pulse processing chain consisting of a digital pulse processing unit (model DSPec, ORTEC) and an external high voltage power supply (model 3125, Canberra). Digital pulse shaping parameters used were 8 μs rise time and 2.4 μs flattop.

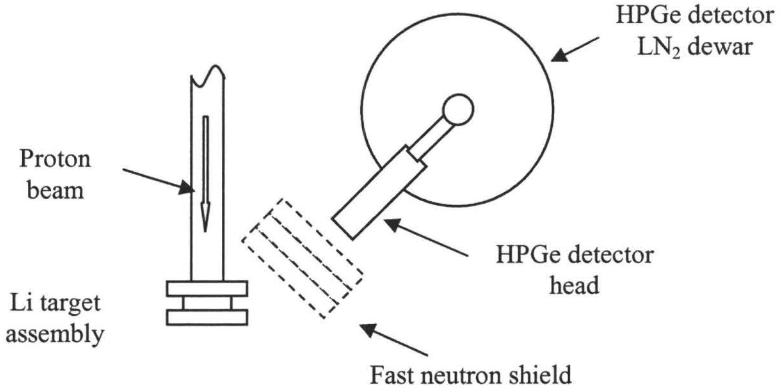

Figure 6.2: Experimental arrangement of the HPGe detector for neutron yield measurement.

Figure 6.2 shows the experimental setup for the neutron yield measurement. In order to avoid inaccuracies related to positioning of the heavy LN_2 dewar, the HPGe detector was fixed at the measurement position during irradiations. It was permanently located behind the target assembly at approximately 135 degrees with respect to the incident proton beam. The lower neutron fluence rate in the back direction reduced the probability of the germanium crystal damage by fast neutrons. The distance of 37 cm between the detector head and the lithium target was chosen to provide a space sufficient to install removable fast neutron shielding (3 layers of wax blocks, 12 cm total thickness) to reduce the possibility of neutron damage further and at the same time to give a sufficient detection efficiency. Also, the Al case of the detector was covered with cadmium sheets during irradiations to prevent it from being activated.

An attempt to collect the gamma-ray spectrum during irradiations failed, due to the extremely high event rate, which saturated the HPGe preamplifier completely. However, no indication of resolution degradation was observed after each irradiation.

In order to find the peak efficiency of the HPGe detector at 478 keV, efficiency calibration was carried out using two mixed Eu (^{152}Eu and ^{154}Eu) calibration sources (a commercial source and a locally produced one). To determine the energy dependent efficiencies at the identical condition with the ^{7}Be activity measurements, each Eu source was placed at the lithium target position. The source position was aligned so that the geometric center of the source matched the spot where the proton beam hits the lithium target. The first measurement was carried out using the commercial mixed Eu calibration source (model MGS-1, 5% uncertainty, Oxford Instruments Inc, Oak Ridge). Its current activity is ~ 10 kBq level, which required a long collection time (~ 42 hours) due to gamma-ray scatterings by the lithium target holder assembly, which elevated the background continuum of the spectrum significantly. To obtain increased peak counting rates, a new Eu source with higher activity was produced at the McMaster Nuclear Reactor. The source was made by irradiating 54.5 mg of europium oxide powder for 600 seconds at a thermal neutron irradiation site with neutron fluence rate of 5×10^{12} n/cm^{2}s. After waiting for decay of the short lived radionuclides from ^{152m}Eu and those produced from impurities, the activity of the new source was cross-calibrated with the MGS-1 source at three source-detector distances: 25, 33, and 55 cm. It turned out that the ^{154}Eu and ^{152}Eu activities of the new source were sufficient for efficiency calibration.

In order to monitor the long term stability of the neutron yield, over the experimental period of approximately one year, neutron yield was periodically measured with a locally designed long counter and the ^{3}He ion chamber. The long counter consists of a 1" BF_3 proportional counter and a cylindrical polyethylene moderator.

6.2. Results

6.2.1. Cross-calibration of the MGS-1 Eu standard with the locally produced Eu source

Two sets of measurements at three distances: 25, 33, and 55 cm from the HPGe detector head were taken (Table 6.1). In the first set, the MGS-1 standard was used and it required counting times between 20 and 26 hours as opposed to the second set, for which only short acquisition times were needed to reach sufficient statistical quality. For determination of the ^{152}Eu activity, five peaks were analyzed: 344.3, 411.1, 778.9, 964.1, and 1408 keV. For the ^{154}Eu radioisotope, only the 1274.5 keV peak was used.

Table 6.1: Data acquisition summary for cross-calibration of the locally produced strong Eu source with the MGS-1 standard.

	Distance from source [cm]	Dead time [%]	Live time [s]
Set 1 (MGS-1)	25	<1	72,000
	33		95,600
	55		82,800
Set 2 (strong source)	25	23	600
	33	15	
	55	7	

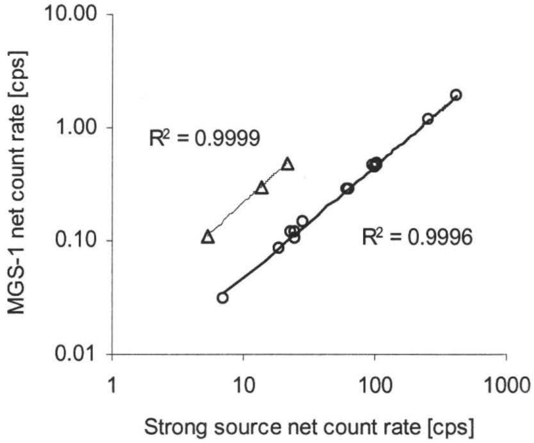

Figure 6.3: Peak counting rates of the MGS-1 standard and the strong Eu source for ^{152}Eu (circles) and ^{154}Eu (triangles) at three distances. Uncertainties due to counting statistics are insignificant.

Figure 6.3 shows the relation of the measured ^{152}Eu and ^{154}Eu peak counting rates between the MGS-1 standard and the strong Eu source. Very good linearity between peak counting rates indicates that the source positioning accuracy was sufficient. Since the statistical uncertainty is negligible, the most significant cause of error for the strong Eu source was the activity uncertainty of the MGS-1 source, therefore the 5 % uncertainty was adopted for the strong source. Table 6.2 lists activity relations between the MGS-1 standard and the strong Eu source.

Table 6.2: Results of the cross-calibration between the MGS-1 standard and the strong Eu source.

	MGS-1 standard [kBq]	Strong source [kBq]
^{152}Eu	5.34	1,196
^{154}Eu	3.29	144

6.2.2. Measurement of the HPGe detector efficiency in the target assembly configuration

In order to determine the peak efficiencies of the HPGe detector *in situ*, both the strong and the MGS-1 Eu sources were sequentially installed at the spot where the proton beam hits the lithium target. The detector remained in the same position during proton irradiations of the target. The weak MGS-1 source was counted for 81 hours in order to accumulate a good quality spectrum, whereas only 2 hour counting was sufficient for the strong Eu source. For comparison, the in-target assembly and in-air spectra are shown for the strong source in Figure 6.4.

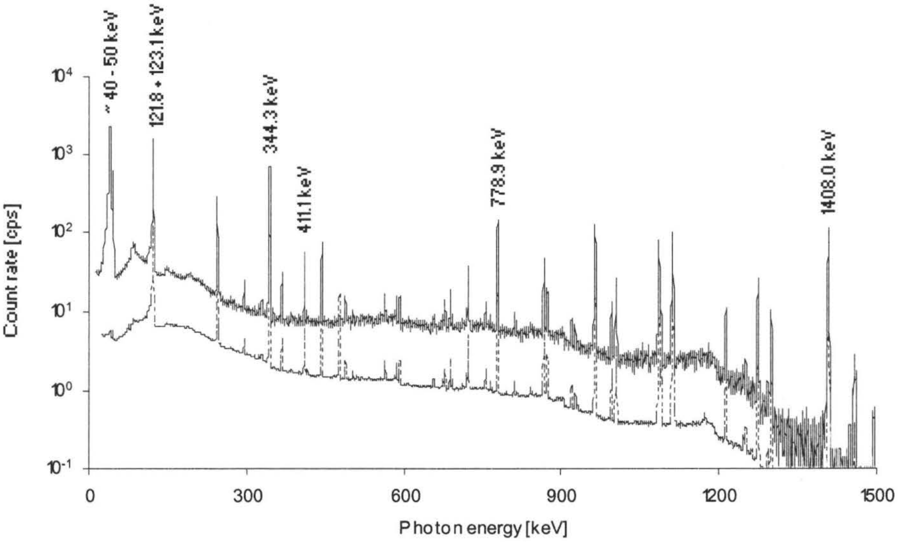

Figure 6.4: Gamma-ray calibration spectra taken with the strong Eu source in air (solid line) and mounted in the target assembly (dotted line).

Table 6.3 shows strong Eu source spectra collected for the in-air and in-target assembly arrangements. As expected, the difference in counting rates due to attenuation is more significant for lower photon energies and is very small in the energy region above 400 keV. It can be noted that the structure around 40 keV from SmKα and SmKβ characteristic X-rays was completely attenuated by the Li target assembly, and the two peaks at 121.8 and 123.1 keV were attenuated by ~ 25 %. Only approximate values of the combined counting rate for the two peaks are given because insufficient detector resolution did not allow for reliable count rate calculations of the individual peaks.

Table 6.3: Comparison of net peak count rates of the strong europium source for selected gamma-lines in air and mounted in the target assembly at the distance of 37 cm.

Gamma-ray energy [keV]	Net peak count rate [cps] In air	 In the target assembly
~ 40 to 45	~ 1343	~ 3.5
121.8 + 123.1	~ 443	~ 300
344.3	210.2	196.1
411.1	15.2	14.5
778.9	51.7	50.7
1408.0	52.2	52.6

Absolute peak efficiency values measured using the two Eu sources are shown in Figure 6.5. For each dataset, the efficiency curve was obtained by fitting a fourth order polynomial function in the energy region from 344 to 1408 keV. The difference between the experimental data points is within 1 % in the lower energy region (300 ~ 450 keV) and increases to approximately 9 % around 800 keV. From the fitted absolute peak efficiency curves, the efficiency value at 478 keV was 4.57×10^{-4} for the weak source and 4.62×10^{-4} for the strong source. The difference between these two values is within 1 % therefore it was concluded that source positioning errors were not significant and the average of the two values was adopted for further calculations.

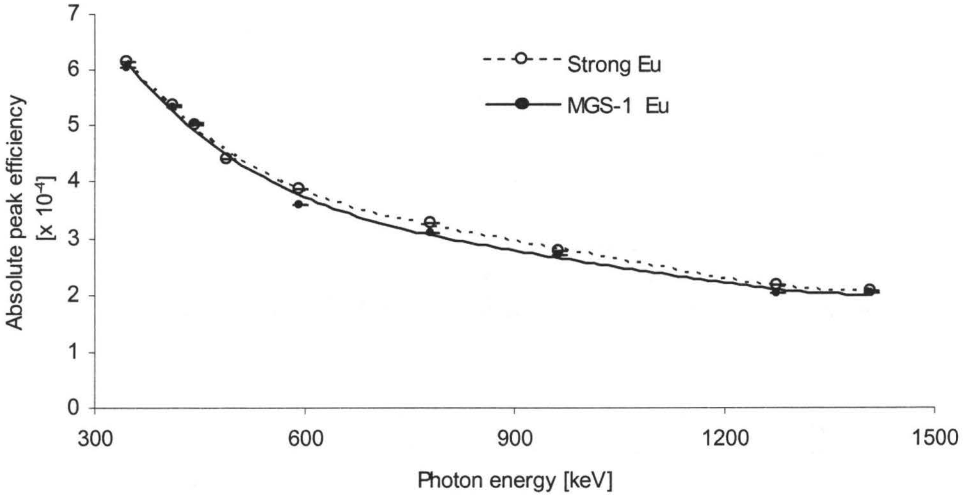

Figure 6.5. Experimental absolute peak efficiencies for the HPGe detector in the target assembly configuration obtained using the strong source (dotted line) and the MGS-1 standard (solid line).

6.2.3. Effective proton energy

Theoretical analysis of the ^{7}Li(p,n) reaction kinematics (Lee & Zhou, 1999) shows that the maximum neutron energy can be used to indicate the effective proton energy incident on the target. Figure 6.6 shows that the relation between proton energy and maximum neutron energy is almost linear, which allows for establishing the effective proton energy incident on the target independently of the accelerator proton energy calibration.

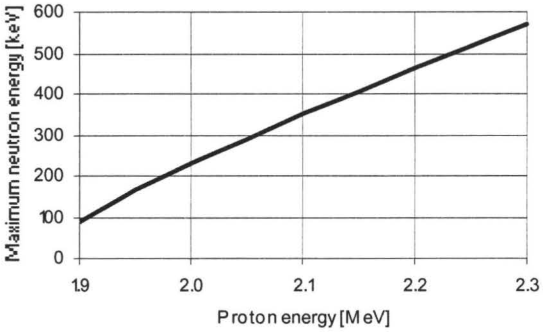

Figure 6.6: Relation between incident proton energy and maximum neutron energy for the ^{7}Li(p,n) reaction.

To find the maximum neutron energy, the ^{3}He ionization chamber was used. The detector was positioned at 3.7 m from the lithium target along the proton beam axis. The spectra were collected for five nominal proton energies: 1.95, 2.0, 2.1, 2.2, and 2.3 MeV (Figure 6.7). High neutron energy edges for all spectra are well defined and increase with proton energy.

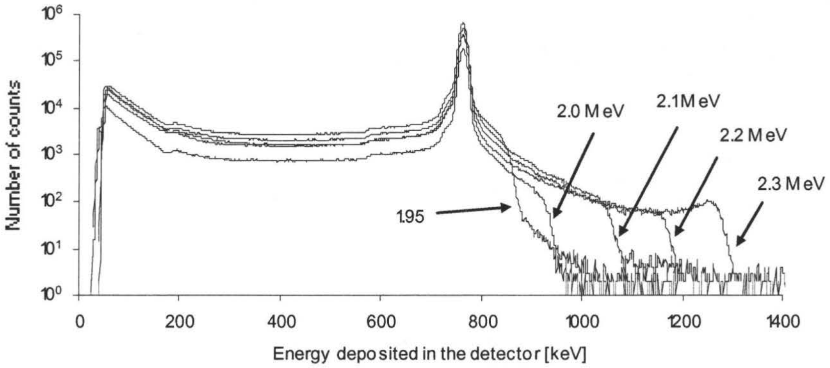

Figure 6.7: Raw neutron spectra collected for a series of nominal proton energies from 1.95 to 2.3 MeV.

For all acquired spectra, the maximum neutron energies were estimated using a simple graphical method: the spectra were printed with logarithmic ordinate and a straight line was fitted to the falling slope of the high energy edge. The point where the spectrum diverged from the straight line was considered the maximum deposited energy as shown in Figure 6.8.

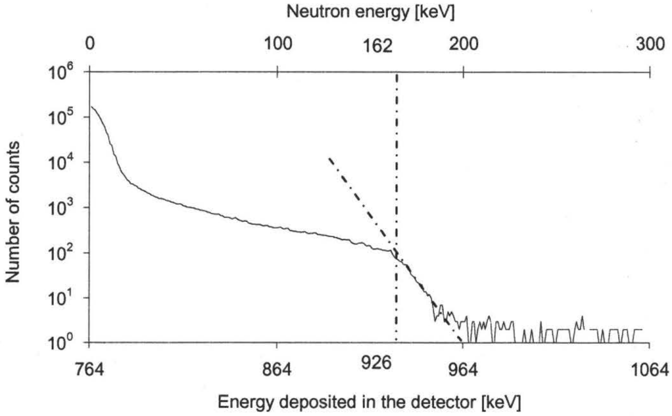

Figure 6.8: Graphical method of estimation the maximum neutron energy in the raw ^{3}He spectra. An example for the 2.0 MeV spectrum.

From the figure, the maximum neutron energy for the nominal proton energy of 2.0 MeV is 162 keV, which corresponds to an effective proton energy of 1.948 MeV.

In order to evaluate accuracy of this graphical method, it was tested using a known spectrum. Analytical thick Li target neutron spectrum for the 1.948 MeV proton energy was computed using a double differential cross-section (Liskien & Paulsen, 1975; Matysiak et al., 2008) and folded with the response function of the detector. The computed spectrum is shown in Figure 6.9 and compared with the measured spectrum for the nominal energy of 2.0 MeV. The analytical spectrum has been vertically shifted by multiplication through an arbitrary number to match the fast neutron portion of the measured spectrum.

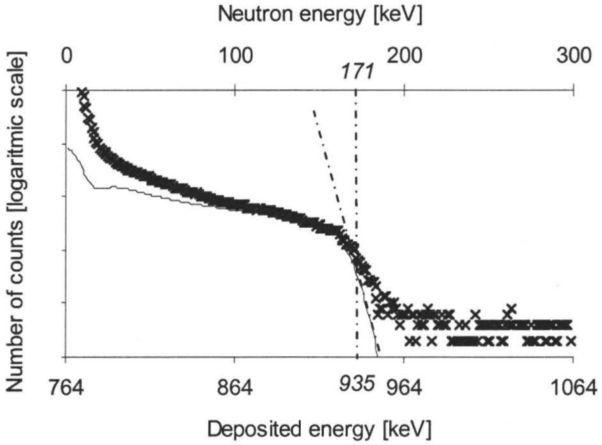

Figure 6.9: Analytical neutron fluence spectrum over the detector area for incident proton energy of 1.948 MeV (thin solid line). The graphical method of maximum neutron energy estimation (dashed lines) indicates 171 keV, which is 9 keV higher than the true maximum neutron energy. For comparison, the raw measured spectrum is shown for the nominal proton energy of 2.0 MeV (crosses).

The figure shows, that the graphical method overestimates the true maximum neutron energy. However, it is also apparent that the shapes of the high energy edge for the two spectra are different. The high energy edge for the analytical spectrum falls faster than the measured one, which may indicate that either the energy resolution encoded in the detector response did not match the experimental value or that neutron production close to the target surface was distorted due to contamination or oxidation. As a result, the high energy edge has a shape closer to a damped exponential rather than a combination of the Gaussian and the Gauss error functions as would be otherwise expected if the high energy edge had a sharp falling shape. Consequently, the proton energy offset for the measured spectra might be even higher than the one established using the simple graphical method, but for further analysis the more conservative estimate was used. The 9 keV difference between the graphical method and the true maximum proton energy (Figure 6.9), gives also an estimation of the precision of the graphical method.

Table 6.4 lists nominal proton accelerator terminal potentials indicated by the generating voltmeter (GVM), corresponding maximum neutron energies found using the graphical method from the ^{3}He spectra, and effective proton energies.

Table 6.4: Nominal and experimental effective proton energies incident on the lithium target.

Nominal accelerator terminal potential [MV]	Maximum neutron energy from the ^{3}He detector [keV]	Corresponding proton energy [MeV]	Proton energy offset [keV]
1.95	87	1.900	-50
2.00	162	1.948	-52
2.10	282	2.042	-58
2.20	401	2.145	-55
2.30	511	2.243	-57

Results presented in Table 6.4 indicate a systematic shift in the effective proton energy incident on the lithium target. This observation was used in the neutron yield verification experiment presented in the next section.

6.2.4. Total neutron yield of the ^{7}Li(p,n) reaction

The lithium target was irradiated at five nominal proton energies between 1.95 and 2.3 MeV at low proton currents to prevent target instability but high enough to induce a measurable increase in ^{7}Be activity. Table 6.5 summarizes irradiation and counting parameters used in the experiment as well as neutron yield data.

Table 6.5: Parameters and results of the neutron yield measurement

Nominal proton energy [MeV]	1.95	2.00	2.10	2.20	2.30
Effective proton energy [MeV]	1.900	1.948	2.042	2.145	2.243
Irradiation time [s]	1800	1800	1800	1800	1800
Proton current [μA]	22.9	11.1	5.3	2.3	1.1
Increase in ^{7}Be activity [kBq] (±7 %)	72	164	208	155	123
Theoretical neutron yield [× 10^{10} n/mC]	1.49	5.89	15.1	27.2	46.0
Experimental neutron yield [× 10^{10} n/mC] (±7 %)	1.16	5.49	14.4	25.2	42.9

Figure 6.10 shows comparison of the theoretical neutron yield with experimental yield. When accounting for the proton energy offset, the experimental neutron yield follows the theoretical trend closely within ~ 7 % for all proton energies except 1.95 MeV where the difference is much higher (22 %). (Table 6.5). This systematic difference may indicate that the proton offset value is even higher than the one found by the graphical method in Figure 6.9.

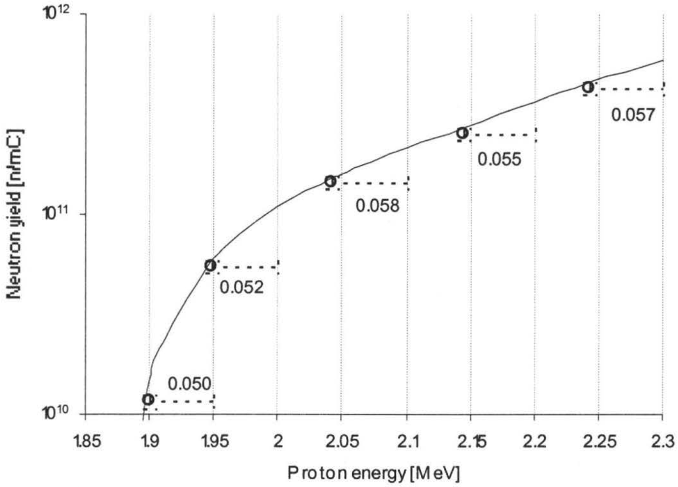

Figure 6.10: Comparison of the theoretical (solid line) and experimental (open circles) neutron yields. Dotted lines indicate proton energy offset (see Table 6.4).

6.2.5. Long term stability of the lithium target

In order to monitor long term neutron yield of the target, before and after each series of experiments, a short acquisition was conducted at standard conditions: the ^{3}He detector located at 3.7 m from the target along the proton beam line direction and the long counter at 5.5 m with a little vertical off-axis shift so that the ^{3}He did not shadow the long counter. All measurements were taken at 1.95 MeV nominal proton energy and 5 μA current for 10 minutes as well as 2.1 MeV, 1 μA current for 3 minutes. Selection of the above conditions was based on the total counting rates in the ^{3}He detector below 2000 cps. The two energies were chosen in order to verify if the yield stability also varies with the nominal proton energy.

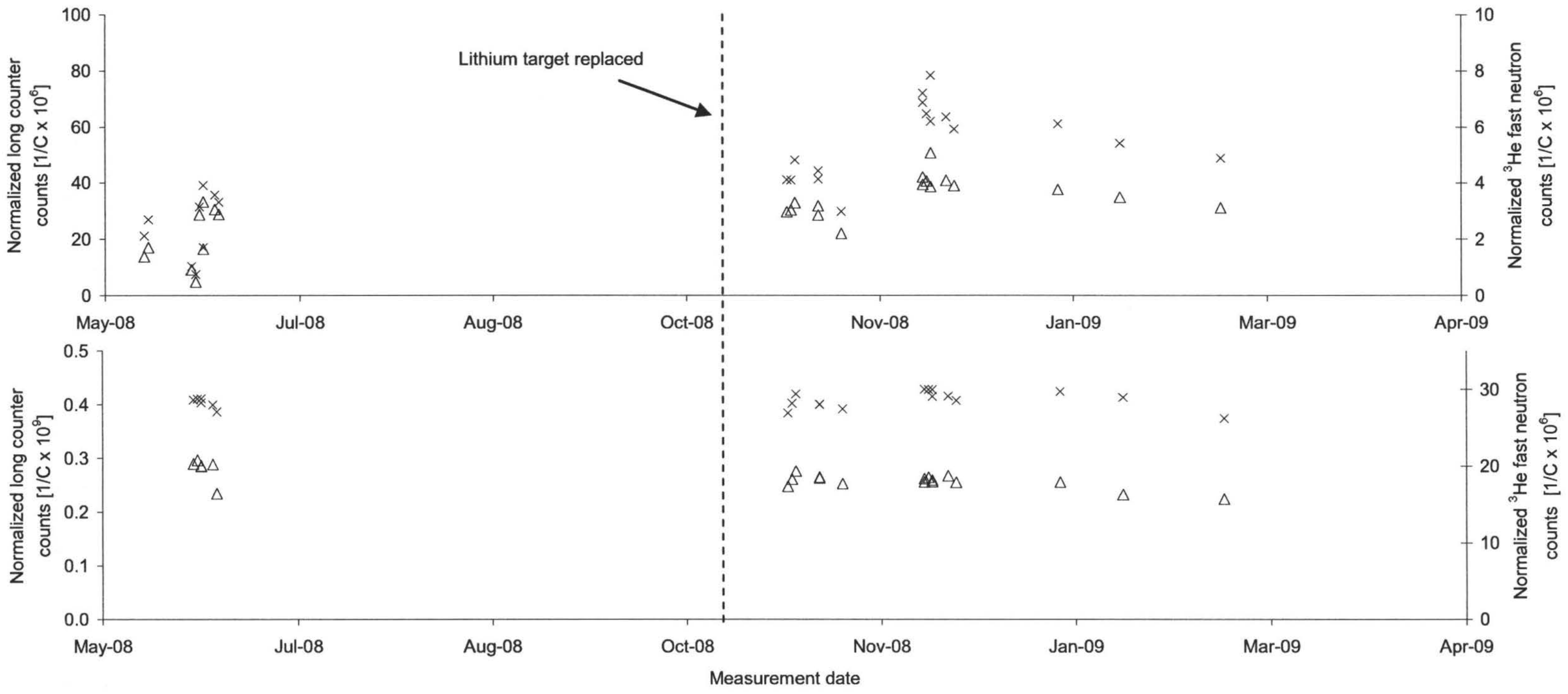

Figure 6.11: Results of the long term neutron yield monitoring with the long counter (crosses) and the ^{3}He ion chamber (triangles) for two nominal proton energies: 1.95 MeV (top) and 2.1 MeV (bottom) normalized to total proton current. The vertical dashed line indicates the date when the lithium metal target material was replaced.

Figure 6.11 shows results of the yield monitoring with two neutron detectors: the long counter and the ^{3}He ion chamber. For the latter, only events caused by fast neutrons were counted, which were defined as all neutron events above 30 keV (794 keV energy deposited in the detector). The limit of 30 keV was adopted to exclude the contribution of the epithermal peak, whose size depends on the amount of scattering materials present in the room. The two detectors show consistent relative results for both 1.95 and 2.1 MeV. At 2.1 MeV (Figure 6.11 bottom), neutron yield does not change over time, which indicates that the target condition is stable. The vertical dashed line in Figure 6.11 shows the date when the target assembly was unmounted from the beam line, the old lithium layer removed, replaced by fresh lithium metal, and the assembly reattached to the beam line end section. The figure shows that the target change does not affect the neutron yield.

On the other hand, neutron yield at 1.95 MeV (Figure 6.11 top) shows significantly more variations than at 2.1 MeV. The average number of counts above 30 keV per unit charge recorded by the ^{3}He detector is $(3.0 \pm 1.1) \times 10^6$ for 1.95 MeV and $(18 \pm 2) \times 10^6$ for 2.1 MeV. The relatively higher standard deviation for 1.95 MeV than for 2.1 MeV may be explained by the shape of the energy dependent total neutron yield close to the threshold (Figure 6.10). At the nominal proton energy of 1.95 MeV, the effective proton energy is approximately 1.90 MeV. In this region, the yield varies rapidly with proton energy, much faster than in the 2.1 MeV region (effective proton energy ~2.06 MeV).

Chapter 7

CONCLUSIONS AND FUTURE WORK

7.1. Conclusions

The ^{7}Li(p,n) accelerator based neutron source is suitable for use in research and clinical applications due to its high neutron yield and relatively soft neutron spectrum. However, the accuracy of results, regardless of the applications, is mostly determined by the accuracy of neutron dosimetry. Until now, only the theoretical spectra based on the cross-section and kinematics of the reaction have been used for neutron dose calculations from the source. A few studies reported significant discrepancies between the calculated and experimental neutron doses, which were attributed to the target condition or energy stability of the proton beam, but there has been no experimental verification of the neutron dose based on the measured neutron spectra.

In this study, the neutron spectra from the thick target ^{7}Li(p,n) source were measured in the incident proton energy range between 1.95 and 2.3 MeV with a ^{3}He ionization chamber.

First, the properties of the detector and the acquisition system were investigated. The experimentally verified response function and efficiency for this detector are only available in the neutron energy region between 130 keV and 3 MeV, but a significant portion of the measured fluence from the ^{7}Li(p,n) source was expected below 130 keV. It was therefore necessary to extend the dynamic range of the detector to lower neutron energies. 30 keV was found to be the lowest limit due to interference of the epithermal peak. The efficiency of the detector could not be experimentally verified easily in this energy region, and therefore MC simulation was employed. Similarly, the response of the detector could not be experimentally found, but in addition, the MC simulations reported in the literature showed discrepancies between experimental and simulated results. In this work, the following approach was applied: using the proton chopper, the detector response for epithermal neutrons was measured and parameterized using the same set of parameters as the published experimental response. Then, the parameters were interpolated between ~ 0 keV (epithermal region) and 130 keV. This way, the response of the detector could be in part verified experimentally.

Next, it was necessary to use a suitable spectral unfolding algorithm to unravel neutron spectra from the raw measured spectra. The iterative approach introduced by van Cittert and modified by Jansson was employed. The algorithm however, was not suitable for unfolding neutron spectra using the full detector response, because the relative size of the epithermal peak made the unfolding process unstable. Only the part of the response above 794 keV (> 30 keV neutron energy) was used, so therefore a significant portion of the information below this limit was lost. It was concluded that if the events from the epithermal neutrons can be rejected so that the epithermal peak size is reduced, the unfolding using the full response can be attempted. As the most convenient method, the TOF rejection of slow neutrons was selected.

For this purpose, the proton chopper and the 2-D time energy analyzing system were developed. Two designs of proton chopper HV switch were tested, and finally the model based on fast switching was chosen for further experiments. The 2-D system records energy and arrival time of incoming events and was used to characterize the timing behavior of the pulsing system. It was experimentally verified that the fast neutron yield of the neutron spectra collected in the proton pulsing mode is equivalent to the yield from neutron spectra acquired in the continuous current mode. The proton pulsed beam acquisition reduced the size of the epithermal peak considerably, but the iterative algorithm was still unable to unfold neutron spectra collected in the pulsing mode using the full response function. However, another algorithm based on constrained regularized inversion was employed instead. Neutron spectra unfolded with this algorithm were compared with spectra unfolded with the iterative algorithm, which used the above 794 keV portion of the spectrum, as well with spectra obtained by simple division by energy dependent efficiency. It was concluded, that for incident proton energies up to 2.1 MeV, the neutron spectra do not require unfolding and, simple division by efficiency is sufficient if measurement inaccuracy of approximately 5 % can be tolerated. For higher incident proton energies, unfolding is needed, but the full detector response is not necessary, and the iterative algorithm using the portion of the spectrum above 794 keV gives satisfactory results.

From the raw ^{3}He spectrometer neutron spectra, it was identified that the maximum neutron energy measured from raw spectra is lower than analytically calculated for the same nominal proton energy. This observation led to the conclusion that effective proton energy incident on the target is lower than that indicated by the generating voltmeter of the accelerator terminal. Using the effective proton energies, analytical neutron fluence spectra were calculated and compared with the unfolded experimental neutron spectra. This comparison was made for spectra collected at various angles with respect to the proton beam propagation direction, various distances from the target in a forward direction, and various incident proton energies. All measurements indicated significant scattering, which was observed as a partial moderation of the source spectrum and as in-scattering of high energy neutrons originally emitted in forward direction to higher angles. Due to these processes, the calculated kerma in forward direction consistently overestimates the experimental. With increasing distance from the source, the scattering component of the total fluence becomes more significant, and at the most often studied distance of 3.7 m, the direct and scattered components are comparable.

Since the efficiency of the ^{3}He detector has not been verified in the full neutron energy range studied, the TEPC microdosimetric measurements were used for comparison. Results of the measurements taken with the two types of detectors (½" and 5") showed the TEPC measured doses for lower proton energies approximately 20 % below those measured with the ^{3}He spectrometer. This difference increased to ~ 50 % for higher proton energies.

The Monte Carlo method was also used to model scattering conditions in the experimental room, and the simulation results were in agreement within ~ 30 % with experimental values.

To further verify the proton energy offset, the total neutron yield measurement from the ^{7}Li(p,n) reaction was made. The results showed, that when accounting for this offset, neutron yield from the target follows the theoretically calculated results within approximately 20 % for 1.95 MeV and within 7 % for other measured proton energies. A conservative assessment of the offset was made and was found to vary between 50 and 58 keV in the proton energy region between 1.95 and 2.3 MeV.

Long term stability of the lithium target was also monitored for a period of approximately one year. No significant variations in the yield were observed at 2.1 MeV, even after target replacement. More instability was identified at 1.95 MeV and was attributed to the fact that the neutron yield varies rapidly in the region near threshold; therefore, even small proton beam energy instability may induce significant changes in the total neutron yield.

7.2. Future work

The ^{3}He detector is well suited for measurement of the ^{7}Li(p,n) ABNS near threshold but more work is needed to overcome some difficulties found when working with this detector. First, its hypersensitivity to epithermal neutrons has to be addressed. In this work, the pulsing system combined with TOF rejection of slow neutrons was used, but other methods can be also tried i.e. the pulse shape discrimination. As reported in the literature, the recoil events can be successfully discriminated against using this method. The necessary equipment for the off-line pulse shape analysis has already been built and preliminary data collected, but the ultimate goal is a real time pulse shape discriminator. Such system would significantly increase throughput of the ^{3}He chamber and enhance the response of the spectrometer to fast neutrons.

Another aspect which needs further work is the fact that the response function and efficiency of the detector have not been experimentally verified in the energy region between 30 and 130 keV. Knowing the neutron yield from the ^{7}Li(p,n) source, direct and scattered fluence can be identified and the ^{3}He detector efficiency indirectly verified.

The Monte Carlo method can be extremely useful in modeling the detector response as well as scattering conditions due to the target assembly and the walls of the experimental area. The simulation results presented in this study agree well with the experiment for proton energies up to approximately 2.1 MeV but diverge from the experimental values for higher proton energies, therefore a more accurate model of the scattering conditions in the experimental area is needed.

To help analyze the scattering vs. direct fluence ratio, measurements at various distances from the target at emission angles other than zero degrees should be taken. This way, relative contribution of the target assembly and walls of the experimental area can be determined. Knowing the relative scattering contribution of the target assembly, new designs minimizing neutron scattering can be simulated using the MC method.

REFERENCES

Allen, D. A., Beynon, T. D., Green, & James, N. D. (1999). Toward a final design for the Birmingham boron neutron capture therapy neutron beam. *Medical Physics*, *26*(1), 77-82. doi:10.1118/1.598480

Arnold, M. L., McNeill, F. E., Prestwich, W. V., & Chettle, D. R. (2000). System design for in vivo neutron activation analysis measurements of manganese in the human brain: based on Monte Carlo modeling. *Applied Radiation and Isotopes*, *53*(4-5), 651-656. doi:10.1016/S0969-8043(00)00199-8

Arnold, M. L., McNeill, F. E., Stronach, I. M., Pejović-Milić, A., Chettle, D. R., & Waker, A. (2002). An accelerator based system for in vivo neutron activation analysis measurements of manganese in human hand bones. *Medical Physics*, *29*(11), 2718-2724. doi:10.1118/1.1517613

Aslam, Pejović-Milić, A., McNeill, F. E., Byun, S. H., Prestwich, W. V., & Chettle, D. R. (2008). In vivo assessment of magnesium status in human body using accelerator-based neutron activation measurement of hands: A pilot study. *Medical Physics*, *35*(2), 608-616. doi:10.1118/1.2830383

Aslam, Prestwich, W. V., & McNeill, F. E. (2003). Lithium target performance evaluation for low-energy accelerator-based in vivo measurements using gamma spectroscopy. *Applied Radiation and Isotopes*, *58*(3), 321-331. doi:10.1016/S0969-8043(02)00346-9

Bayanov, B., Kashaeva, E., Makarov, A., Malyshkin, G., Samarin, S., & Taskaev, S. (2009). A neutron producing target for BINP accelerator-based neutron source. *Applied Radiation and Isotopes*, *67*(7-8, Supplement 1), S282-S284. doi:10.1016/j.apradiso.2009.03.076

Beimer, K., Nyman, G., & Tengblad, O. (1986). Response function for 3-He neutron spectrometers. *Nuclear Instruments and Methods in Physics Research Section A: Accelerators, Spectrometers, Detectors and Associated Equipment*, *245*(2-3), 402-414. doi:10.1016/0168-9002(86)91275-1

Berkovits, D., Paul, M., Ben-Dov, Y., Bordeanu, C., Ghelberg, S., Heber, O., Hass, M., et al. (2004). Upgrading of the AMS facility at the Koffler 14UD Pelletron accelerator. *Nuclear Instruments and Methods in Physics Research Section B: Beam Interactions with Materials and Atoms*, *223-224*, 161-167. doi:10.1016/j.nimb.2004.04.033

Bleuel, D. L., Donahue, R. J., Ludewigt, B. A., & Vujic, J. (1998). Designing accelerator-based epithermal neutron beams for boron neutron capture therapy. *Medical Physics*, *25*(9), 1725-1734. doi:10.1118/1.598353

Blue, T. E., & Yanch, J. C. (2003). Accelerator-based Epithermal Neutron Sources for Boron Neutron Capture Therapy of Brain Tumors. *Journal of Neuro-Oncology*, *62*(1), 19-31. doi:10.1023/A:1023247222043

Briesmeister, J. (1997). *MCNP - A General Monte Carlo N-Particle Transport Code*. Los Alamos National Laboratory. Retrieved from http://mcnp-green.lanl.gov

Brooks, F. D., & Klein, H. (2002). Neutron spectrometry--historical review and present status. *Nuclear Instruments and Methods in Physics Research Section A: Accelerators, Spectrometers, Detectors and Associated Equipment*, *476*(1-2), 1-11. doi:10.1016/S0168-9002(01)01378-X

Byun, S. H., Pejović-Milić, A., McMaster, S., Matysiak, W., Aslam, Liu, Z., Watters, L. M., et al. (2007). Dosimetric characterization of the irradiation cavity for accelerator-based in vivo neutron activation analysis. *Physics in Medicine and Biology*, *52*(6), 1693-1703.

Chadwick, M. B., Barschall, H. H., Caswell, R. S., DeLuca, P. M., Hale, G. M., Jones, D. T. L., MacFarlane, R. E., et al. (1999). A consistent set of neutron kerma coefficients from thermal to 150 MeV for biologically important materials. *Medical Physics*, *26*(6), 974-991. doi:10.1118/1.598601

van Cittert, P. H. (1931). Zum Einfluß der Spaltbreite auf die Intensitätsverteilung in Spektrallinien. II. *Zeitschrift für Physik A Hadrons and Nuclei*, *69*(5), 298-308. doi:10.1007/BF01391351

Crilly, P. B. (1990). The use of a cross-correlation technique to enhance Jansson's deconvolution procedure. *Journal of Chemometrics*, *4*(4), 291-298. doi:10.1002/cem.1180040404

Culbertson, C. N., Green, S., Mason, A. J., Picton, D., Baugh, G., Hugtenburg, R. P., Yin, Z., et al. (2004). In-phantom characterisation studies at the

Birmingham Accelerator-Generated epIthermal Neutron Source (BAGINS) BNCT facility. *Applied Radiation and Isotopes, 61*(5), 733-738. doi:10.1016/j.apradiso.2004.05.057

Draxler, M., Gruber, R., & Bauer, P. (2003). Evaluation of absolute ion fractions from TOF-LEIS spectra. *Journal of Electron Spectroscopy and Related Phenomena, 129*(2-3), 165-169. doi:10.1016/S0368-2048(03)00065-3

Evans, A. E., & Brandenberger, J. D. (1979). High resolution fast neutron spectroscopy without time-of-flight. *IEEE Transactions on Nuclear Science, NS-26*, 1484-1487.

Fifield, L., Tims, S., Gladkis, L., Morton, C., & Barrows, T. (2006). Aluminium-26 measurements with beryllium-10 counting statistics. *Geochimica et Cosmochimica Acta, 70*(18, Supplement 1), A172. doi:10.1016/j.gca.2006.06.346

Franz, H., Rudolph, W., Ohm, H., Kratz, K., Herrmann, G., Nuh, F., Slaughter, D., et al. (1977). Delayed-neutron spectroscopy with 3-He spectrometers. *Nuclear Instruments and Methods, 144*(2), 253-261. doi:10.1016/0029-554X(77)90116-1

Iguchi, T., Nakayamada, N., Takahashi, H., & Nakazawa, M. (1994). Neutron spectrometry using a 3-He gas ionization chamber. *Nuclear Instruments and Methods in Physics Research Section A: Accelerators, Spectrometers, Detectors and Associated Equipment, 353*(1-3), 152-155. doi:10.1016/0168-9002(94)91625-X

Jansson, P. A. (1995). *Deconvolution with Application in Spectroscopy.* Academic Press.

Lee, C. L., & Zhou, X. -. (1999). Thick target neutron yields for the 7-Li(p,n)7-Be reaction near threshold. *Nuclear Instruments and Methods in Physics Research Section B: Beam Interactions with Materials and Atoms, 152*(1), 1-11. doi:10.1016/S0168-583X(99)00026-9

Lee, C. L., Zhou, X. -., Harmon, J. F., Bartholomay, R. W., Harker, Y. D., & Kudchadker, R. J. (1999). Thermal neutron flux mapping in a head phantom. *Nuclear Instruments and Methods in Physics Research Section A: Accelerators, Spectrometers, Detectors and Associated Equipment, 422*(1-3), 106-110. doi:10.1016/S0168-9002(98)01174-7

Liskien, H., & Paulsen, A. (1975). Neutron production cross sections and energies for the reactions 7-Li(p,n)7-Be and 7-Li(p,n)7-Be*. *Atomic Data and Nuclear Data Tables, 15*(1), 57-84.

Loughlin, M. J., Adams, J. M., & Sadler, G. (1990). Measurement of the response function of a 3-He ionisation chamber to monoenergetic neutrons in the energy range from 2.0 to 3.0 MeV. *Nuclear Instruments and Methods in Physics Research Section A: Accelerators, Spectrometers, Detectors and Associated Equipment, 294*(3), 606-615. doi:10.1016/0168-9002(90)90305-P

MathWorks Inc. (2008). *Matlab.* Natick, Massachusetts.

Matysiak, W., Chin, K., McMaster, S., Prestwich, W. V., & Byun, S. H. (2009).

Relative Enhancement of a 3-He Ion Chamber Response to Fast Neutrons by TOF Rejection of Slow Neutrons with a Pulsed Neutron Source. *Nuclear Science, IEEE Transactions on*, *56*(1), 266-271. doi:10.1109/TNS.2008.2008805

Matysiak, W., Prestwich, W. V., & Byun, S. H. (2008). Measurement of the thick target 7-Li(p,n) neutron source spectrum using a 3-He ionization chamber. *Nuclear Instruments and Methods in Physics Research Section A: Accelerators, Spectrometers, Detectors and Associated Equipment*, *592*(3), 316-324. doi:10.1016/j.nima.2008.03.110

McFee, J. E. (1977). *Photoneutron spectroscopy of nuclei near mass 200.* McMaster University.

Newson, H. W., Williamson, R. M., Jones, K. W., Gibbons, J. H., & Marshak, H. (1957). 7-Li(p, n), (p, p' gamma), and (p, gamma) Reactions near Neutron Threshold. *Physical Review*, *108*(5), 1294. doi:10.1103/PhysRev.108.1294

Ohm, H., Kratz, K., & Prussin, S. (1987). The analysis of delayed neutron energy spectra recorded with 3-He ionization chambers. *Nuclear Instruments and Methods in Physics Research Section A: Accelerators, Spectrometers, Detectors and Associated Equipment*, *256*(1), 76-90. doi:10.1016/0168-9002(87)91041-2

Pejović-Milić, A., Arnold, M. L., McNeill, F. E., & Chettle, D. R. (2000). Monte Carlo design study for in vivo bone aluminum measurement using a low energy accelerator beam. *Applied Radiation and Isotopes*, *53*(4-5), 657-664. doi:10.1016/S0969-8043(00)00200-1

Petrich, D., Heil, M., Käppeler, F., Kaltenbaek, J., Knaetsch, E., Litfin, K., Roller, D., et al. (2008). A neutron production target for FRANZ. *Nuclear Instruments and Methods in Physics Research Section A: Accelerators, Spectrometers, Detectors and Associated Equipment*, *596*(3), 269-275. doi:10.1016/j.nima.2008.08.131

Provencher, S. W. (1982). CONTIN: a general purpose constrained regularization program for inverting noisy linear algebraic and integral equations. *Computer Physics Communications*, *27*(3), 229-242.

Ritchie, A. I. M. (1976). Neutron yields and energy spectra from the thick target Li(p,n) source. *Journal of Physics D: Applied Physics*, *9*(1), 15-26.

Sailor, W. C., Prussin, S. G., & Derzon, M. S. (1988). Monte Carlo calculation of the response function for a 3-He neutron spectrometer. *Nuclear Instruments and Methods in Physics Research Section A: Accelerators, Spectrometers, Detectors and Associated Equipment*, *270*(2-3), 527-536. doi:10.1016/0168-9002(88)90726-7

Sekharan, K. K., Laumer, H., Kern, B. D., & Gabbard, F. (1976). A neutron detector for measurement of total neutron production cross sections. *Nuclear Instruments and Methods*, *133*(2), 253-257. doi:10.1016/0029-554X(76)90617-0

SHARCNET. (2008). Shared Hierarchical Academic Research Computing

Network. Retrieved from http://www.sharcnet.ca

Taccetti, N., Giuntini, L., Casini, G., Stefanini, A. A., Chiari, M., Fedi, M. E., & Mandò, P. A. (2002). The pulsed beam facility at the 3 MV Van de Graaff accelerator in Florence: Overview and examples of applications. *Nuclear Instruments and Methods in Physics Research Section B: Beam Interactions with Materials and Atoms*, *188*(1-4), 255-260. doi:10.1016/S0168-583X(01)01109-0

Xu, C., Aissaoui, I., & Jacquey, S. (1994). Algebraic analysis of the Van Cittert iterative method of deconvolution with a general relaxation factor. *Journal of the Optical Society of America A*, *11*(11), 2804-2808. doi:10.1364/JOSAA.11.002804

Young, F. C. (1996). Radioactivities induced in commonly used materials by proton and deuteron beams up to 10 MeV. *Atomic Data and Nuclear Data Tables*, *64*(2), 223-251.

Yu, W., Yue, G., Han, X., Chen, J., & Tian, B. (1998). Measurements of the neutron yields from 7-Li(p,n)7-Be reaction (thick target) with incident energies from 1.885 to 2.0 MeV. *Medical Physics*, *25*(7), 1222-1224. doi:10.1118/1.598299

Ziegler, J. (2006). *SRIM-the stopping and ranges of ions in matter*. Retrieved from http://www.srim.org